

Electronic Thesis and Dissertation Repository

---

5-29-2012 12:00 AM

## Numerical investigation of highly curved turbulent flows in centrifugal compressors and in a simplified geometry

Kevin J. Elliott  
*The University of Western Ontario*

Supervisor  
Dr. Chao Zhang  
*The University of Western Ontario* Joint Supervisor  
Dr. Eric Savory  
*The University of Western Ontario*

Graduate Program in Mechanical and Materials Engineering  
A thesis submitted in partial fulfillment of the requirements for the degree in Master of Engineering Science  
© Kevin J. Elliott 2012

Follow this and additional works at: <https://ir.lib.uwo.ca/etd>



Part of the [Aerodynamics and Fluid Mechanics Commons](#)

---

### Recommended Citation

Elliott, Kevin J., "Numerical investigation of highly curved turbulent flows in centrifugal compressors and in a simplified geometry" (2012). *Electronic Thesis and Dissertation Repository*. 556.  
<https://ir.lib.uwo.ca/etd/556>

This Dissertation/Thesis is brought to you for free and open access by Scholarship@Western. It has been accepted for inclusion in Electronic Thesis and Dissertation Repository by an authorized administrator of Scholarship@Western. For more information, please contact [wlsadmin@uwo.ca](mailto:wlsadmin@uwo.ca).

# **Numerical investigation of highly curved turbulent flows in centrifugal compressors and in a simplified geometry**

(Spine Title: Numerical investigation of highly curved turbulent flows)

(Thesis format: Monograph)

By

Kevin J. Elliott

Graduate Program in Mechanical and Materials Engineering

A thesis submitted in partial fulfillment  
of the requirements for the degree of  
Master of Engineering Science

The School of Graduate and Postdoctoral Studies  
The University of Western Ontario  
London, Ontario, Canada

© Kevin J. Elliott 2012

THE UNIVERSITY OF WESTERN ONTARIO  
School of Graduate and Postdoctoral Studies

**CERTIFICATE OF EXAMINATION**

Joint-Supervisor

\_\_\_\_\_  
Dr. Chao Zhang

Joint-Supervisor

\_\_\_\_\_  
Dr. Eric Savory

Supervisory Committee

\_\_\_\_\_  
Dr. Anthony Straatman

Examiners

\_\_\_\_\_  
Dr. Anthony Straatman

\_\_\_\_\_  
Dr. Jun Yang

\_\_\_\_\_  
Dr. Girma Bitsuamlak

The thesis by

**Kevin James Elliott**

entitled:

**Numerical investigation of highly curved turbulent flows in centrifugal compressors and in a simplified geometry**

is accepted in partial fulfillment of the  
requirements for the degree of  
Master of Engineering Science

Date: \_\_\_\_\_

\_\_\_\_\_  
Chair of the Thesis Examination Board

## ABSTRACT

---

Curvature effects are investigated in terms of a recently developed curvature corrected turbulence model in turbomachinery applications. Two centrifugal compressor stages and a curved geometry modelled after a centrifugal impeller are simulated using the curvature corrected SST (SST-CC) turbulence model. This work improves the understanding of how the SST-CC model predicts curvature effects. An analysis of the SST-CC production multiplier,  $f_{r1}$ , in both centrifugal cases reveals that the model is appropriately accounting for curvature effects, showing increased production near concave surfaces and decreased production near convex surfaces. These results correlate well with the simplified geometry results and demonstrate that the simplified geometry is successfully capturing the curvature effects of the centrifugal stages. A detailed investigation of turbulence quantities in the simplified geometry further demonstrated how curvature effects are predicted by the SST-CC model. Future work will include experimentation on the 1C stage and further comparison with numerical results.

**Keywords:** SST-CC, computational fluid dynamics, curvature, centrifugal compressors, turbulence modelling, turbomachinery

## **ACKNOWLEDGEMENTS**

---

First of all, I would like to thank my joint-supervisors Dr. Chao Zhang and Dr. Eric Savory for inviting me to join this project and for always being very helpful in offering guidance and support. I'd also like to thank Dr. Robert Martinuzzi from the University of Calgary, who always found the time to provide valuable direction, despite a very full schedule. Furthermore, thanks are due to Pratt and Whitney Canada (P&WC) for extending the opportunity to work on this project. It was an excellent chance to be able to research in conjunction with a leader in the Canadian aerospace industry. Many thanks are extended to the personnel in the compressor division, specifically Hong Yu, Douglas Roberts and Peter Townsend for their help over the course of this project. Finally, thanks are due to SHARCNET, who provided the computational resources for running many of the simulations in this work.

I would also like to thank various colleagues for their input over the course of this project: Jason Bourgeois, for helping to configure compressor simulations and helping to interpret his previous work, Dr. William Lin, for helping with project coordination, and Zixiang Chen, for assisting in the initial simulation setup and for running some simulations on Westgrid. I would also like to thank my colleagues in the Advanced Fluid Mechanics (AFM) research group, for providing a productive and fun research environment. Finally, many thanks are extended to Emily and my parents, Gwen and Scott, for providing extensive moral support throughout the entire process.

My gratitude is expressed to the sources of funding that made this project possible: Pratt and Whitney Canada (P&WC), the Green Aviation Research and Development Network (GARDN), and Mathematics of Information Technology and Complex Systems (MITACS). Thanks are also due to the Government of Ontario for their financial support through the Ontario Graduate Scholarship (OGS) program.

# TABLE OF CONTENTS

---

---

<b>Abstract .....</b>	<b>iii</b>
<b>Acknowledgements .....</b>	<b>iv</b>
<b>List of tables .....</b>	<b>ix</b>
<b>List of figures .....</b>	<b>x</b>
<b>List of abbreviations, symbols and nomenclature .....</b>	<b>xiv</b>
<b>1. Introduction .....</b>	<b>1</b>
1.1 Scope and objectives of the present work.....	4
1.2 Organization of the thesis .....	5
1.3 Summary .....	6
<b>2. Turbomachinery background.....</b>	<b>7</b>
2.1 Compressor types .....	7
2.2 Basics of operation .....	7
2.2.1 Axial compressors.....	7
2.2.2 Centrifugal compressors .....	8
2.3 Compressor selection.....	8
2.4 Compressor performance evaluation .....	9
2.4.1 Subscripts in compressors.....	9
2.4.2 Characteristic curves (speedlines).....	10
2.4.3 Efficiency lines.....	11
2.5 Summary .....	12
<b>3. Literature review .....</b>	<b>13</b>
3.1 Curvature effects.....	13
3.1.1 Magnitude of curvature effects.....	14
3.1.2 Curvature directionality effects.....	16
3.1.3 Effect of Reynolds number (Re) on curvature .....	19
3.1.4 Effect of streamwise pressure gradients on curvature .....	21

3.1.5	Summary .....	24
3.2	Turbulence modelling – Theory and governing equations.....	24
3.2.1	Origin of the turbulent transport equations.....	26
3.2.2	Two-equation eddy viscosity models (EVM).....	29
3.2.3	Reynolds stress models (RSM) .....	35
3.2.4	Turbulence models studied in current work.....	38
3.2.5	Summary .....	38
3.3	Turbulence modelling with respect to curvature.....	39
3.3.1	Evaluation of EVMs with respect to predicting curvature effects.....	40
3.3.2	Curvature corrections for EVMs.....	41
3.3.3	Selection of the SST-CC model.....	43
3.3.4	Summary .....	44
3.4	Turbulence modelling in turbomachinery applications .....	45
3.4.1	Summary .....	48
3.5	Summary and analysis of the literature review .....	48
<b>4.</b>	<b>Centrifugal compressors – Numerical setup .....</b>	<b>51</b>
4.1	Description of the geometry .....	51
4.1.1	The 307C centrifugal stage.....	51
4.1.2	The 1C centrifugal stage .....	53
4.2	Matching test rig and in-flight conditions (1C) .....	54
4.2.1	Application of non-dimensional parameters.....	54
4.2.2	Application of Reynolds number corrections for efficiency.....	57
4.3	Boundary conditions .....	58
4.3.1	Impeller inlet .....	60
4.3.2	Impeller exit/diffuser inlet.....	60
4.3.3	Diffuser exit .....	60
4.3.4	Other boundary conditions .....	61
4.4	Meshing.....	61

4.4.1	Impeller mesh.....	61
4.4.2	Diffuser mesh.....	62
4.4.3	Mixing plane mesh.....	65
4.4.4	$y^+$ values and wall functions.....	66
4.4.5	Grid independence.....	67
4.5	Solver description.....	67
4.5.1	Advection schemes .....	68
4.5.2	Solver control and output control .....	68
4.6	Summary .....	69
<b>5.</b>	<b>Simplified geometry – Numerical setup.....</b>	<b>70</b>
5.1	Description of the geometry .....	70
5.2	Idealizations from the centrifugal case .....	73
5.2.1	No blades or rotation.....	73
5.2.2	Unidirectional curvature.....	74
5.2.3	Fully developed flow.....	74
5.2.4	Constant temperature .....	74
5.3	Meshing.....	74
5.3.1	Grid independence study .....	76
5.4	Boundary conditions .....	78
5.5	Solver description.....	78
5.5.1	Turbulence models.....	79
5.5.2	Convergence criteria.....	79
5.6	Summary .....	79
<b>6.</b>	<b>307C compressor results.....</b>	<b>80</b>
6.1	Global performance – PR and efficiency .....	80
6.2	Comparison with experimental data – flow field .....	83
6.2.1	Impeller-Diffuser Interface (Mixing Plane).....	83
6.2.2	Diffuser Exit.....	85



6.3	Investigation of the production multiplier, $f_{r1}$ .....	88
6.4	Summary .....	91
<b>7.</b>	<b>1C compressor results .....</b>	<b>93</b>
7.1	Limitations of this case .....	93
7.2	Global performance – PR and efficiency .....	93
7.3	Investigation of the production multiplier, $f_{r1}$ .....	96
7.4	Comparison of eddy viscosity .....	99
7.5	Summary .....	102
<b>8.</b>	<b>Simplified geometry investigation.....</b>	<b>104</b>
8.1	Curvature and flow parameters .....	105
8.2	Mean velocity profiles .....	106
8.3	Turbulent kinetic energy (TKE) profiles .....	109
8.4	Reynolds normal stresses.....	113
8.5	Production of TKE Profiles.....	121
8.6	Analysis of the $f_{r1}$ formulation .....	124
8.7	Summary .....	126
<b>9.</b>	<b>Conclusions .....</b>	<b>127</b>
<b>10.</b>	<b>Recommendations for future work .....</b>	<b>130</b>
	<b>References .....</b>	<b>132</b>
	<b>Appendix I – Sample calculations .....</b>	<b>136</b>
	<b>Appendix II – Additional plots .....</b>	<b>137</b>

## LIST OF TABLES

---

<b>Table 1:</b> Typical characteristics for axial and centrifugal compressors, adapted from (Boyce, 2003, p. 5).....	8
<b>Table 2:</b> Key locations in the compressor stages and their associated subscripts ...	10
<b>Table 3:</b> Summary of previous experiments completed in terms of curvature magnitude, curvature directionality, the Reynolds number and the presence of pressure gradients .....	20
<b>Table 4:</b> Constants for the pressure-strain correlation term in the RSM-SSG turbulence model.....	37
<b>Table 5:</b> Comparison of the test rig and in flight R and $\gamma$ values for the 1C stage simulations.....	55
<b>Table 6:</b> Summary of boundary conditions for each location in the centrifugal compressors .....	59
<b>Table 7:</b> Summary of mesh types and number of elements for the two compressor cases.....	61
<b>Table 8:</b> Details on the meshes for the grid independence study.....	77
<b>Table 9:</b> Comparison of mass flow averaged (MFA) outlet flow variables for the three meshes .....	77

## LIST OF FIGURES

---

<b>Figure 1:</b> Cross section of a Pratt and Whitney Canada aero-engine (c/o P&WC) .....	3
<b>Figure 2:</b> Example of the different flow regions on a compressor characteristic curve .....	10
<b>Figure 3:</b> Diagram of different curvature directions (Piquet, 1999, p. 563) .....	13
<b>Figure 4:</b> Coordinate system and variable definition for a curved surface (Piquet, 1999, p. 565).....	15
<b>Figure 5:</b> Taylor-Gortler style vortices that form in the presence of concave surfaces .....	18
<b>Figure 6:</b> Maximum secondary flow intensity as a function of downstream distance along a curved channel for different radii of curvature in an LES study by Münch & Metais (2007). $D_h$ is the hydraulic diameter of the duct, and $s$ is the arc length. ....	19
<b>Figure 7:</b> Wind tunnel section setup for zero pressure gradient; the radius of curvature gradually increases so neither a favourable or adverse pressure gradient exists (So & Mellor, 1973).....	22
<b>Figure 8:</b> Test configurations for the experiment conducted by Holloway et al. (2005). $R_m$ and $R_s$ represent cases where the pressure gradient is removed from the second section, $A_m$ and $A_s$ represent cases where the pressure gradient is applied to the second section .....	23
<b>Figure 9:</b> Full model of the 307C stage; consisting of 31 impeller blades split between an inducer (silver) and an exducer (blue) and 22 diffuser passages (brown).....	52
<b>Figure 10:</b> Section of 307C centrifugal stage (computational domain) .....	52
<b>Figure 11:</b> Full model of the 1C stage; consisting of 28 impeller blades (blue) and 26 diffuser passages (brown).....	53
<b>Figure 12:</b> Section of 1C centrifugal stage being analyzed numerically.....	54
<b>Figure 13:</b> Comparison of speedlines (normalized pressure ratio vs. corrected mass flow) for the 1C stage between the in-flight and test rig conditions with and without $\gamma$ in the corrected speed calculation.....	56

<b>Figure 14:</b> Efficiency plot for test rig conditions after applying the Hutton and Ackeret Reynolds number corrections to the in-flight condition .....	58
<b>Figure 15:</b> Schematic of the boundary condition surfaces (1C compressor geometry) .....	59
<b>Figure 16:</b> Structured hexahedral mesh for the (a) 307C impeller and (b) 1C impeller.....	63
<b>Figure 17:</b> Unstructured tetrahedral diffuser mesh for (a) 307C compressor and (b) 1C compressor. ....	64
<b>Figure 18:</b> Connection interface for the mixing plane. (a) Structured hexahedral impeller side and (b) unstructured tetrahedral diffuser side .....	66
<b>Figure 19:</b> Law of the wall, adapted from Wilcox (2006, p. 17).....	67
<b>Figure 20:</b> Centrifugal impeller passage for the 1C compressor stage.....	71
<b>Figure 21:</b> Simplified version of a centrifugal compressor impeller passage.....	71
<b>Figure 22:</b> Full 360° rotation of the simplified geometry .....	72
<b>Figure 23:</b> Straight section added to ensure fully developed flow at the curved section inlet.....	73
<b>Figure 24:</b> Hexahedral mesh used in the simplified geometry. (a) Isometric view and (b) side view.....	76
<b>Figure 25:</b> Comparison of velocity and TKE at the outlet using different meshes. (a) Velocity and (b) TKE.....	78
<b>Figure 26:</b> Comparison of 307C compressor speedlines from the SST and SST-CC models with experimental data and RSM-SSG results from Bourgeois et al. (2011) at 100% design speed .....	81
<b>Figure 27:</b> 307C compressor total-to-static efficiency line for the SST, SST-CC models compared to experimental data and RSM-SSG results from Bourgeois et al. (2011) at 100% design speed.....	81
<b>Figure 28:</b> Radial velocity, $c_r$ , at the mixing plane, normalized by the blade tip speed, $U_2$ .....	84
<b>Figure 29:</b> Circumferential velocity, $c_\theta$ , at the mixing plane, normalized by the blade tip speed, $U_2$ .....	84

<b>Figure 30:</b> Axial velocity contours at the diffuser exit, normalized by the blade tip speed. (a) Experimental data (Bourgeois et al., 2011) (b) SST model (c) SST-CC model.....	86
<b>Figure 31:</b> Circumferential velocity contours at the diffuser exit, normalized by the blade tip speed. (a) Experimental data (Bourgeois et al., 2011) (b) SST model (c) SST-CC model .....	87
<b>Figure 32:</b> Development of the $f_{r1}$ parameter in the 307C, progressing spanwise in the impeller starting at the hub: (a) 5%, (b) 25%, (c) 50%, (d) 75% and (e) 95% span.....	90
<b>Figure 33:</b> Meridional plot of $f_{r1}$ (circumferentially averaged) for the 307C compressor.....	91
<b>Figure 34:</b> 1C compressor speedline for the SST, SST-CC and RSM-SSG models at 100% design speed .....	94
<b>Figure 35:</b> 1C compressor total-to-static efficiency line for the SST, SST-CC and RSM-SSG models at 100% design speed.....	95
<b>Figure 36:</b> Contours of $f_{r1}$ for (a) the simplified geometry and (b) the 1C compressor (meridional).....	97
<b>Figure 37:</b> Production multiplier for the simplified geometry at 45° and the 1C compressor at 50% streamwise .....	98
<b>Figure 38:</b> Contours of eddy viscosity for the curved section of the simplified geometry. (a) SST model and (b) SST-CC model.....	100
<b>Figure 39:</b> Contours of eddy viscosity for the 1C compressor (meridional contour). (a) SST model and (b) SST-CC model .....	102
<b>Figure 40:</b> Schematic of the measurement locations and the coordinate system used .....	105
<b>Figure 41:</b> Velocity profiles at different streamwise locations along the simplified geometry: (a) Before inlet, (b) 0°, (c) 22.5°, (d) 45°, (e) 67.5° and (f) 90°.....	109
<b>Figure 42:</b> TKE profiles at different streamwise locations along the simplified geometry .....	112
<b>Figure 43:</b> Reynolds $\overline{uu}$ normal stress for 0 – 90° in the simplified geometry .....	116
<b>Figure 44:</b> Reynolds $\overline{vv}$ normal stress for 0 – 90° in the simplified geometry.....	118

<b>Figure 45:</b> Reynolds $\overline{w'w'}$ normal stress for 0 – 90° in the simplified geometry.....	120
<b>Figure 46:</b> Normalized TKE production at streamwise locations along the simplified geometry .....	123
<b>Figure 47:</b> Contour of $f_{r1}$ in the simplified geometry .....	125
<b>Figure 48:</b> Development of the $f_{r1}$ parameter in the 1C, progressing spanwise in the impeller starting at the hub: (a) 5%, (b) 25%, (c) 50%, (d) 75% and (e) 95% span. ....	138

## **LIST OF ABBREVIATIONS, SYMBOLS AND NOMENCLATURE**

---

### ***Abbreviations***

ARSM	Algebraic Reynolds Stress Model
CCV	Concave curvature
CFD	Computational Fluid Dynamics
CVX	Convex curvature
DNS	Direct Numerical Simulation
EVM	Eddy Viscosity Model
FD	Fully Developed
GARDN	Green Aviation Research and Development Network
GGI	General Grid Interface
HW	Hotwire anemometry
LDV	Laser Doppler Velocimetry
LES	Large Eddy Simulation
MFA	Mass-Flow Averaged
NLEVM	Non-Linear Eddy Viscosity Model
P&WC	Pratt and Whitney Canada
PG	Pressure Gradient
PR	Pressure Ratio
PS	Pressure Side of impeller blade
RANS	Reynolds-Averaged Navier-Stokes
RSM	Reynolds Stress Models
RSM-SSG	Reynolds Stress Model – Speziale, Sarkar and Gatski
S-A	Spalart-Allmaras model
SARC	Spalart-Allmaras Rotation and Curvature corrected model
SS	Suction Side of impeller blade
SST	Shear Stress Transport model
SST-CC	Shear Stress Transport – Curvature Corrected model
TKE	Turbulent Kinetic Energy

TG Taylor-Görtler (vortices)

### **Latin Symbols**

$a_{ij}$	Anisotropy tensor (-)
$C_f$	Friction coefficient (-)
$C_p$	Pressure coefficient (-)
$c_a$	Absolute velocity in the axial direction (m/s)
$c_p$	Specific heat capacity at constant pressure (kJ/kg K)
$c_r$	Absolute velocity in the radial direction (m/s)
$c_v$	Specific heat capacity at constant volume (kJ/kg K)
$c_\theta$	Absolute velocity in the circumferential direction (m/s)
$D$	Diameter or term in the $\tilde{r}$ equation (SST-CC model) (m)
$D_h$	Hydraulic diameter (m)
$F_1$	First blending function in the SST model (-)
$F_2$	Second blending function in the SST model (-)
$f_{r1}$	Production multiplier in the SST-CC model (-)
$f_{rotation}$	Argument for the production multiplier, $f_{r1}$ (-)
$H$	Duct height (m)
$h_{0i}$	Specific stagnation enthalpy at location $i$ (kJ/kg)
$h_{is}$	Specific isentropic enthalpy at location $i$ (kJ/kg)
$K_{12}$	Local longitudinal curvature (m <sup>-1</sup> )
$K_w$	Reciprocal of the radius of curvature (m <sup>-1</sup> )
$k$	Turbulence kinetic energy (TKE) (m <sup>2</sup> /s <sup>2</sup> )
$L_e$	Entrance length (m)
$M$	Mach number (-)
$\dot{m}$	Mass flow rate (kg/s)
$\dot{m}_{c1}$	Corrected mass flow rate at the impeller inlet (kg/s)
$\dot{m}_{c1,ref}$	Reference corrected mass flow rate the impeller inlet (kg/s)
$N$	Rotational speed (RPM)
$P_{ij}$	Production of Reynolds stress in RSM-SSG model (kg/ms <sup>3</sup> )



$P_k$	Production of turbulence kinetic energy (kg/ms <sup>3</sup> )
$P_{ri}$	Relative pressure at location $i$ (Pa)
$p$	Pressure (Pa)
$p'$	Fluctuating component of pressure (Pa)
$p_{0i}$	Total Pressure at location $i$ (Pa)
$p_s$	Static pressure (Pa)
$Q$	Heat transfer (W)
$R$	Specific gas constant (J/kg K)
$R_c$	Radius of curvature (m)
$Re$	Reynolds number (-)
$Re_{D_h}$	Reynolds number based on hydraulic diameter (-)
$Re_H$	Reynolds number based on duct height (-)
$Re_N$	Reynolds number based on rotational speed (-)
$Re_\theta$	Reynolds number based on momentum thickness (-)
$R_f$	Flux Richardson number (-)
$r$	Radial direction in cylindrical coordinates (m)
$\vec{r}$	Vector connecting the integration point and upwind node (m)
$r^*$	Term in $f_{rotation}$ equation; ratio of strain and rotation tensors (-)
$\tilde{r}$	Term in $f_{rotation}$ equation (-)
$r_i$	Annulus inner radius (m)
$r_o$	Annulus outer radius (m)
$S$	Magnitude of the strain rate tensor (s <sup>-1</sup> )
$S_{ij}$	Strain rate tensor (s <sup>-1</sup> )
$s$	Arc length (m)
$T_{0i}$	Total temperature at location $i$ (K)
$T_{is}$	Isentropic temperature at location $i$ (K)
$T_s$	Static temperature (K)
$U_i$	Mean velocity component in the $i$ th direction (m/s)
$U_2$	Blade tip speed (m/s)

$U_{inlet}$	Velocity in x direction at the simplified geometry inlet (m/s)
$u_i$	Turbulent fluctuating velocity in the $i$ direction (m/s)
$u^+$	Non-dimensional velocity for the law of the wall (-)
$\overline{u_i u_j}$	Turbulent Reynolds stress in the $i$ and $j$ directions ( $m^2/s^2$ )
$x$	Cartesian coordinate direction or tangential direction in curvilinear coordinates (m)
$x_i$	Cartesian coordinate in the $i$ th direction (m)
$y$	Cartesian coordinate direction or normal direction in curvilinear coordinates (m)
$y^+$	Non-dimensional wall height (-)
$z$	Cartesian coordinate direction or transverse direction in curvilinear coordinates (m)

### ***Greek Symbols***

$\alpha$	Absolute flow angles ( $^\circ$ )
$\gamma$	Ratio of specific heat capacities ( $c_p/c_v$ ) (-)
$\delta$	Boundary layer thickness (m)
$\delta_{ij}$	Kronecker delta (-)
$\epsilon$	Turbulence dissipation rate ( $m^2/s^3$ )
$\epsilon_{ijk}$	Permutation symbol (-)
$\zeta$	Spanwise coordinate from concave to convex surfaces in simplified geometry; hub to shroud in centrifugal cases (-)
$\eta$	Efficiency in the Hutton and Ackeret correlations (-)
$\eta_m$	“Model” efficiency in Hutton and Ackeret correlations (-)
$\eta_{ts}$	Total-to-static efficiency (-)
$\eta_{tt}$	Total-to-total efficiency (-)
$\theta$	Streamwise position along simplified geometry for center of curvature ( $^\circ$ )
$\mu$	Dynamic viscosity (kg/ms)
$\mu_t$	Eddy viscosity (kg/ms)
$\nu$	Kinematic viscosity ( $m^2/s$ )

$\rho$	Density (kg/m <sup>3</sup> )
$\Phi_{ij}$	Pressure-strain correlation term in the RSM-SSG model, $\Phi_{ij} = \Phi_{ij,1} + \Phi_{ij,2}$ (kg/ms <sup>3</sup> )
$\Phi_{ij,1}$	1 <sup>st</sup> part of pressure-strain correlation term (kg/ms <sup>3</sup> )
$\Phi_{ij,2}$	2 <sup>nd</sup> part of pressure-strain correlation term (kg/ms <sup>3</sup> )
$\Omega$	Magnitude of the rotation rate tensor (s <sup>-1</sup> )
$\Omega_{ij}$	Rotation rate tensor (s <sup>-1</sup> )
$\Omega^{rot}$	System rotation rate (rad/s)
$\omega$	Specific dissipation rate (s <sup>-1</sup> )

### ***Operators***

$D/Dt$	Lagrangian derivative (or total derivative)
$\partial/\partial t$	Partial derivative with respect to time
$\partial/\partial x_i$	Partial spatial derivative with respect to the $i$ th direction
$N$	Navier-Stokes operator (component of equation)

### ***Subscripts, superscripts and accents (variable $\phi$ )***

$\phi_{ip}$	$\phi$ at the integration point
$\phi_{up}$	$\phi$ at the upwind node
$\phi_0$	Stagnation quantity of $\phi$
$\phi_1$	$\phi$ at location 1 (impeller inlet)
$\phi_2$	$\phi$ at location 2 (impeller exit)
$\phi_3$	$\phi$ at location 3 (diffuser inlet)
$\phi_4$	$\phi$ at location 4 (diffuser exit)
$\bar{\phi}$	Time averaged value of $\phi$

## 1. INTRODUCTION

---

In the present drive to make the aircraft industry more environmentally friendly, one of the current key concerns is reducing emissions of both noise and exhaust pollutants. This work focuses on one of a series of projects funded by Canada's Green Aviation Research and Development Network (GARDN) with the goals of reducing the impact of the aerospace industry on the environment. GARDN focuses on seven different research themes: source noise reduction, source emissions reduction, materials and manufacturing processes, airport operations, aircraft operations, alternative fuels and product lifecycle management. Within this context, the aim of this research is to improve the overall performance of Canadian aircraft engines designed by Pratt and Whitney Canada (P&WC). This will be accomplished by developing a better understanding of their internal aerodynamics, specifically in regions within the engine where the airflow is strongly turned (high curvature). Curvature exists in many regions of an aero-engine, however a specific focus will be directed towards the centrifugal compressor stage in P&WC's small scale compact engines. A further understanding of the flow physics and the effects of curvature in this region will lead to more compact designs, resulting in a higher efficiency and reduced weight; all to provide greener engine operation.

In addition to the investigation of curvature within a centrifugal stage in an aero-engine, the effects of curvature will also be investigated in a general sense. Curvature is present in many turbulent engineering flows, with one specific example being in turbomachinery applications. Whether it is, for example, the curvature of the blades in an axial machine, or the axial to radial transition in a centrifugal machine, curvature will exist somewhere in the system in most applications. An important part of understanding the flow physics in these machines is identifying and knowing how to deal with any curvature effects. This becomes particularly relevant when using computational fluid dynamics (CFD) modeling techniques. Curvature introduces an extra level of complexity that can greatly affect the flow

structure and turbulence quantities, which needs to be accounted for when considering the implementation of turbulence models.

Turbulence modelling techniques have been studied by numerous researchers since their initial development. There are a variety of different turbulence models, however eddy viscosity models are the most popular and practical branch of turbulence models for industrial applications. These models focus on the mean quantities and use various approximations to simulate the details, such as the turbulent quantities. Since this research focuses on industrial applications, these models will be emphasized and outlined in detail herein. Different eddy viscosity turbulence models will be investigated and evaluated based on their performance to predict flows with high curvature. The main focus of this work is on a curvature corrected version of the SST model (SST-CC) that was recently developed by Smirnov and Menter (2009). This model has performed well for various test cases with curvature, and although the comparisons demonstrate the effectiveness of the SST-CC model for these cases, an in-depth investigation of the turbulence effects relative to the uncorrected SST model has not been published. Thus, the present research attempts to further analyze the SST-CC model and improve the understanding of the flow physics by isolating and deconstructing the turbulent quantities in both the uncorrected SST model as well as the corrected SST-CC model.

In the following chapters, three separate cases will be examined to investigate the performance of the SST-CC model. The first two cases are centrifugal compressors designed by P&WC. The first is a compressor stage (307C) that was analyzed previously using numerical simulations and LDV experiments by Bourgeois et al. (2011). This compressor stage consists of a tandem bladed impeller and a “fish tail” style diffuser, located after a series of axial compressor stages and before the combustor and turbine regions in the aero-engine, as shown in Figure 1. The main advantage to having a centrifugal stage at this location in the engine is to achieve a high pressure increase, without increasing the size of the engine, thus reducing weight, resulting in fuel savings in the long term. Curvature corrected models will be benchmarked against the completed experiments in terms of overall

performance characteristics as well as against the detailed flow fields. The second case will be another centrifugal stage (1C) currently in development by P&WC. This stage is similar to the previous centrifugal compressor in terms of location in the aero-engine, however it consists of a more compact geometry in both the impeller and the diffuser portions, thus creating a highly curved flow. This centrifugal compressor will be compared to the third and final case: a simplified geometry case consisting of a curved geometry with a similar curvature and flow condition to the 1C compressor impeller geometry. The simplified geometry allows for a simplification of the complex flow in a centrifugal compressor to isolate the effects of curvature from any other mechanisms present in the compressor flow. All three of these cases are useful in determining the effectiveness of a curvature corrected model, as well as providing an evaluation of the potential industry benefits in the improvement of the accuracy of CFD modelling for future turbomachinery components with high curvature.

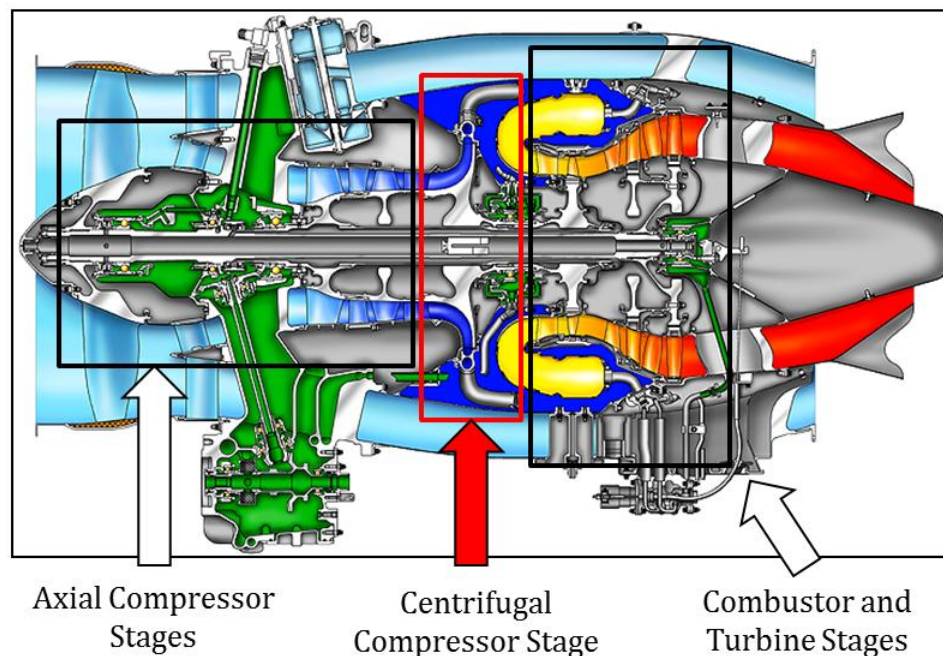


**Figure 1: Cross section of a Pratt and Whitney Canada aero-engine (c/o P&WC)**

### ***1.1 Scope and objectives of the present work***

The overall scope of this work entails examining the effects of curvature from the perspective of turbulence modelling with the objectives of developing an improved understanding of the flow phenomena associated with curvature in general, determining how curvature corrected turbulence models account for these phenomena and thoroughly investigating the use of the SST-CC model in centrifugal compressor cases with high curvature. Smirnov and Menter (2009) have previously investigated the SST-CC model performance in various simplified test cases by comparing against experimental data, however their focus was primarily on mean quantities. This work expands on the work of Smirnov and Menter (2009) by further investigating the underlying flow mechanisms and effects due to curvature and the relationship between curvature effects and the formulation of the SST-CC model. Furthermore, this work expands on the investigation of the use of this model in turbomachinery applications by testing the SST-CC model in detail for two compressor cases, considering flow fields as well as global performance.

Therefore, the objectives of this work are accomplished by evaluating the performance of the SST-CC turbulence model, as compared to the original uncorrected SST model and the more curvature sensitive RSM-SSG model, in terms of detailed global performance and local flow characteristics for two different centrifugal compressor cases and a simplified geometry. The simplified geometry uses a curved section, modelled after a centrifugal impeller with high curvature, with the purpose of eliminating the complex flow properties in a centrifugal impeller to direct the focus towards curvature effects and the prediction of said curvature effects by the SST-CC model.

The completion of this work is beneficial in terms of developing a deeper understanding of the underlying mechanisms in the SST-CC model in regards to curvature effects. Moreover, it provides valuable performance characteristics for new and future compressors designs for the advancement of the Canadian

aerospace industry, and further validates the use of the SST-CC turbulence models in other turbomachinery applications.

## **1.2 Organization of the thesis**

This work considers the effects of curvature with respect to turbulence and flow mechanisms and discusses the performance of different curvature corrected turbulence models in predicting these curvature effects using three different test cases. The thesis is organized as follows.

Firstly, Chapter 2 outlines some basics of compressors in terms of types, functionality and performance evaluation. Chapter 3 presents a literature review which discusses curvature effects on turbulent flows in terms of curvature magnitude, curvature directionality (concave vs. convex), Reynolds number ( $Re$ ) and pressure gradients. It also presents the governing equations associated with commonly used turbulence models in industry as well as discusses the turbulence models studied in this work, with a specific focus on the SST-CC model by Smirnov and Menter (2009). Chapter 3 continues with a review of recent advancements in correcting eddy viscosity turbulence models to account for curvature, and closes with an evaluation of the performance of common turbulence models in other turbomachinery applications. Chapter 4 describes the geometry and numerical setup for the two (307C and 1C) centrifugal compressor test cases. The computational setups for both compressors are discussed concurrently since there are many similarities between the two. Chapter 5 introduces the numerical setup of the simplified geometry test case, which is an idealized version of the 1C centrifugal compressor geometry. Chapter 6 presents the numerical and experimental comparison for the 307C compressor case. Comparisons are made between three different turbulence models used in terms of global performance and in terms of flow field prediction. Chapter 7 presents the results from the 1C compressor case. A comparison is made between turbulence models in terms of global performance parameters and to the simplified geometry in terms of flow field and the prediction of the appropriate curvature effects. Chapter 8 presents some additional



investigations in terms of the simplified geometry flow field and turbulence quantities. Chapter 9 states the conclusions of the study and summarizes the work. Finally, Chapter 10 outlines the recommendations for future work.

### ***1.3 Summary***

Background information as well as the scope and objectives of the current work were introduced in this chapter. This project is within the scope of GARDN, with the overall goal of improving the efficiency of aero-engines, thus reducing emissions and the negative environmental impact. The scope of this research was to expand on the work of Smirnov and Menter (2009) by investigating their SST-CC model in terms of the predicting of the underlying mechanisms caused by curvature, with the objectives of improving the understanding of the formulation of the SST-CC model and further validating it for use in turbomachinery applications. This is completed by considering two centrifugal compressor test cases and a simplified geometry. The chapter closed with a discussion on the organization of the thesis. The next section discusses some basics of turbomachinery, with a specific focus on compressors.

## **2. TURBOMACHINERY BACKGROUND**

---

This chapter introduces some of the different types of compressors (axial, mixed flow and centrifugal), describes basic concepts relating to compressor operation, briefly discusses the advantages and disadvantages of different compressor types and finally, describes techniques used to evaluate compressor performance.

### ***2.1 Compressor types***

The three main types of rotating compressors used in industrial applications are axial, mixed flow and centrifugal compressors. The names are derived from the primary flow direction; in axial compressors, the primary flow is axially along the machine axis; in centrifugal compressors, the primary exit flow is in the radial direction, and in mixed flow compressors, the flow exiting is neither fully axial nor fully radial, but is a combination of the two directions. From this point forward, the focus will be directed towards axial and centrifugal compressors.

### ***2.2 Basics of operation***

All types of rotating compressors have the same final goal: a pressure rise from inlet to outlet. Similarly, all types use the same general concept: increase the velocity of the working fluid, thereby increasing the kinetic energy, and then diffuse the high velocity, converting the kinetic energy into pressure energy. However, the methods of increasing the velocity and converting it to pressure energy are where differences arise between the two types.

#### ***2.2.1 Axial compressors***

In axial compressors, alternating rows of “rotors” and “stators” are used to increase the flow velocity and diffuse the high velocity into high pressure, respectively. The rotor consists of multiple rotating blades, whereas the stator consists of a series of stationary blades that redirect the flow, which increases the flow pressure. Each of the rotor-stator pairs are known as a compressor stage. Across each stage there is a

relatively small pressure rise, usually 1.1:1 – 1.4:1 (Boyce, 2003, p. 6), so generally multiple stages are required to obtain the desired pressure rise.

### 2.2.2 Centrifugal compressors

In centrifugal compressors, a rotating impeller is paired with a stationary diffuser to produce the pressure rise across the stage. The impeller is curved from the axial to radial direction, increasing the velocity of the flow using an outward centrifugal force, in combination with the rotating blades. On exiting the impeller, the flow enters the stationary diffuser, consisting of a series of gradually expanding vanes (or sometimes, pipes), which redirect the flow and convert the kinetic energy into pressure energy. Often, in centrifugal compressors, the pressure rise is designed to be equally split between the impeller and diffuser sections (Boyce, 2003, p. 9).

### 2.3 Compressor selection

Compressors are typically selected depending on the required pressure ratio, mass flow, efficiency and size. Table 1 lists some typical characteristics for axial and centrifugal compressors for three typical applications: industrial, aerospace and research (Boyce, 2003, p. 5). Note that for both compressors, the operating range will depend on the pressure ratio magnitude, and decreases with increasing pressure ratio.

**Table 1: Typical characteristics for axial and centrifugal compressors, adapted from (Boyce, 2003, p. 5)**

Compressor Type	Pressure Ratio			Efficiency	Operating Range
	Industrial	Aerospace	Research		
<b>Axial</b>	1.05 – 1.3	1.1 – 1.45	2.1	80 – 91%	Narrow 3 – 10%
<b>Centrifugal</b>	1.2 – 1.9	2.0 – 7.0	13	75 – 87%	Large 25%

From Table 1, it can be seen that axial compressors are advantageous for applications with lower pressure ratios (1.05 – 2.1). Due to the low pressure rise across each stage, they are very efficient, but they also have a narrow operating

range. Furthermore, to use an axial compressor for a large pressure rise, many stages will be necessary, which will increase the size of the machine.

Centrifugal compressors are capable of a range of pressure ratios, from low to high (1.2 – 13), as seen from Table 1. They are generally less efficient than axial compressors, but provide a larger operating range and are ideal for applications where space is limited, since they can achieve a large pressure rise in a relatively small volume.

From these characteristics, it is clear that the choice of compressor depends on the system requirements including the pressure ratio, flow rates, efficiency and size. P&WC, for example, use both axial and centrifugal stages in their aero-engines, since the characteristics of both types are beneficial in different regions of the engine.

#### ***2.4 Compressor performance evaluation***

Two commonly used performance evaluations for turbomachinery, which are used in this work, are characteristic curves and efficiency lines. Characteristic curves for compressors, also known as speedlines, provide information about the pressure ratio (PR) at different mass flow rates for different rotational speeds. This is a commonly used chart when either evaluating the performance of a specific operating point, or selecting a compressor for an industrial application. Efficiency lines present information about the overall efficiency of the compressor stage along a range of mass flow rates. This is useful for selecting the most efficient operating point for the compressor, as well as for estimating the efficiency at off-design points. Further details on both speedlines and efficiency lines are discussed in the following sections, after a brief note on subscripts.

##### ***2.4.1 Subscripts in compressors***

Herein, various subscripts are used to describe different key locations in the compressor stages studied. These locations are the impeller inlet, the impeller exit, the diffuser inlet and the diffuser outlet. The subscripts associated with these locations are outlined in Table 2.

Table 2: Key locations in the compressor stages and their associated subscripts

Location	Subscript
Impeller Inlet	1
Impeller Exit	2
Diffuser Inlet	3
Diffuser Exit	4

#### 2.4.2 Characteristic curves (speedlines)

A speedline is a plot of pressure ratio (PR), generally from impeller inlet to diffuser exit (location 1 to 4), for different mass flow rates. The speedline can be broken down into three main regions: the design region, the choke region and the stall/surge region, as shown in Figure 2. The choke and the stall/surge regions are on opposite ends of the compressor speedline and represent the two operating limits of the compressor stage.

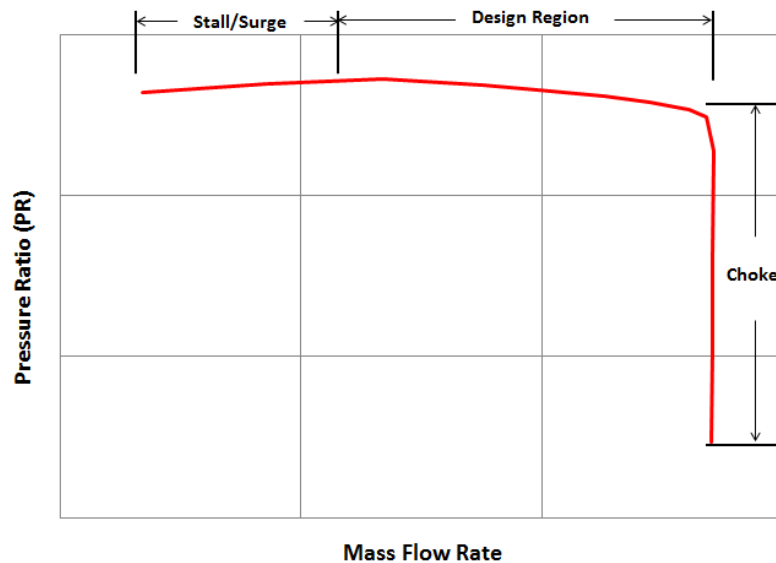


Figure 2: Example of the different flow regions on a compressor characteristic curve

When a compressor is at the choke condition, the pressure ratio and efficiency drop drastically with little to no change in flow rate. In modern compressors, running in choke will not cause compressor damage (Brun & Kurz, 2009). However it is very

impractical to run compressors in the choke condition because of the drop in PR and efficiency. When a compressor is operating in the stall/surge condition, a complete flow reversal can occur, which results in a complete loss of pressure rise and can cause serious damages due to large forces on the compressor (Boyce, 2003, p. 5).

The terms stall and surge are sometimes used interchangeably, and are phenomena that occur in the same mass flow region (low mass flows). Stall is simply a precursor to surge, where the flow starts to separate in different regions in the compressor stage (Brun & Kurz, 2009). Surge will occur once the separation reaches a critical point and rapid backflow occurs through the compressor stage.

### 2.4.3 Efficiency lines

Efficiency lines provide information about the machine efficiency at different mass flow rates, which is useful for determining the optimal operating point. A turbomachine's overall efficiency is generally evaluated using either the total-to-total efficiency or the total-to-static efficiency. The total-to-total efficiency (Eq. 2.1) (Dixon & Hall, 2010, p. 18) is used when the kinetic energy at the outlet is useful, whereas the total-to-static efficiency (Eq. 2.2) (Dixon & Hall, 2010, p. 18) is used if the kinetic energy at the outlet is wasted. An example where the kinetic energy is useful is the exit turbine stage of an aircraft engine, where the kinetic energy is used for propulsion (Dixon & Hall, 2010, p. 16).

$$\eta_{tt} = \frac{h_{04s} - h_{01}}{h_{04} - h_{01}} \quad (2.1)$$

$$\eta_{ts} = \frac{h_{4s} - h_{01}}{h_{04} - h_{01}} = \frac{c_{p,4}T_{4s} - c_{p,1}T_{01}}{c_{p,4}T_{04} - c_{p,1}T_{01}} \quad (2.2)$$

In the compressor cases studied herein, the kinetic energy is wasted by being slowed down at the diffuser into a combustor, making the total-to-static efficiency the appropriate efficiency to use. Recall, in Eqs. 2.1 and 2.2, the subscript '1' represents the machine inlet (impeller inlet) and '4' represents the machine exit (diffuser exit). In this case, enthalpy values are calculated using mass flow averaged

$c_p$  values at each location in conjunction with stationary reference frame temperatures and  $T_{4s}$  is found using ideal gas tables (Cengel & Boles, 2006, p. 936) based on the compressor pressure ratio. A sample calculation of the total-to-static efficiency (Eq. 2.2) in the centrifugal cases studied later in this work can be found in Appendix I, §A.

## **2.5 Summary**

The basics of turbomachinery were discussed, including different compressor types, operating principles and performance characteristics. The next chapter presents a literature review in four different branches: curvature effects in turbulent flows, turbulence modelling techniques, the performance of different turbulence models with respect to curvature and finally, a discussion on turbulence modelling in turbomachinery applications.

### 3. LITERATURE REVIEW

---

The following sections describe various topics relating to curvature, turbulence modelling and turbomachinery. First, completed research on the effects of curvature on turbulent flows will be discussed. This will include descriptions of the physical effects of curvature with past experimental work backing up the details. Second, the theory behind different turbulence models used in industrial applications is discussed in terms of governing equations, and in terms of the models specifically used in this study. Third, different turbulence models are evaluated in terms of their ability to predict curvature effects, and the performance of different “curvature corrected” models is analyzed. Finally, a connection is made between turbulence modelling and turbomachinery, specifically in terms of model performance in turbomachinery, with a brief discussion of the difficulties associated with modelling turbomachinery flows.

#### 3.1 Curvature effects

A surface can have curvature in three orthogonal directions: the longitudinal or tangential ( $x$ ), normal ( $y$ ) and transverse ( $z$ ) directions as shown in Figure 3. In each of these directions, the surfaces can be curved in a convex (CVX) direction, a concave (CCV) direction, or some combination of the two directions.

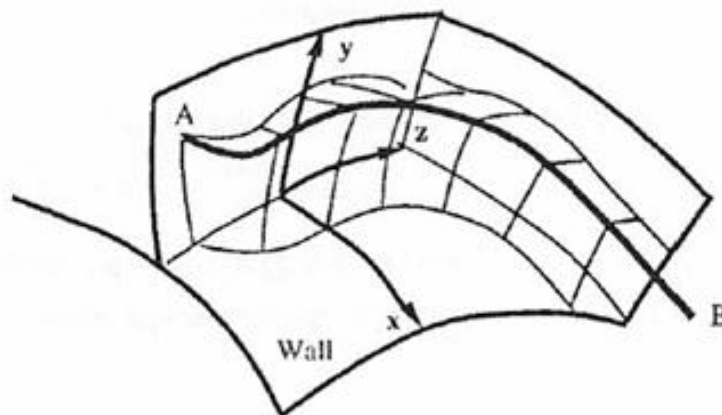


Figure 3: Diagram of different curvature directions (Piquet, 1999, p. 563)



A common type of curvature that has many practical applications is in the tangential direction, which can be referred to as streamwise curvature (herein denoted simply by “curvature”), which will be the focus of this work. Curvature exists in many applications such as in a curved duct, in turbomachinery blades, or in flows over other types of aerofoils. These are only a few examples, but many types of engineering flows will have some form of curvature.

Bradshaw (1973) describes the effects of curvature as an “extra rate of strain”,  $\partial V/\partial x$ , to the already present principal strain,  $\partial U/\partial y$ . A review of the literature reveals that the overall effect of this “extra rate of strain” depends on many factors that include: the magnitude of the curvature, the directionality of the curvature (CVX or CCV), the Reynolds number ( $Re$ ) and the presence of streamwise pressure gradients (PG). All of these factors must be taken into consideration when analyzing a flow with curvature.

### 3.1.1 *Magnitude of curvature effects*

As discussed in a review of curvature effects by Patel and Sotiropoulos (1997), the curvature magnitude can be described by the ratio of the boundary layer thickness ahead of the curved surface,  $\delta$ , to the radius of curvature,  $R_c$ . Thus, the magnitude is described by the product  $K_w\delta$ , where  $K_w$  is the local wall curvature ( $K_w = 1/R_c$ ). According to Bradshaw (1973), curvature effects can begin to appear for a  $K_w\delta$  as small as  $10^{-2}$ , whereas other terms are of order 1. In this regard, there is a general rule of thumb for the magnitude that  $K_w\delta = 0.01$  denotes weak curvature, 0.1 denotes moderate curvature and 1.0 denotes strong curvature, however these values are not widely accepted (Patel & Sotiropoulos, 1997). Piquet (1999, p. 564) also states that “the effects on the flow are considerably larger than the one presumed by these orders of magnitude”, which suggests that the  $K_w\delta$  representation is, perhaps, not an overly realistic method of evaluating the magnitude of curvature effects.

Another parameter that can be used to describe the relative importance of the curvature in the flow is the flux Richardson number,  $R_f$ , given by Eq. 3.1 (Piquet,

1999, p. 570). It is a non-dimensional parameter that represents the ratio of the curvature production to the primary shear production.

$$R_f = \frac{K_{12}U}{\partial U/\partial y} \quad (3.1)$$

In Eq. 3.1,  $K_{12}$  is the local “longitudinal curvature” (Eq. 3.2),  $U$  is the mean flow velocity in the  $x$ -direction,  $\partial U/\partial y$  is the primary shear and in Eq. 3.2,  $y$  is the distance to the location of interest, normal to the wall. Figure 4 shows the curvilinear coordinate system used for these definitions, where  $r$  represents the radial distance to the point of interest and  $r_o(x)$  represents the radial distance to the surface.

$$K_{12} = \frac{K_w}{1 + K_w y} \quad (3.2)$$

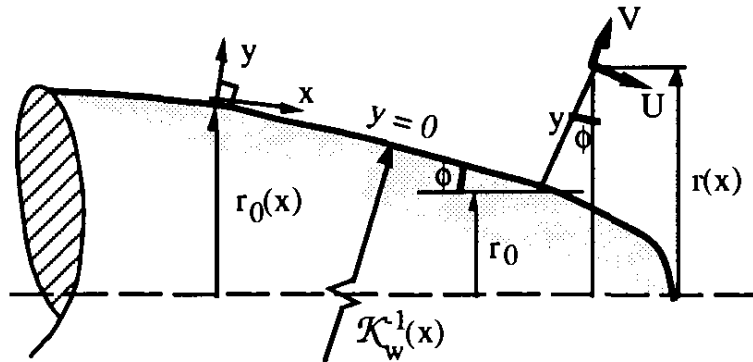


**Figure 4: Coordinate system and variable definition for a curved surface (Piquet, 1999, p. 565)**

$R_f$  gives a relative sense of the importance of the curvature from a local perspective and provides both a quantitative and qualitative description of the curvature effects, whereas the previous  $K_w\delta$  method provides a measure of the curvature effects from a global perspective. For example, qualitatively it can be seen from Eq. 3.1 that if  $R_f$  is locally high, curvature effects are very important as they dominate the ratio. On the contrary, if  $R_f$  is locally low, the curvature effects are less important as compared to the primary shear (Piquet, 1999, p. 570). On the other hand, with  $K_w\delta$ , one can deduce the general importance of curvature on the flow based on the boundary layer thickness prior to curvature, however there is no information on the

local importance of curvature at any given location. Thus, each of the methods has a useful purpose for defining curvature magnitude effects.

### *3.1.2 Curvature directionality effects*

A curved surface can be curved in either a convex or a concave direction. This difference, which will be described as the directionality of the curvature, dictates the turbulent structure, the variation in turbulent quantities and the velocity profile, therefore making it the most important aspect to consider when analyzing curvature effects. It is often quoted in the literature that the effects of convex and concave curvature are opposite and asymmetric (Piquet, 1999, p. 570), however as will be described in the following sections, the physics are very different in these two types of curvature. The following two sections will outline the important effects on a turbulent flow due to convex and concave curvatures, respectively.

#### *3.1.2.1 Convex (CVX) curvature*

There are many examples of convex curvature in engineering applications, with a specific example being the flow over a nose cone. The main effects on turbulence with flow over a convex surface are a reduction in shear stress, a reduction in turbulent kinetic energy and a reduction in turbulent mixing. Thus, it is frequently stated that convex curvature is a “stabilizing” curvature, since it tends to suppress turbulence (Patel & Sotiropoulos, 1997). The reasoning behind the stabilizing effect can be explained by considering an element near the convex wall. Due to the curvature, there is a centrifugal force acting on the fluid element, which can be different on two different radial streamlines because of the radial velocity gradient. If a turbulent fluctuation then acts on the fluid and a fluid element is shifted from one streamline to another, there will be a net centrifugal force. In the case of the convex curvature, the net centrifugal force is opposite to the shifting motion, resulting in a turbulence suppression (or stabilization) (Kozulovic & Rober, 2006 and Xu et al., 2008).

The preceding analogy explains the reduction in turbulent energy, however it does not discuss the shear stress reduction or the reduction in turbulent mixing. Near a convex surface, the boundary layer tends to separate into sub-layers, with the inner layer showing a large reduction in shear stress. In fact, there is generally a point in the boundary layer where the shear stress can completely vanish (Patel & Sotiropoulos, 1997). As for the reduction in turbulent mixing, this is likely due to the reduction of turbulent energy. When there is less turbulent energy in the flow there is bound to be less turbulent mixing because there will be less swirling flow (i.e. turbulent vorticity).

In terms of turbulent structure, there seems to be a lack of information for convex curvatures. There was a brief discussion by Kim & Patel (1994) that strong prolonged curvature can lead to longitudinal vortices on the convex wall, however as confirmed by the review of longitudinal curvature by Patel and Sotiropoulos (1997), there is a need for more data in this regard.

### *3.1.2.2 Concave (CCV) curvature*

As stated previously, the effects of concave curvature are opposite to the effects of convex curvature; concave curvature tends to increase the shear stress, increase the turbulent kinetic energy and increase the turbulent mixing, whereas in the convex case, all these quantities are decreased (Patel & Sotiropoulos, 1997). This increase in turbulence is why concave curvature is generally regarded as "destabilizing" curvature. In other words, it disorganizes the mean flow by the introduction of higher turbulence levels. As compared with the fluid element analogy, as stated in the convex curvature section, the net centrifugal force and the shifting motion are in the same direction, which is the reasoning for the turbulence destabilization near concave surfaces (Kozulovic & Rober, 2006 and Xu et al., 2008).

Although the effects of concave and convex curvature are often described as opposite and asymmetric, the physical structures involved in concave turbulence are stated as being quite different from those in convex curvature (Piquet, 1999). One main structure found by many researchers is the formation of Taylor-Görtler

(TG) style vortices (see Figure 5) that appear on the concave surface at a certain limit of curvature. The wording “Taylor-Görtler style” is used because there is some argument as to whether these structures are actually TG vortices or “longitudinal roll cells”. Longitudinal roll cells are simply regions of highly extended fluid in the flow direction, with limited lifetime and no well-defined cores (Piquet, 1999).

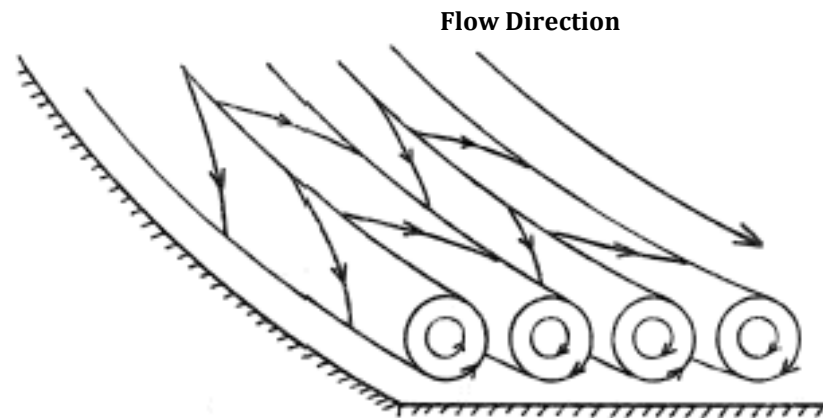


**Figure 5: Taylor-Gortler style vortices that form in the presence of concave surfaces**  
 (from <http://www.thermopedia.com/content/817/?tid=104&sn=1412>)

Regardless of the type of vortex, these vortices produce secondary flows proportional to the magnitude of the radial pressure gradient (Munch & Métais, 2007) which greatly complicate the flow patterns and make the flow over a concave surface fully three dimensional. In regards to secondary flows, Munch and Metais (2007) completed an LES study on curved ducts of varying radii of curvature and confirmed that the intensity of the secondary flows increases with decreasing radius of curvature (see Figure 6). Figure 6 clearly shows that with decreasing radius of curvature (increasing curvature magnitude), there is an increase in the maximum secondary flow intensity,  $I_{max}$ .

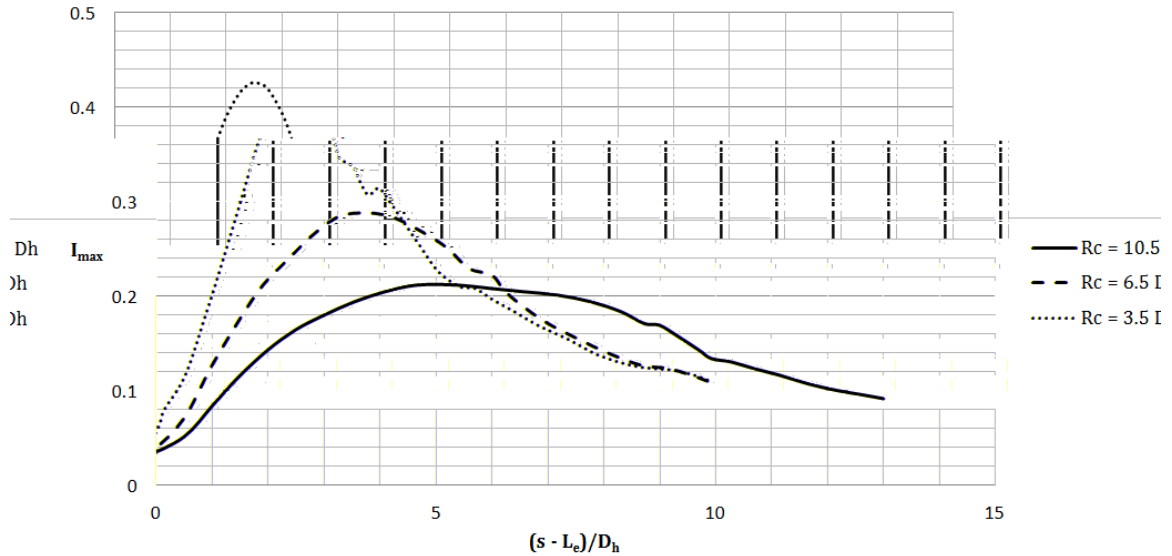


**Figure 6: Maximum secondary flow intensity as a function of downstream distance along a curved channel for different radii of curvature in an LES study by Münch & Metais (2007).  $D_h$  is the hydraulic diameter of the duct, and  $s$  is the arc length.**

### 3.1.3 Effect of Reynolds number ( $Re$ ) on curvature

In general, the relationship between  $Re$  and curvature effects seems to be relatively unknown. It has been stated that any speculation on the effects of curvature at high  $Re$  should be made with caution (Patel & Sotiropoulos, 1997). This can be confirmed by the summary of experiments completed in curved ducts given in Table 3, compiled by Mokhtarzadeh-Dehghan and Yuan (2003). One of their conclusions was that most experiments have used a lower  $Re_H$ , within a relatively narrow range, and that a gap existed at higher  $Re_H$  values. Thus, Mokhtarzadeh-Dehghan and Yuan (2003) measured a developing flow through a square cross section curved duct using hot wire anemometry at a higher  $Re_H$  of  $3.6 \times 10^5$ . Unfortunately, despite showing typical curvature effects as described in the previous sections, the researchers did not mention any additional effects due to using a higher  $Re_H$ , as this was not the primary goal of their research. Consequently, it appears that, based on the tabled information, there is still a gap in the description of curvature effects for  $Re_H$  at or above  $3.6 \times 10^5$ . This region could be further investigated experimentally, ideally using non-intrusive methods to fully characterize the flow without any disturbances. Additionally, a numerical investigation could be conducted but would

require using eddy-viscosity models, since a LES or DNS study at a  $Re_H$  this high would be impractical. The author postulates that with increasing  $Re$ , the flow should become increasingly complex, with higher secondary flows and increased vorticity; however this is just speculation. Further knowledge of curvature effects in a higher  $Re$  region would be valuable for applications such as turbomachinery, or similar applications with high  $Re$ .

**Table 3: Summary of previous experiments completed in terms of curvature magnitude, curvature directionality, the Reynolds number and the presence of pressure gradients (Mokhtarzadeh-Dehghan & Yuan, 2003)**

	$R_c/H$	$W/H$	$\delta/H$	$\delta/R_c$	$\theta^\circ$	$Re_H$	$Re_\theta$		Method
<b>So and Mellor (1973)</b>		8.0 <sup>a</sup>		$\approx 0.01$		20,300		CVX	HW
<b>Ellis and Joubert (1974)</b>	6 & 30	13.2						CCV & CVX +PG	P
<b>Meroney and Bradshaw (1975)</b>	20	6		0.02				CCV & CVX +PG	HW
<b>Ramaprian and Shivaprasad (1978)</b>	$\approx 25$	2.5		0.01				CCV & CVX +PG	HW
<b>Hunt and Joubert (1979)</b>	100	13.2				30,000, 60,000 & 130,000		CCV & CVX	HW
<b>Smits et al. (1979)</b>	1.0 (CVX)	6.0	0.165	0.083 (CCV)	20			CCV & CVX +PG	HW
	2.0 (CCV)			0.165 (CVX)	30				
<b>Humphrey et al. (1981)</b>	1.8 (CVX)	1.0		0.053 (CCV)	90	40,000		FD	LDV
	2.8 (CCV)			0.083 (CVX)					
<b>Taylor et al. (1982)</b>	1.8 (CVX)	1.0		0.053	90	40,000		PG	LDV
	2.8 (CCV)								
<b>Enayat et al. (1982)</b>	7.5 (CCV)	1.0	0.14	0.0186 (CCV)	90	35,200		CCV & CVX	LDV
	6.5 (CVX)			0.0215 (CVX)					
<b>Gillis and Johnson (1983)</b>	0.9	2.54		0.05, 0.1	90		3378	CVX	HW
<b>Muck et al. (1985)</b>	19 (CVX)	6.0		0.009			5000	CVX + PG	HW
<b>Hoffman et al. (1985)</b>	20 (CCV)	6.0		0.009			5000	CCV + PG	HW
<b>Johnson and Launder (1985)</b>	3.35	1.0			180	$5.6 \times 10^4$		CCV & CVX +PG	LDV
<b>Barlow and Johnson (1988)</b>				0.056 – 0.088	90		1140	CVX, PG $\approx 0$	LDV

Iacovides et al. (1990)	6.6	1.0		0.02		58,000			
Kim and Patel (1994)	3.5	6.0		0.02	90	224,000		CCV, PG	
Gibson and Servatjoo (1989)		5.6	0.2		30			CVX	
Alving et al. (1990)		8.0		0.08		$3.0 \times 10^5$	6000	CVX	
Yamaguchi (1992)	3.3	4.0			180	$1.8 \times 10^5$	1160	PG, CCV & CVX	
Moktarzadeh et al. (2003)	1.17	1.0	0.069 (CCV)	0.041 (CCV)	90	360,000	2515	PG	E
			0.036 (CVX)	0.054 (CVX)			1324		

Note: CCV = concave, CVX = convex, PG = existing pressure gradient, R = radius of curvature, W = width (spanwise), H = height (normal), FD = fully developed flow, HW = hot-wire anemometry, P = other probes, LDV = Laser Doppler velocimetry

### 3.1.4 Effect of streamwise pressure gradients on curvature

When analyzing the effects of curvature, researchers must consider streamwise pressure gradient effects. Streamwise pressure gradients are generally present with surface curvatures and result in similar effects (Piquet, 1999, p. 564). In fact, favourable pressure gradients can simulate concave curvature effects and adverse pressure gradients can simulate convex curvature effects (Patel & Sotiropoulos, 1997). In connection with pressure gradient effects, many researchers have investigated the flow through curved duct style geometries; some of which isolate pressure gradients from curvature and specifically investigate the effects of curvature as compared to the effects of pressure gradients, and some of which simply accept the presence of additional pressure gradients. In regards to these studies, Kim and Patel (1994) state that: “in some cases, attempts were made to remove the attendant pressure gradients and isolate the effects of curvature, while in others, the pressure gradient effects were not documented and were generally ignored”. This has also been confirmed in Table 3, in which some experiments have pressure gradients (PG) and some do not. An example of isolation of pressure gradients is in the work of So and Mellor (1973). So and Mellor used a gradually expanding wind tunnel test section (see Figure 7), which was designed to eliminate strong pressure gradients, with the intent of focussing solely on curvature effects. In contrast, Kim and Patel (1994) performed an experiment with developing turbulent flow through a rectangular 90 degree bend, and did not strictly isolate any



streamwise pressure gradients. Table 3 (Column 9) indicates whether or not a streamwise pressure gradient (PG) was present in previous studies. Both types of studies are useful, depending on the application and the research goal.

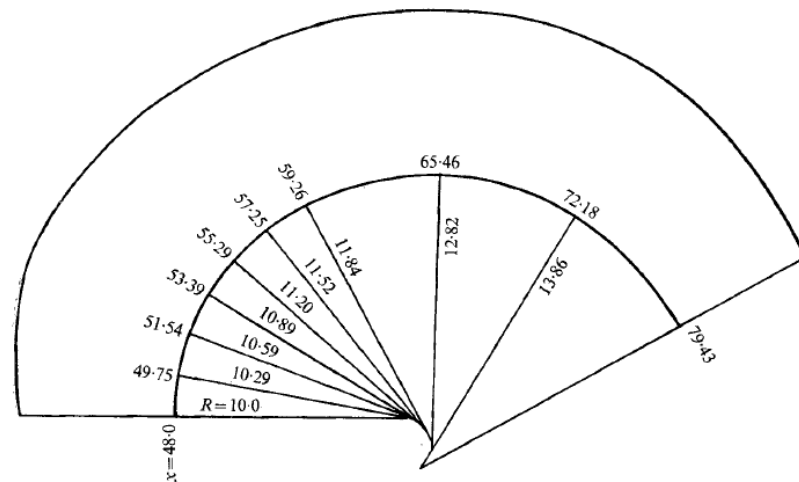


**Figure 7: Wind tunnel section setup for zero pressure gradient; the radius of curvature gradually increases so neither a favourable or adverse pressure gradient exists (So & Mellor, 1973).**

In terms of showing the similarities between streamwise pressure gradients and curvature effects, Holloway et al. (2005) completed a detailed experiment using a curved wind tunnel test section with different combinations of converging walls and curvature. Figure 8 shows the different configurations, where  $A_m$  and  $A_s$  denote cases where the pressure gradient is added to the second section of the wind tunnel via a converging section and  $R_m$  and  $R_s$  denote cases where the pressure gradient is removed from the second section. The subscripts m and s are a representation of the strength of the tunnel convergence. These different configurations allowed the researchers to control which sections would primarily exhibit curvature effects and which sections would primarily exhibit pressure gradient effects. This experiment confirmed the similarity between pressure gradients effects and curvature effects by investigating the magnitude of the streamwise strain rate and direction of the principal mean strain rate. They found that there were similarities between the magnitude of the streamwise strain rate induced by flow convergence (pressure gradient) and that produced by curvature. They also found that the direction of the principal mean strain rate was equivalent for the converging section (pressure

gradient effects) and the non-converging section (curvature effects), which again confirmed the similarity between the two effects. Furthermore, the original cross section of the tunnel was square, representing the full three dimensionality of a curved flow, which is a more accurate depiction of the curvature effects in practical applications as opposed to a high aspect ratio section.

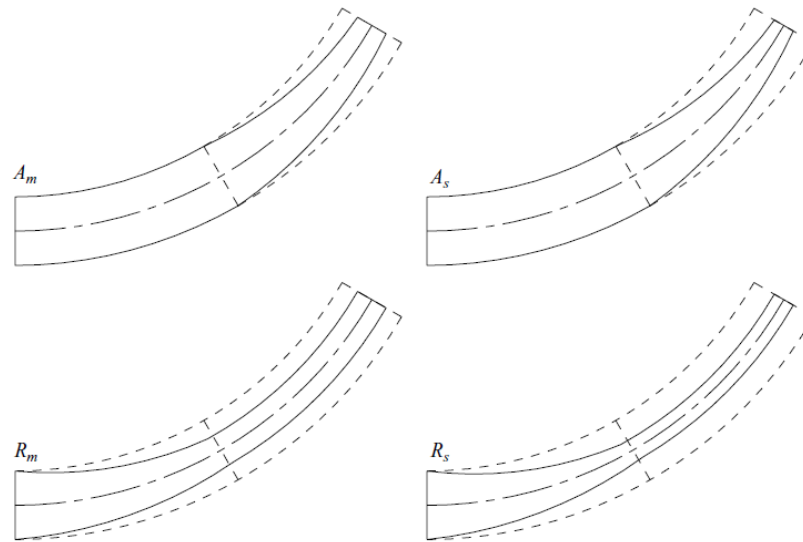


**Figure 8: Test configurations for the experiment conducted by Holloway et al. (2005).  $R_m$  and  $R_s$  represent cases where the pressure gradient is removed from the second section,  $A_m$  and  $A_s$  represent cases where the pressure gradient is applied to the second section**

Therefore, due to the similarity of curvature effects and streamwise pressure gradients, any research exclusively considering curvature effects should be done in zero or near zero pressure gradient scenarios to isolate the curvature effects from the streamwise pressure gradient effects. However, practical applications that include curvature effects will likely have additional streamwise pressure gradients. For example, consider the case of a centrifugal compressor, as studied in this work. In the impeller of a centrifugal compressor stage, there is a combination of curvature, rotation and a pressure gradient (pressure increase). Therefore, for this style of case, the effects of streamwise pressure gradients should not be completely isolated, since this would not be an accurate representation of the actual problem.

### 3.1.5 Summary

The preceding section outlined the main characteristics of curvature in terms of magnitude and directionality as well as the effects of Reynolds number and the effects of streamwise pressure gradients on curvature. In terms of magnitude, the presumed effects of curvature can be measured by the radius of curvature and boundary layer thickness for a global evaluation, or the Richardson number for an evaluation of local curvature effects. The directionality of the curvature greatly influences the curvature effects, with convex curvature causing stabilization of turbulence and concave curvature causing destabilization. *Re* effects on curvature are relatively unknown and should be further investigated. Studies have shown that streamwise pressure gradients can resemble curvature effects. The next section will go into detail on turbulence modelling techniques and the governing equations of various turbulence models.

### 3.2 Turbulence modelling – Theory and governing equations

Turbulent flows are incredibly complex, consisting of multiple length and time scales, unsteadiness, randomness and three-dimensionality (Pope, 2000, p. 335). For this reason, turbulent flows are impossible to resolve using analytical methods. As a result, numerical methods must be used, known as computational fluid dynamics (CFD). These methods discretize the flow domain into smaller cells, which are then resolved by solving the flow equations for each cell. Then by using averaging and approximation techniques over each of cells, scalar and vector fields are computed.

Various methods can be used to compute the flow field for a given problem. The three main categories of CFD, listed from the most to the least computationally intensive, are direct numerical simulation (DNS), large eddy simulation (LES) and Reynold-averaged Navier Stokes (RANS) methods. DNS is the most accurate, but also the most computationally intensive method because there is no turbulence modeling involved. Turbulent flows are resolved down to the smallest scales of turbulence (Kolmogorov scales). LES is somewhat of a mixture of DNS and RANS

because the large turbulent eddies in the flow are fully resolved, but the smaller turbulent scales are modeled. This still gives an accurate, detailed solution of the flow field and of the turbulent structures in the flow, without as much computational intensity as full DNS. RANS is the least computationally intensive method, but this also means that it is the least detailed and least exact method. With RANS, the Reynolds stresses are fully approximated by turbulence models.

From these descriptions it is clear that there is a trade-off between computational intensity and level of detail and accuracy, meaning that the best method to use depends on the task and the final goal. DNS and LES are generally used for research of the turbulent structures in the flow, whereas RANS methods are more practical for industrial applications because of their computational advantages. RANS methods have a much faster turn-around time than both LES and DNS methods, which make them ideal for design iteration and optimization. This, however, leads to a heavily approximated solution, with no resolution of turbulent structures; often completely acceptable for industrial applications, where mean quantities, such as velocity or pressure, are more important than fine details, such as turbulence at the Kolmogorov scales. The main focus of this thesis is on industrial applications, thus from this point forward only RANS methods will be discussed in detail.

Despite being computationally simpler than DNS or LES, computing the flow field using RANS is still not a simple task. Issues quickly arise because of the ratio of the number of equations to the number of unknown quantities, known as the closure problem. There are ten unknown quantities in any flow problem: the velocity (vector) distributions in the  $x$ ,  $y$  and  $z$  directions, the pressure (scalar) distribution and six individual Reynolds stresses. These unknowns must be resolved to fully compute a turbulent flow in any application. This becomes an issue since there are only four equations for the flow field: the momentum equations in the Cartesian directions and the continuity equation. This is where turbulence modelling is required to close the system of equations; turbulence models provide approximations for the six unknown Reynolds stresses based on different parameters, resulting in an equality of equations and unknowns. These

approximations will reduce the accuracy of the solution since only the mean flow is computed and the turbulent fluctuations are modeled, but as stated previously, this is a trade-off for computational speed.

When using RANS techniques, there are several turbulence models that can be used to approximate the Reynolds stresses and, in turn, to predict turbulent flows. Each of the models has advantages and disadvantages depending on the nature of flow being studied. For that reason, there are no set procedures as to which turbulence model to use for a specific flow. Some turbulence models are known to perform better than others, however these are only guidelines based on experience. In the following section, the theory and application of two standard types of turbulence models will be described: two-equation eddy viscosity models and Reynolds stress models. This is preceded by an explanation of the origin of the turbulent transport equations, which are essential for all turbulence models.

### 3.2.1 *Origin of the turbulent transport equations*

The modelling of turbulent flows using RANS methods begins with the continuity equation (incompressible) and the Navier-Stokes momentum equations for the mean flow, given by Eqs. 3.3 and 3.4 (White, 2011), respectively.

$$\frac{\partial U_i}{\partial x_i} = 0 \quad (3.3)$$

$$\rho \left( \frac{\partial U_i}{\partial t} + U_j \frac{\partial U_i}{\partial x_j} \right) = -\frac{\partial p}{\partial x_i} + \mu \frac{\partial^2 U_i}{\partial x_i^2} - \rho g_i \quad (3.4)$$

From this point, each of the variable quantities is then decomposed into a mean component and a fluctuating (turbulent) component, and the result is averaged, using a technique known as Reynolds averaging. Through a series of arithmetic operations, the resulting Reynolds-averaged Navier-Stokes momentum equations are obtained (Eq. 3.5) (Wilcox, 2006, p. 40). Recall that uppercase letters denote mean velocity and lowercase letters denote fluctuating velocity. The ensuing

continuity equation is the same as before, however in the momentum equations a new term is introduced, known as the Reynolds stress tensor ( $\rho\overline{u_i u_j}$ ).

$$\rho \left( \frac{\partial U_i}{\partial t} + U_j \frac{\partial U_i}{\partial x_j} \right) = - \frac{\partial p}{\partial x_i} + \frac{\partial}{\partial x_j} \left( \mu \left( \frac{\partial U_i}{\partial x_j} + \frac{\partial U_j}{\partial x_i} \right) - \rho\overline{u_i u_j} \right) \quad (3.5)$$

The Reynolds stress tensor has six components and therefore six unknowns have been introduced due to the Reynolds averaging completed on the Navier-Stokes equations. To resolve this issue, an equation needs to be derived to compute the Reynolds stresses.

The Reynolds stress equation is developed by manipulating the original Navier-Stokes equations and using the same averaging techniques as used to derive the RANS equations. The operations necessary to derive the Reynolds stress equation are multiplying the  $U_i$  component of the Navier-Stokes equation by the fluctuating  $u_j$  component, summing it with the  $U_j$  momentum equation, multiplied by the  $u_i$  component (see Eq. 3.6) (Wilcox, 2006, p. 41), and then averaging.

$$\overline{u_j N(U_i) + u_i N(U_j)} = 0 \quad (3.6)$$

Where:  $N(\dots)$  is the component of the Navier-Stokes equation,  $U$  is the mean velocity and  $u$  is the fluctuating component.

After algebraic manipulation and simplifications, the resulting Reynolds stress equation is (Wilcox, 2006, p. 43):

$$\begin{aligned} \frac{\partial \overline{u_i u_j}}{\partial t} + \frac{\partial}{\partial x_k} (U_k \rho \overline{u_i u_j}) \\ = -\rho \overline{u_i u_j} \frac{\partial U_j}{\partial x_k} - \rho \overline{u_j u_k} \frac{\partial U_i}{\partial x_k} + \epsilon_{ij} - \Phi_{ij} \\ + \frac{\partial}{\partial x_k} \left[ \nu \frac{\partial \overline{u_i u_j}}{\partial x_k} + C_{ijk} \right] \end{aligned} \quad (3.7)$$

Where:

$$\epsilon_{ij} = 2\nu \frac{\partial \overline{u_i}}{\partial x_k} \frac{\partial \overline{u_j}}{\partial x_k} \quad (3.8)$$

$$\Phi_{ij} = \frac{p'}{\rho} \left( \frac{\partial u_i}{\partial x_j} + \frac{\partial u_j}{\partial x_i} \right) \quad (3.9)$$

$$\rho C_{ijk} = \rho \overline{u_i u_j u_k} + \overline{p' u_i} \delta_{jk} + \overline{p' u_j} \delta_{ik} \quad (3.10)$$

Equation 3.7 is the basis for Reynolds stress models, where each of the individual Reynolds stresses is calculated based on the differential equation, which will be described in §3.2.3.

From Eq. 3.7, one further step can be taken to obtain the turbulent kinetic energy,  $k$ , equation, which is used for the eddy viscosity models described in §3.2.2. The turbulent kinetic energy is defined by half of the trace of the Reynolds stress tensor, that is (Wilcox, 2006, p. 108):

$$k = \frac{1}{2} \overline{u_i u_i} \quad (3.11)$$

With this in mind, one can take the trace of the Reynolds stress differential equation, presented as Eq. 3.7, to obtain the differential equation for  $k$  used in common turbulence models. After some algebra, the resulting  $k$  equation is (Wilcox, 2006, p. 108):

$$\begin{aligned} \frac{\partial k}{\partial t} + U_j \frac{\partial k}{\partial x_j} = & \overline{u_i u_j} \frac{\partial U_i}{\partial x_j} - \nu \frac{\partial u_i}{\partial x_k} \frac{\partial u_i}{\partial x_k} \\ & + \frac{\partial}{\partial x_j} \left( \nu \frac{\partial k}{\partial x_j} - \frac{1}{2} \overline{u_i u_i u_j} - \frac{1}{\rho} \overline{p' u_j} \right) \end{aligned} \quad (3.12)$$

From this point forward, all of the turbulence models described utilize the  $k$  equation, however approximations and assumptions are implemented to model the unknown terms. Terms that require modelling are those which contain any fluctuating components (i.e. the right hand side of the equation).

From the derivation of the Reynolds stress and  $k$  equations, the level of approximation and sources of error in turbulence modelling become very apparent.

At each level of manipulation and averaging, new unknowns are introduced, which must be modelled to close the system of equations and obtain a numerical solution. The level at which these approximations are made describes the different types of turbulence modelling techniques, which are outlined in the next sections.

### 3.2.2 Two-equation eddy viscosity models (EVM)

Two – equation eddy viscosity models are relatively simple and robust turbulence models, making them applicable for widespread use. They are particularly useful for industrial design purposes where fast turnaround time is required to iterate through different designs. Two equation models use two additional differential equations to calculate turbulence length and time scales, which are used to model the velocity fluctuations that come with turbulence. Modern two-equation models are based on the Boussinesq approximation (Eq. 3.13) (Boussinesq, 1877), which approximates the Reynolds stresses as proportional to the mean velocity gradients. Note that for incompressible flow,  $\partial U_k / \partial x_k = 0$ , from the continuity equation.

$$-\rho \overline{u_i u_j} = \mu_t \left( \frac{\partial U_i}{\partial x_j} + \frac{\partial U_j}{\partial x_i} \right) - \frac{2}{3} \mu_t \frac{\partial U_k}{\partial x_k} \delta_{ij} - \frac{2}{3} \rho k \delta_{ij} \quad (3.13)$$

Where:  $u$  is the fluctuating turbulent velocity,  $U$  is the mean velocity,  $k$  is the turbulent kinetic energy (TKE),  $\rho$  is the fluid density and  $\mu_t$  is the eddy viscosity.

The proportionality constant,  $\mu_t$ , is known as the eddy viscosity, which represents the momentum transfer by the turbulent eddies. In two equation models, the eddy viscosity is calculated from the solution of the two additional differential equations, one of which is often the turbulence kinetic energy (TKE),  $k$ . Differences between eddy viscosity models are primarily due to the other transport equation used and how the eddy viscosity term is defined.

There are many different variations of two equation eddy viscosity models and there are no rules that dictate which turbulence model to use for a specific application. However, through extensive experimentation and testing, there are some guidelines as to which models will perform well in certain flow conditions and



which will not. Three prominent eddy viscosity models available in most commercial CFD packages are the  $k - \epsilon$ ,  $k - \omega$  and SST models, each of which will be outlined in the following section. Finally, a newly developed variation of the SST model with curvature correction, denoted SST-CC, will be presented.

### 3.2.2.1 The $k - \epsilon$ model

The  $k - \epsilon$  model is one of the most commonly used models and is useful for a wide range of turbulent flow problems. The eddy viscosity,  $\mu_t$ , in the  $k - \epsilon$  model is obtained from the turbulent kinetic energy,  $k$ , and the turbulent dissipation rate (dissipation of velocity fluctuations),  $\epsilon$  (Eq. 3.14).  $k$  and  $\epsilon$  are obtained by solving transport equations, which are given by Eqs. 3.15 and 3.16, respectively (Launder & Spalding, 1974). The turbulence production term,  $P_k$ , used in the both transport equations is given in Eq. 3.17.

$$\mu_t = C_\mu \rho \frac{k^2}{\epsilon} \quad (3.14)$$

$$\frac{\partial(\rho k)}{\partial t} + \frac{\partial}{\partial x_j}(\rho U_j k) = \frac{\partial}{\partial x_j} \left( \left( \mu + \frac{\mu_t}{\sigma_k} \right) \frac{\partial k}{\partial x_j} \right) + P_k - \rho \epsilon \quad (3.15)$$

$$\begin{aligned} \frac{\partial(\rho \epsilon)}{\partial t} + \frac{\partial}{\partial x_j}(\rho U_j \epsilon) \\ = \frac{\partial}{\partial x_j} \left( \left( \mu + \frac{\mu_t}{\sigma_\epsilon} \right) \frac{\partial \epsilon}{\partial x_j} \right) + \frac{\epsilon}{k} (C_{\epsilon 1} P_k - C_{\epsilon 2} \rho \epsilon) \end{aligned} \quad (3.16)$$

$$P_k = \mu_t \left( \frac{\partial U_i}{\partial x_j} + \frac{\partial U_j}{\partial x_i} \right) \frac{\partial U_i}{\partial x_j} - \frac{2}{3} \frac{\partial U_k}{\partial x_k} \left( 3\mu_t \frac{\partial U_k}{\partial x_k} + \rho k \right) \quad (3.17)$$

In these equations, the following constants derived by Launder and Spalding (1974) are used:

$$C_\mu = 0.09, C_{\epsilon 1} = 1.44, C_{\epsilon 2} = 1.92, \sigma_k = 1.0, \sigma_\epsilon = 1.3$$

### 3.2.2.2 The $k - \omega$ model

The  $k - \omega$  model is another commonly used two-equation turbulence model that was developed by Wilcox (1988). It solves transport equations for the turbulence kinetic energy,  $k$ , and the specific dissipation rate,  $\omega$ , to model the eddy viscosity term, as shown in Eq. 3.18. The specific dissipation rate,  $\omega$ , is defined by the ratio  $\epsilon/k$  (Wilcox, 2006, p. 122). The  $k$  and  $\omega$  transport equations are given by Eqs. 3.19 and 3.20, respectively.

$$\mu_t = \rho \frac{k}{\omega} \quad (3.18)$$

$$\frac{\partial(\rho k)}{\partial t} + \frac{\partial}{\partial x_j}(\rho U_j k) = \frac{\partial}{\partial x_j} \left( \left( \mu + \frac{\mu_t}{\sigma_k} \right) \frac{\partial k}{\partial x_j} \right) + P_k - \beta' \rho k \omega \quad (3.19)$$

$$\begin{aligned} \frac{\partial(\rho \omega)}{\partial t} + \frac{\partial}{\partial x_j}(\rho U_j \omega) \\ = \frac{\partial}{\partial x_j} \left( \left( \mu + \frac{\mu_t}{\sigma_\omega} \right) \frac{\partial \omega}{\partial x_j} \right) + \alpha \frac{\omega}{k} P_k - \beta \rho \omega^2 \end{aligned} \quad (3.20)$$

The constants in these model equations are (Wilcox, 1988):

$$\beta' = 0.09, \alpha = \frac{5}{9}, \beta = 0.075, \sigma_k = 2, \sigma_\omega = 2$$

### 3.2.2.3 The SST model

The SST model is a combination of the  $k - \epsilon$  and the  $k - \omega$  models. It takes advantage of the performance of each of these models in different regions; the  $k - \epsilon$  model performs well in freestream regions, whereas the  $k - \omega$  model performs well in near-wall regions (Menter, 1994). Therefore, the eddy viscosity formulation for the SST model must also incorporate this combination. As shown in Eq. 3.21, the eddy viscosity term uses a function  $F_2$  (Eq. 3.22) that is equal to 1 in the boundary layer region and equal to zero outside the boundary layer to incorporate the switch between the two models.  $F_2$  is dependent on the distance from the nearest surface,

$y$ , as well as different flow properties and flow characteristics, as shown in Eqs. 3.22 and 3.23.

$$\mu_t = \frac{\rho a_1 k}{\max\left(a_1 \omega, \frac{\partial u}{\partial y} F_2\right)} \quad (3.21)$$

$$F_2 = \tanh(\text{arg}_2^2) \quad (3.22)$$

$$\text{arg}_2 = \max\left(\frac{2\sqrt{k}}{\beta' \omega y}, \frac{500\nu}{y^2 \omega}\right) \quad (3.23)$$

In order to combine the two models, the  $k - \epsilon$  model must first be transformed to a  $k$  and  $\omega$  formulation. The two models are then combined as a linear combination using blending functions which automatically assign the  $k - \omega$  model equations to the near wall regions and the  $k - \epsilon$  model equations to the freestream regions. The transformed equations are shown as Eqs. 3.24 and 3.25, respectively (Menter, 1994).

$$\frac{\partial(\rho k)}{\partial t} + \frac{\partial}{\partial x_j}(\rho U_j k) = \frac{\partial}{\partial x_j} \left( \left( \mu + \frac{\mu_t}{\sigma_{k2}} \right) \frac{\partial k}{\partial x_j} \right) + P_k - \beta' \rho k \omega \quad (3.24)$$

$$\begin{aligned} \frac{\partial(\rho \omega)}{\partial t} + \frac{\partial}{\partial x_j}(\rho U_j \omega) \\ = \frac{\partial}{\partial x_j} \left( \left( \mu + \frac{\mu_t}{\sigma_{\omega 2}} \right) \frac{\partial \omega}{\partial x_j} \right) + 2\rho \frac{1}{\sigma_{\omega 2} \omega} \frac{\partial k}{\partial x_j} \frac{\partial \omega}{\partial x_j} \\ + \alpha_2 \frac{\omega}{k} P_k - \beta_2 \rho \omega^2 \end{aligned} \quad (3.25)$$

Where all the new constants are as follows (Menter, 1994):

$$\sigma_{k2} = 1.0, \sigma_{\omega 2} = 0.856, \alpha_2 = 0.44, \beta_2 = 0.0828$$

With the transformation to the  $k - \epsilon$  equations, the blending functions can be applied by multiplying the  $k - \omega$  equations by the blending function  $F_1$  and the transformed  $k - \epsilon$  equations by  $(1 - F_1)$  and adding them in a linear combination as

shown in Eqs. 3.26 and 3.27. The definition of the blending function  $F_1$  (Eqs. 3.28 - 3.30) in the SST model has been improved from the baseline (BSL)  $k - \omega$  model by incorporating flow variables as opposed to only being a function of wall distance.

$$k_{SST} = F_1 k_{k-\omega} + (1 - F_1) k_{k-\epsilon} \quad (3.26)$$

$$\omega_{SST} = F_1 \omega_{k-\omega} + (1 - F_1) \omega_{k-\epsilon} \quad (3.27)$$

$$F_1 = \tanh(\text{arg}_1^4) \quad (3.28)$$

$$\text{arg}_1 = \min \left( \max \left( \frac{\sqrt{k}}{\beta' \omega y}, \frac{500\nu}{y^2 \omega} \right), \frac{4\rho k}{CD_{k\omega} \sigma_{\omega 2} y^2} \right) \quad (3.29)$$

$$CD_{k\omega} = \max \left( 2\rho \frac{1}{\sigma_{\omega 2} \omega} \frac{\partial k}{\partial x_j} \frac{\partial \omega}{\partial x_j}, 1.0 \times 10^{-10} \right) \quad (3.30)$$

#### 3.2.2.4 The SST – CC model

The curvature corrected SST model (SST-CC) was developed by Smirnov and Menter (2009) as a modification to the SST model based on the original correction by Spalart and Shur (1997) to the Spalart-Allmaras (S-A) one equation model. The correction is applied to the two additional transport equations for the SST model ( $k$  and  $\omega$ ) as a multiplier to the production term,  $P_k$ , shown in Eqs. 3.31 and 3.32, respectively (Smirnov & Menter, 2009).

$$\begin{aligned} \frac{\partial(\rho k)}{\partial t} + \frac{\partial}{\partial x_j} (\rho U_j k) \\ = \frac{\partial}{\partial x_j} \left( \left( \mu + \frac{\mu_t}{\sigma_{k2}} \right) \frac{\partial k}{\partial x_j} \right) + P_k f_{r1} - \beta' \rho k \omega \end{aligned} \quad (3.31)$$

$$\begin{aligned}
& \frac{\partial(\rho\omega)}{\partial t} + \frac{\partial}{\partial x_j}(\rho U_j \omega) \\
&= \frac{\partial}{\partial x_j} \left( \left( \mu + \frac{\mu_t}{\sigma_{\omega 2}} \right) \frac{\partial \omega}{\partial x_j} \right) + 2\rho \frac{1}{\sigma_{\omega 2} \omega} \frac{\partial k}{\partial x_j} \frac{\partial \omega}{\partial x_j} \\
&+ \alpha_2 \frac{\omega}{k} P_k f_{r1} - \beta_2 \rho \omega^2
\end{aligned} \tag{3.32}$$

The production multiplier is denoted by  $f_{r1}$  (Eq. 3.33) and its magnitude varies depending on the flow curvature. For areas with convex curvature, turbulence production is diminished (or eliminated), meaning that the production multiplier  $f_{r1}$  will have a value that is less than unity. On the other hand, for areas with concave curvature, turbulence production is augmented, meaning that the multiplier will take on a value that is greater than one. Note that this multiplier has a limit of 1.25 (see Eq. 3.33) for numerical stability reasons, and to eliminate the possibility of excess turbulence production in very highly curved regions (Smirnov & Menter, 2009). The magnitude of the production multiplier is primarily based on the strain rate tensor,  $S_{ij}$ , the rotation rate tensor,  $\Omega_{ij}$ , and the overall rate of rotation of the system,  $\Omega^{rot}$ , as shown in Eqs. 3.34 - 3.41.

$$f_{r1} = \max(\min(f_{rotation}, 1.25), 0.0) \tag{3.33}$$

$$f_{rotation} = (1 + c_{r1}) \frac{2r^*}{1 + r^*} (1 - c_{r3} \tan^{-1}(c_{r2} \tilde{r})) - c_{r1} \tag{3.34}$$

$$r^* = \frac{S}{\Omega} \tag{3.35}$$

$$S = \sqrt{2S_{ij}S_{ij}} \tag{3.36}$$

$$\Omega = \sqrt{2\Omega_{ij}\Omega_{ij}} \tag{3.37}$$

$$S_{ij} = \frac{1}{2} \left( \frac{\partial U_i}{\partial x_j} + \frac{\partial U_j}{\partial x_i} \right) \quad (3.38)$$

$$\Omega_{ij} = \frac{1}{2} \left( \frac{\partial U_i}{\partial x_j} - \frac{\partial U_j}{\partial x_i} \right) + 2\epsilon_{mji}\Omega_m^{rot} \quad (3.39)$$

$$\tilde{r} = 2\Omega_{ik}S_{jk} \left[ \frac{DS_{ij}}{Dt} + (\epsilon_{imn}S_{jn} + \epsilon_{jmn}S_{in})\Omega_m^{rot} \right] \frac{1}{\Omega D^3} \quad (3.40)$$

$$D^2 = \max(S^2, 0.09\omega^2) \quad (3.41)$$

With the constants in Eq. 3.34 being (Smirnov & Menter, 2009):

$$c_{r1} = 1.0, c_{r2} = 2.0, c_{r3} = 1.0$$

The SST-CC model has been tested by Smirnov and Menter (2009), using multiple test cases. Some examples of these test cases are developed flow in a rotating channel, flow through a two-dimensional U-duct, flow through a hydro cyclone and flow through a centrifugal compressor using the "Radiver" (Ziegler, Gallus, & Niehuis, 2003) test case. These cases show improved agreement to experimental results and/or DNS by the SST-CC model in mean velocity profiles, with some cases comparing other variables such as  $C_p$ ,  $C_f$ , turbulent fluctuations and shear stress as compared to the original SST model. None of the documented cases show extensive detail on turbulence related quantities, such as TKE or Reynolds stresses, or provide any focus on the underlying mechanisms relating to curvature. This includes the Radiver compressor test case, where the comparison was limited to a four operating points on a speedline.

### 3.2.3 Reynolds stress models (RSM)

Reynolds stress models (RSM) are the most complex and computational intensive models in the RANS category. The complexity stems from having to solve six additional transport equations for the Reynolds stress components, as opposed to solving two transport equations as in the two equation models described earlier.

There are many different versions of RSMs, however this description will focus on the RSM-SSG model specifically, formulated by Speziale, Sarkar and Gatski (1991). For this model, the transport equation for the Reynolds stresses (in index notation) is given by the following equation.

$$\begin{aligned} \frac{\partial \overline{u_i u_j}}{\partial t} + \frac{\partial}{\partial x_k} (U_k \rho \overline{u_i u_j}) - \frac{\partial}{\partial x_k} \left( \left( \mu + \frac{2}{3} C_s \rho \frac{k^2}{\epsilon} \right) \frac{\partial \overline{u_i u_j}}{\partial x_k} \right) \\ = P_{ij} + \Phi_{ij} - \frac{2}{3} \delta_{ij} \rho \epsilon \end{aligned} \quad (3.42)$$

Where:  $P_{ij}$  is the production term (Eq. 3.43),  $\Phi_{ij}$  is the pressure-strain correlation term (Eqs. 3.44 - 3.46),  $k$  is the turbulent kinetic energy,  $C_s$  is a constant (equal to 0.22) and  $\epsilon$  is the turbulent dissipation.

$$P_{ij} = -\rho \overline{u_i u_j} \frac{\partial U_j}{\partial x_k} - \rho \overline{u_j u_k} \frac{\partial U_i}{\partial x_k} \quad (3.43)$$

The differences between the various Reynolds stress models arise primarily in how the pressure-strain correlation term is modelled. The RSM-SSG model uses a quadratic relation for this term, shown by the definitions in Eqs. 3.44, 3.45 and 3.46 (Speziale, Sarkar, & Gatski, 1991).

$$\Phi_{ij} = \Phi_{ij,1} + \Phi_{ij,2} \quad (3.44)$$

$$\Phi_{ij,1} = -\rho \epsilon \left[ C_{s1} a_{ij} + C_{s2} \left( a_{ik} a_{kj} - \frac{1}{3} a_{mn} a_{mn} \delta_{ij} \right) \right] \quad (3.45)$$

$$\begin{aligned} \Phi_{ij,2} = & -C_{r1} P a_{ij} + C_{r2} \rho k S_{ij} - C_{r3} \rho k S_{ij} \sqrt{a_{mn} a_{mn}} \\ & + C_{r4} \left( a_{ik} S_{jk} + a_{jk} S_{ik} - \frac{2}{3} a_{kl} S_{kl} \delta_{ij} \right) \\ & + C_{r5} \rho k (a_{ik} \Omega_{jk} + a_{jk} \Omega_{ik}) \end{aligned} \quad (3.46)$$

$$a_{ij} = \frac{\overline{u_i u_j}}{k} - \frac{2}{3} \delta_{ij} \quad (3.47)$$

$$S_{ij} = \frac{1}{2} \left( \frac{\partial U_i}{\partial x_j} + \frac{\partial U_j}{\partial x_i} \right) \quad (3.48)$$

$$\Omega_{ij} = \frac{1}{2} \left( \frac{\partial U_i}{\partial x_j} - \frac{\partial U_j}{\partial x_i} \right) \quad (3.49)$$

The constants in the pressure-strain correlation terms for the RSM-SSG model are as follows (Speziale, Sarkar, & Gatski, 1991):

**Table 4: Constants for the pressure-strain correlation term in the RSM-SSG turbulence model**

Constant	Value
$C_{s1}$	1.7
$C_{s2}$	-1.05
$C_{r1}$	0.9
$C_{r2}$	0.8
$C_{r3}$	0.65
$C_{r4}$	0.625
$C_{r5}$	0.2

Along with the individual differential equations for the Reynolds stresses, an additional transport equation for the dissipation rate,  $\epsilon$ , must also be solved since it appears in the stress transport equations. Eq. 3.50 presents the  $\epsilon$  equation for the RSM-SSG model (Speziale, Sarkar, & Gatski, 1991).

$$\begin{aligned} \frac{\partial(\rho\epsilon)}{\partial t} + \frac{\partial}{\partial x_k}(\rho U_k \epsilon) &= \frac{\epsilon}{k} (C_{\epsilon 1} P_k - C_{\epsilon 2} \rho \epsilon) \\ &+ \frac{\partial}{\partial x_k} \left( \left( \mu + \frac{\mu_t}{\sigma_{\epsilon RS}} \right) \frac{\partial \epsilon}{\partial x_k} \right) \end{aligned} \quad (3.50)$$



Where the constants associated with the  $\epsilon$  equation are as follows (Speziale, Sarkar, & Gatski, 1991):

$$C_{\epsilon 1} = 1.45, C_{\epsilon 2} = 1.83, \sigma_{\epsilon RS} = 1.36$$

### 3.2.4 *Turbulence models studied in current work*

From this point forward, three of the previous described turbulence models are used in this thesis. These models are the SST, the SST-CC and the RSM-SSG models. The SST-CC model is the primary focus in this thesis and the reasoning behind choosing this particular model is discussed in the next chapter. The choices of the SST and RSM-SSG models are based on a previous performance evaluation by Bourgeois (2008) and Roberts and Steed (2004) demonstrating the capabilities of these models for turbomachinery applications, which will be described in more detail in §3.4.

Therefore, the models described that will not be studied further are the  $k - \epsilon$  model and the  $k - \omega$  model. The  $k - \epsilon$  model will not be investigated further because of its well-known poor performance in compressible wall-bounded flows with adverse pressure gradients (Menter, 1994) as are found in compressor flows. Conversely, the  $k - \omega$  model has shown improvements over the  $k - \epsilon$  model in areas such as flow separation prediction and would potentially be suitable for the type of flows in this study (Menter, 1994), however, since the SST model is essentially an optimized  $k - \omega$  model, the  $k - \omega$  model is also excluded from the analysis.

### 3.2.5 *Summary*

This section outlined the concept of turbulence modelling, and presented the formulations for several common two-equation turbulence models for industrial applications (the  $k - \epsilon$  model, the  $k - \omega$  model, the SST model and the SST-CC model) and one Reynolds stress model (the RSM-SSG model). Finally, a brief outline on the different models being studied was presented; these models are the SST, SST-CC and RSM-SSG models. In the next section, the models described will be evaluated in terms of their abilities to predict flows with high surface curvature, based on

previous numerical work. Corrections to different eddy viscosity models will be discussed, as well as the reasoning behind choosing the SST-CC model over other curvature corrected models.

### ***3.3 Turbulence modelling with respect to curvature***

An important decision when numerically modelling any flow is choosing an appropriate turbulence model. In the previous sections, various eddy viscosity models (EVM) and a Reynolds stress model (RSM) were described in terms of governing equations, however it is important to understand the main advantages and disadvantages of these models, with respect to curvature prediction.

It is fairly well known that many eddy viscosity models do not perform well under the influence of curvature or system rotation because they assume that turbulence is fully isotropic (Pope, 2000, p. 364). The effects of curvature on turbulence and flow structure has been extensively studied using various simplified configurations such as 90 degree ducts, 180 degree U-turn ducts or rotating ducts to evaluate the predictive performance of different eddy viscosity models, as well as make an attempt to improve their performance so that they may be used for more complex design purposes. Eddy viscosity models are extremely attractive for design purposes since they are associated with fast turnaround times, however they still not ideal for certain types of flows, i.e. flows with high curvature. Reynolds stress models on the other hand have been designed with a built-in sensitivity to curvature.

Reynolds stress models fully account for the turbulence anisotropy by solving additional transport equations, which makes them naturally more sensitive to complex turbulent flows with curvature than eddy viscosity models (Bernard & Wallace, 2002), however strong curvature effects can still be a problem (Wallin & Johansson, 2002). Nevertheless, the performance comes at a cost; RSMs are very complex and computationally expensive as compared to EVMs. The performance of RSMs can be approached with less computational cost by using algebraic Reynolds stress models (ARSMs), which are models that solve algebraic equations for the

Reynolds stresses as opposed to differential equations (Girimaji, 1997). These methods could be further investigated if they can provide high accuracy similar to RSMs, however they are not discussed in this work.

Many numerical studies have been completed on flows with curvature over the past 30 years. The completed numerical studies have been carried out to investigate the abilities of the most common turbulence models available today ( $k - \epsilon$ ,  $k - \omega$ , SST, RSM) to predict flows with curvature, but more recently the numerical studies tend to focus on developing improved eddy viscosity turbulence models that have been altered with “curvature corrections” to be able to properly predict flows over curved surfaces. The  $k - \omega$ ,  $k - \epsilon$  and SST turbulence models have been corrected in different ways and have shown improvements that are competitive with more curvature sensitive models such as Reynolds stress models, while still maintaining the simplicity of eddy viscosity models. The following sections describe two types of studies: those that evaluate readily available eddy viscosity turbulence models, and those that alter existing eddy viscosity models to account for curvature effects.

### *3.3.1 Evaluation of EVMs with respect to predicting curvature effects*

A common way of evaluating the performance of turbulence models in predicting the flow over curved surfaces (both convex and concave) is by investigating the flow through curved ducts. In this category, there is a fairly wide variety of studies performed. One common type of study makes use of a high aspect ratio rectangular duct in an attempt to eliminate the third spatial direction and the emergence of complex secondary flows (i.e. Kim & Patel, 1994). Another type of study examines the flow through a square duct, which incorporates a fully three dimensional flow and includes the effects of secondary flows, but also complicates the problem (i.e. Raisee et al., 2006). Regardless of the geometry, many different turbulence models have been tested numerically using these methods, so there is a broad range of detail on the performance of these turbulence models to predict curvature. In this section, previous numerical work related to testing turbulence models on their ability to predict flows with curvature is considered.

Sotiropoulos and Ventikos (1998) investigated the abilities of the standard  $k - \epsilon$  and  $k - \omega$  models, as well as non-linear variants of the  $k - \omega$  model in predicting the flow through a curved  $90^\circ$  rectangular section. Their study showed that the  $k - \omega$  model performed better in terms of predicting velocity profiles and vorticity fields closer to experimental data than the  $k - \epsilon$  model, however both linear models failed in capturing the vorticity characteristics associated with secondary flows that were captured by the non-linear variants of the  $k - \omega$  model. Therefore, their results showed that non-linear models could be investigated further for more complex curved flows. This was also confirmed in a study by Xu et al. (2008) that showed a non-linear eddy viscosity model (NLEVM) predicting similar mean velocity, TKE and Reynolds shear stress as compared to a Reynolds stress model in a U duct flow and a study by Raisee et al. (2006) that showed that a  $k - \epsilon$  NLEVM predicted the turbulence field better than two other low-Re linear  $k - \epsilon$  models for a rectangular sectioned curved duct. Raisee et. al also investigated a square cross section duct and concluded that both the low-Re linear  $k - \epsilon$  models and the  $k - \epsilon$  NLEVM were able to capture the flow fields well. There are many other studies similar to those mentioned above that evaluate the ability of different EVMs in predicting and accounting for the effects of curvature, such as those by Etemad et al. (2006) and Tsujita et al. (2003). These studies are useful as they provide information towards which models to avoid for applications with flow curvature, however they do not provide any insight on improvements that can be made to the models to include the effects of curvature.

### 3.3.2 *Curvature corrections for EVMs*

Along with evaluations of the sensitivity of current linear and non-linear eddy viscosity models in regards to curvature effects, studies that discuss curvature improvements to current eddy viscosity models are perhaps more useful to the development of turbulence modelling techniques. One early turbulence model alteration towards improving curvature prediction was that by Spalart and Shur (1997), with their correction to the Spalart-Allmaras one-equation model (Spalart & Allmaras, 1994). This correction is based on multiplying the production term in the

turbulence transport equation by a curvature correction function, and is adaptable to any other eddy-viscosity based model. Smirnov and Menter (2009) made use of this adaptability by applying it to the SST model, to form the SST-CC model, which will be discussed in the next section.

Since the Spalart and Shur (1997) correction, many other researchers have made alterations or additions to different eddy viscosity models to try to improve their performance with respect to curvature. For example, Kozulovic and Rober (2006) proposed an alteration to the  $k - \omega$  model that makes use of a curvature correction term in the  $\omega$  differential equation that is easy to implement and only uses local variables to compute constants. This model showed improvements in the prediction of Reynolds shear stress, a quantity known to be affected by curvature, in a curved section test case and a U duct test. It also performed well in a compressor stage, showing improved agreement with experiments towards the stall side of the speedline. York et al. (2009) investigated an alteration to the  $k - \epsilon$  model that uses a new formula to define a variable  $C_\mu$  (used in computing the eddy viscosity), in an attempt to improve the curvature sensitivity of the standard  $k - \epsilon$  model. This model showed sensitivity to rotation and curvature effects in various test cases as compared to the standard  $k - \epsilon$ , which often showed no reaction to curvature for quantities such as mean velocity or TKE profiles. The corrected  $k - \epsilon$  also showed improved agreement to experimental or DNS data in their test cases. Dhakal and Walters (2009) used the same methodology as York et al. (2009), but applied the correction to the SST model. They found promising results in prediction improvements in terms of TKE and velocity profiles over the standard SST model for a rotating channel flow case and a U duct test case. A good summary of other methods used to correct turbulence models to account for curvature and rotation effects can be found in a recent review paper by Durbin (2011).

Modifications as discussed above are interesting to turbulence modelling development since a basic eddy viscosity model that could accurately predict complex flows with curvature in a robust manner would be an extremely valuable asset, especially for industrial applications. Many of these models should be tested

thoroughly on more complex flows (not test cases like U ducts) to evaluate their abilities to accurately predict curvature effects for practical industrial flows.

### 3.3.3 Selection of the SST-CC model

It is obvious from the two previous sections that many efforts have been made to both test eddy viscosity models with respect to curvature as well as to alter them to make them more sensitive to curvature. This work focuses on the latter, since as discussed in previous sections, standard uncorrected EVMs are in need of improvement for cases with curvature.

Many “curvature corrected” models have been developed by previous researchers in terms of  $k - \epsilon$  and  $k - \omega$  corrections, however, this work investigates the correction to the SST model by Smirnov and Menter (2009) for the following reasons. The SST-CC model developed by Smirnov and Menter uses the basic formulation of the SST model, which has shown improvements over  $k - \omega$  and  $k - \epsilon$  models for cases similar to those studied in this work, and improves it further by accounting for curvature. It has been tested using standard test cases such as developing flow in a curved channel, two dimensional U duct flow and rotating channel flow and has been shown to match well with RSM results as well as experimental data in these cases. Moreover, the correction makes use of the Spalart and Shur correction (Spalart & Shur, 1997), which is robust and does not increase the computational time of the model. Furthermore, in previous work, the SST model was proven to match well with experimental data in terms of speedlines and flow field prediction for the types of centrifugal compressors studied in this work (Bourgeois et al., 2011). The SST-CC model is also directly implemented into the commercial solver ANSYS CFX 13.0, making it accessible to any future users.

The use of the SST-CC model in more complex three dimensional geometries has yet to be thoroughly described. Smirnov and Menter (2009) only briefly discussed a centrifugal compressor stage and compare a small number of points on a performance curve, however they did not provide extensive detail on how the SST-CC model account for curvature effects in terms of flow field predictions, efficiency

predictions, or how the model compares to a more curvature sensitive model, such as a RSM. Therefore, the present work will differ from previous work by analyzing the performance of the model in detail as well as by developing a further understanding of the mechanisms behind the model and how the model handles the effects of curvature.

The analysis of the SST-CC model will be carried out using three different cases. The first and second cases are centrifugal compressor stages designed by P&WC for their aero-engines. The first case is a split impeller compressor (307C) that has been studied previously both numerically and experimentally by Bourgeois et al. (2011). The second case is a newly developed compressor (1C) that contains a higher curvature than previous P&WC designs, thus making it a good test case for a curvature corrected model. The third case is a simplified version of a centrifugal compressor impeller. This case allows the curvature effects to be isolated from the other complex flow mechanisms in the centrifugal compressor impeller, while still maintaining a similar geometry. Furthermore, this case makes it simpler to identify if the SST-CC model is predicting the same differences in the same locations in the simplified geometry and compressor cases.

#### 3.3.4 Summary

The preceding section described the performance of different types of turbulence models (EVMs and RSMs) with respect to predicting curvature effects. Various EVMs have been investigated in terms of their sensitivity to curvature, however the underlying assumptions in EVMs make them naturally insensitive to curvature, making curvature-corrected models more useful. Alterations to EVMs to account for curvature effects have been tested with common EVMs ( $k - \epsilon$ ,  $k - \omega$  and SST) and many have shown improved curvature sensitivity in flow field or TKE prediction, however this work considers the SST-CC model of Smirnov and Menter (2009). This model was chosen because of its proven sensitivity to curvature improvements over the SST model in simplified cases, its robustness, the proven performance of the uncorrected SST model in previous cases similar to those studied here, and finally

the availability of the model for future researchers. The next section investigates the performance of different turbulence models in turbomachinery applications.

### ***3.4 Turbulence modelling in turbomachinery applications***

In industrial applications, CFD is an important tool to aid in the design and validation of turbomachinery components. However as with any CFD simulation, there are many sources of error that can lead to incorrect or unrealistic solutions. Some sources of error specific to turbomachinery relate to modelling approximations such as the use of idealized geometry in tip clearance regions, incorrect transition modelling, the use of mixing planes, and perhaps the largest approximation: the assumption of steady state flow (Denton, 2010). Due to the limitations of current CFD techniques, many of these assumptions are unavoidable; however one source of error that can be reduced is in turbulence modeling. Efforts are constantly being made to examine and improve readily available eddy viscosity turbulence models. Many researchers have investigated the use of different RANS based eddy viscosity models to predict turbomachinery performance. Some models are more suitable than others for these types of simulations. When simulating turbomachinery, models need to be able to cope with high Reynolds number flows as well as complex flow dynamics such as separated flows, tip clearance vortices, rotating to stationary reference frames, and flow effects by curved surfaces. Some researchers have investigated uncorrected turbulence model performance in turbomachinery applications and others have investigated curvature corrected models such as the curvature/rotation corrected Spalart-Allmaras model (SARC) (Spalart & Shur, 1997).

In terms of uncorrected models, Roberts and Steed (2004) tested the performance of the  $k - \epsilon$  and SST models in predicting the bulk parameters such as pressure ratio (PR), temperature ratio (TR) and total-to-static efficiency,  $\eta_{ts}$ , of a centrifugal compressor stage with a PR between 2 and 3. That study showed that the SST model was greatly superior to the  $k - \epsilon$  model in predicting these parameters, as compared to experimental data. Recently, Bourgeois et al. (2011) also showed that



the  $k - \epsilon$  model performed poorly when compared to experiments in a centrifugal compressor stage. From these studies one could conclude that SST model is the preferred model over the  $k - \omega$  or  $k - \epsilon$  model for these types of applications. The  $k - \omega$  model has shown improvements over the  $k - \epsilon$  model in near wall regions, as well as in adverse pressure gradients and in predicting compressible flows, however it performs poorly in the freestream (Menter, 1994). The  $k - \epsilon$  model, on the other hand, exhibits the opposite performance, being more suitable to freestream flows and not being able to predict adverse pressure gradients and compressible flows as accurately as the  $k - \omega$  model (Menter, 1994). Based on the advantages of the  $k - \omega$  model in the near-wall region and the improved performance of the  $k - \epsilon$  model in the freestream, it is clear why the SST model, which incorporates the benefits of both the  $k - \omega$  and  $k - \epsilon$  models, is suitable for a compressible, wall-bounded turbomachinery application with adverse pressure gradients. However, regardless of their apparent suitability, there is room for improvement with eddy viscosity models.

Other researchers have investigated the performance of different curvature corrected models in turbomachinery applications, as compared to other common models. Marconini et al. (2008) investigated the  $k - \omega$  model, the SARC model and the Baldwin-Lomax (B-L) algebraic model in terms of their performance towards predicting the flow phenomena near the shroud and in the tip clearance gap in a 3.9:1 pressure ratio centrifugal compressor. The primary objective of their work was to investigate different tip clearance modelling methods, however they also analyzed differences in the compressor flow field. The main findings were that the  $k - \omega$  and SARC models predict similarly to the B-L model, which is used in aerodynamic and turbomachinery applications (Baldwin & Lomax, 1978), however differences were found in regions of maximum curvature, such as near the hub and the shroud. In the hub and midspan regions, the  $k - \omega$  and SARC models matched experimental data better than the B-L model, however the opposite is true in the near shroud region. Dufour et al. (2008) analyzed the Radiver test case compressor (Ziegler et al., 2003) using two different eddy viscosity models with curvature

corrections. They tested the SARC model as well as another correction applied to a  $k - \epsilon$  based model: the Yang and Shih rotation and curvature corrected model (YSRC). From analyzing the eddy viscosity at different planes in the compressor impeller, it was found that both of the curvature corrected models were consistent with the physics of curvature, each appropriately modelling the stabilization and destabilization of turbulence. Finally, Smirnov and Menter (2009) recently studied the SST-CC model using the same Radiver test case. They investigated the performance of the model in predicting the pressure rise across the compressor for four different operating points. Their results showed that the SST-CC model matched experimental data better than the uncorrected SST model, for three out of the four points. Both models performed poorly in the choke region for this particular compressor. This study only briefly investigated the performance of the models in regards to turbomachinery, leaving questions about the mean flow field and turbulence quantities.

Both the studies testing the standard turbulence models as well as those investigating various curvature corrected models are useful for the development of turbulence modelling in turbomachinery. By evaluating the performance of standard turbulence models used in industry (such as the  $k - \epsilon$ ,  $k - \omega$  and SST models), the focus can be directed towards improving models that already perform well in these types of applications, and the models with poor performance can be disregarded. The studies that test different curvature corrected models have shown that these models are feasible for use in turbomachinery, and thus, advancements can be made with these models. Previous work on the SST-CC model specifically, has shown that this model has performed well over a small range of operating points for the “Radiver” compressor case, though flow details and turbulence quantities were not discussed. Also, an investigation into how the model captures the physical effects of curvature was not conducted. The present work will connect the effects of curvature to how the SST-CC model predicts different turbulence quantities, such as turbulence kinetic energy and Reynolds normal stresses.

### 3.4.1 Summary

Previous studies evaluating the performance of different turbulence models, including uncorrected and curvature corrected models, were discussed in this section. These studies have shown that the  $k - \epsilon$  turbulence model does not perform as well in turbomachinery applications as the  $k - \omega$  and SST models. Curvature corrected models have been shown to be feasible for use in turbomachinery, however a detailed investigation of the SST-CC model by Smirnov and Menter (2009) has not been completed. The next section provides an overall summary and analysis of the literature review.

### 3.5 Summary and analysis of the literature review

An overall review of the literature reveals the large extent and variety of work that has been completed on the investigation of curvature effects. The literature of relevance to the current work can be branched into four sections: curvature effects, turbulence modelling, turbulence modelling with respect to curvature and turbulence modelling in turbomachinery applications. The following paragraphs briefly summarize the past work within the scope of the current work and discuss how the current work contributes to this area of research.

In terms of curvature effects, several experiments have been completed previously to investigate the flow mechanisms associated with curved surfaces. Much of the experimental work used simplified cases in a variety of geometries, however many studies have been completed using curved ducts. The curved duct is an excellent geometry for these types of problems, allowing researchers to extract valuable information about the flow mechanisms behind curvature as well as the effects of curvature magnitude and directionality, changes in  $Re$  and the presence of favourable or adverse pressure gradients, without the complexities associated with more practical applications. Many theoretical characteristics of flow with curvature such as secondary flows due to the curvature induced pressure gradients from the concave to the convex walls, TG style vortices on the concave wall, and typical velocity and turbulent kinetic energy profiles have been extracted from

experiments. The issue arises with more complex geometries, such as in turbomachinery applications. It is more difficult to obtain a characterization of the entire flow field, for example, in a centrifugal compressor, due to a complex shape, high velocities and limited probe access. For this reason, researchers direct their focus towards numerical modelling for these types of applications.

From a numerical perspective, many researchers have looked at the sensitivity of different turbulence models with respect to curvature effects, again with a focus on curved ducts. Due to the wide range of experimental work, there is a large amount of data available for validation, making these cases quite ideal. From these studies, different eddy viscosity turbulence models have been evaluated in terms of their ability to predict curved flows, however eddy viscosity models are not naturally sensitive to curvature because of the local isotropy assumption. Thus, more recently, researchers have focussed on developing curvature corrected models, which are variations of different eddy viscosity models, adjusted to predict more accurate flow fields in applications with curvature. Smirnov and Menter (2009) recently developed a curvature corrected version of the SST model, denoted SST-CC, for this purpose. In this work, the SST-CC model was chosen based on its proven sensitivity to curvature in simplified cases by Smirnov and Menter, the availability of the model for future researchers and the proven performance of the original SST model in turbomachinery applications (Bourgeois et al., 2011, Roberts & Steed, 2004).

The SST-CC model, among other curvature corrected models, has been used to some extent in predicting turbomachinery flows. However, this study investigates the reasoning behind the improved prediction associated with curvature corrected models. Smirnov and Menter (2009) briefly discuss the global performance of the SST-CC model in the Radiver test case (Ziegler et al., 2003), however they did not get into the details in terms of flow field or discuss any local regions of curvature where the curvature correction would be activated.

Therefore, the current work furthers the investigation of the SST-CC model in turbomachinery applications, in terms of extending the understanding of the effects of the curvature correction on flow fields and turbulence quantities. The current work not only investigates the performance of the SST-CC model in two turbomachinery applications, but it also investigates a simplified geometry modelled similar to a centrifugal impeller. The simplified geometry eliminates the complexities associated with a turbomachinery flow and creates a connection between curvature effects in a simplified geometry and curvature effects in a complex compressor geometry. Curvature effects are evaluated by deconstructing various terms in the SST model equations and comparing the results in the simplified geometry to the results in the compressor impellers, as well as against the known curvature effects relating to turbulence quantities.

In the next chapters, the numerical setup for the CFD simulations of the aforementioned compressors is discussed in detail. This includes a description of the geometry, matching in flight test conditions, boundary conditions, meshing and a description of the solver.

## **4. CENTRIFUGAL COMPRESSORS – NUMERICAL SETUP**

---

This work first considers applying curvature corrected models to practical industry flows. Two different centrifugal compressor stages designed by P&WC for use in their aero-engines will be investigated in detail in this study. The current chapter outlines the geometry, flow conditions and numerical setup for the two compressors studied in this work, known as the 307C and 1C compressors.

### ***4.1 Description of the geometry***

Both compressors analyzed have a similar geometry, however, there are some minor differences between the two geometries, which will be highlighted in this section.

#### ***4.1.1 The 307C centrifugal stage***

The 307C centrifugal stage consists of a rotating split impeller (inducer and exducer regions) and a stationary fishtail pipe diffuser (see Figure 9), which generates a pressure ratio of  $\sim 2.5$ . The impeller comprises of 31 curved blades and the diffuser has 22 stationary fishtail pipe passages. The purpose of the impeller is to increase the flow kinetic energy and the diffuser uses a gradually increasing cross-sectional area which converts the high kinetic energy flow into a high pressure energy flow before entrance into the combustor section. For numerical simplicity only 1 blade passage and 1 diffuser passage are being analyzed, as shown in Figure 10, and periodic boundary conditions are used. This condition will be described in more detail in §4.3.

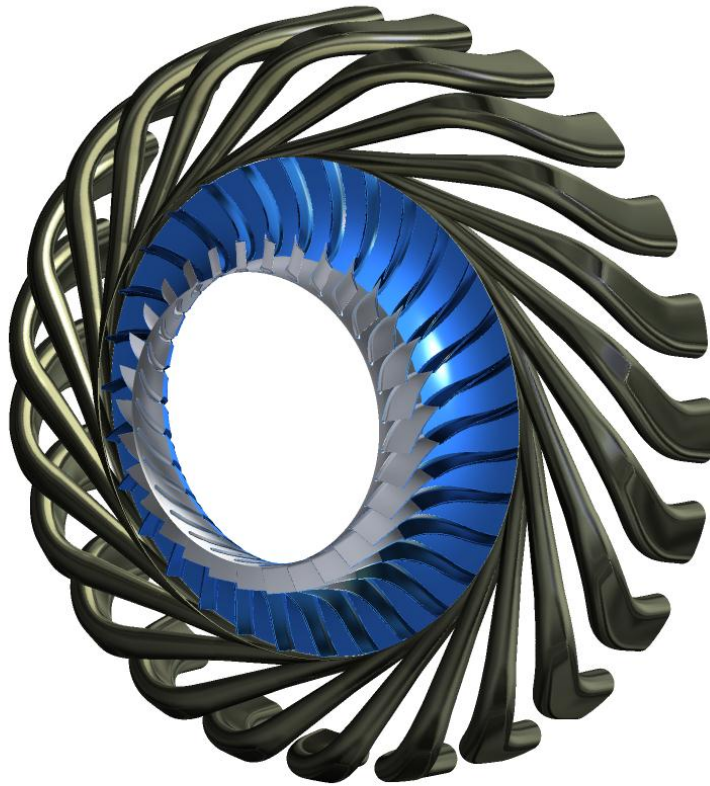


**Figure 9: Full model of the 307C stage; consisting of 31 impeller blades split between an inducer (silver) and an exducer (blue) and 22 diffuser passages (brown).**

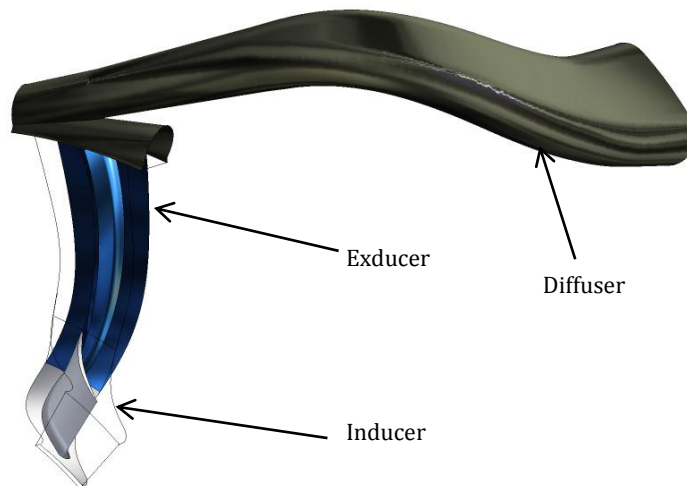


**Figure 10: Section of 307C centrifugal stage (computational domain)**

#### 4.1.2 The 1C centrifugal stage

The 1C centrifugal stage shown in Figure 11, is a more compact centrifugal stage than 307C, while still providing a pressure ratio of roughly 2.5. It consists of a smaller impeller with a tighter curvature than the 307C, as well as a longer diffuser pipe. The purpose of this more compact design is to reduce the size and weight of the aero-engine in which it is used. This stage also has fewer blades and more diffuser pipes with 28 impeller blades and 26 diffuser pipes as compared to 31 blades and 22 diffuser pipes in the 307C stage. Similar to the 307C, only 1 blade passage and 1 diffuser passage are being analyzed numerically as shown in Figure 12. Note that in this case, the blade is one solid surface and not split into an inducer and exducer as in the 307C case.

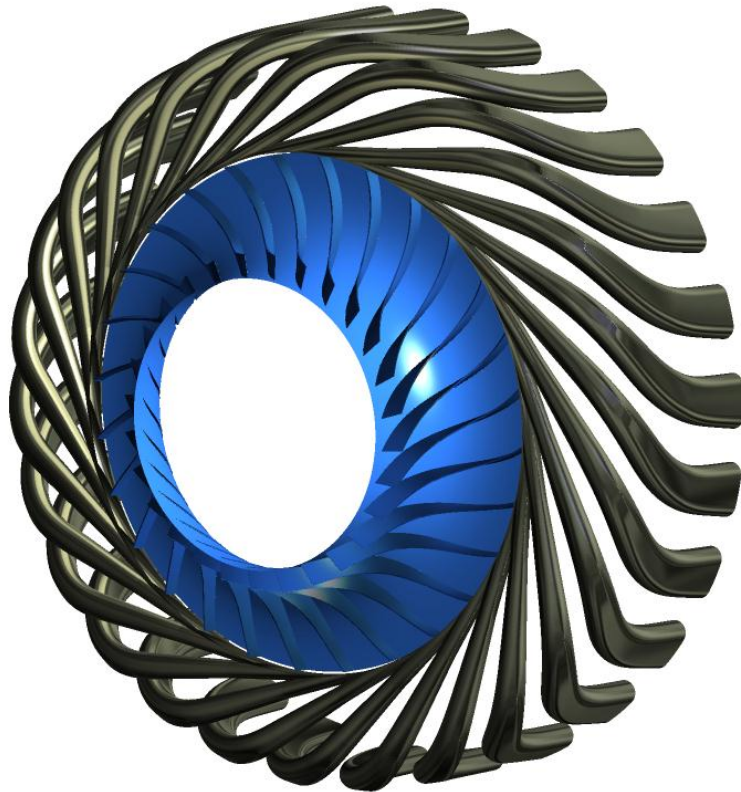


**Figure 11: Full model of the 1C stage; consisting of 28 impeller blades (blue) and 26 diffuser passages (brown).**



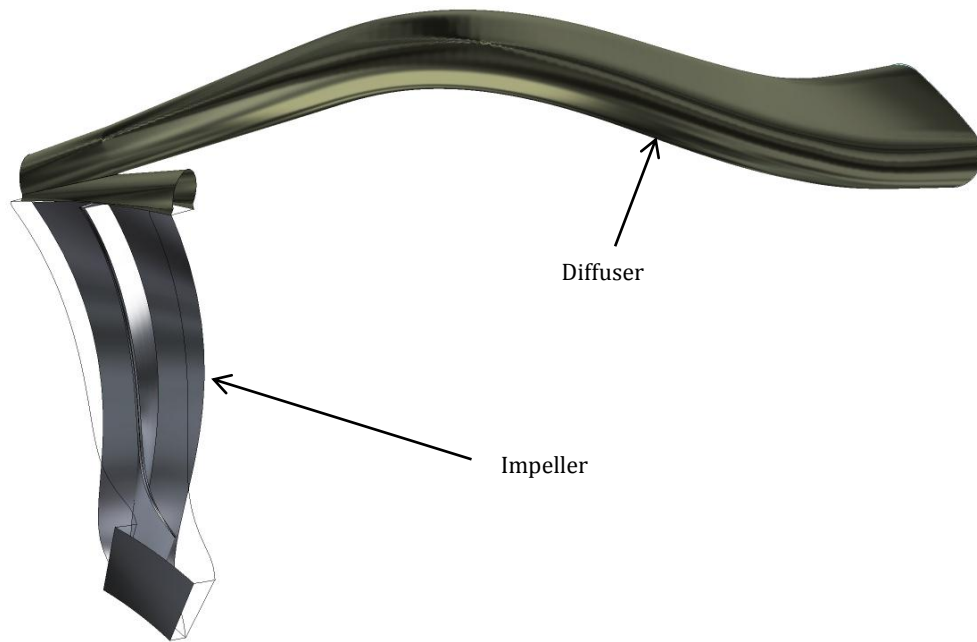


**Figure 12: Section of 1C centrifugal stage being analyzed numerically**

## **4.2 Matching test rig and in-flight conditions (1C)**

### *4.2.1 Application of non-dimensional parameters*

Since the compressors in question are investigated at test rig conditions (i.e. at ground level), certain non-dimensional parameters need to be matched to ensure that the test rig conditions and the in-flight conditions are dynamically similar. The important non-dimensional parameters to match are the total-to-total pressure ratio, the corrected mass flow and the corrected speed, given by equations 4.1 to 4.3, respectively (Dixon & Hall, 2010, p. 35). The power coefficient is another non-dimensional parameter of interest (Eq. 4.4 (Dixon & Hall, 2010, p. 35)), however it is not as important as the first three listed. Note that in Eqs. 4.1 - 4.4,  $\gamma$  is the ratio of specific heats (Eq. 4.5).

$$p_{04}/p_{01} \tag{4.1}$$

$$\frac{\dot{m}\sqrt{\gamma RT_{01}}}{D^2 p_{01}} \quad (4.2)$$

$$\frac{ND}{\sqrt{\gamma RT_{01}}} \quad (4.3)$$

$$\frac{\Delta T_0}{(\gamma - 1)T_{01}} \quad (4.4)$$

$$\gamma = \frac{c_p}{c_v} \quad (4.5)$$

It is common practice to drop the  $\gamma$  and  $R$  parameters in these non-dimensional groups for industrial applications mainly because the effects of these parameters are usually minimal (Dixon & Hall, 2010, p. 35). Consequently, a certain level of accuracy is sacrificed for simplicity by doing so. Table 5 illustrates the differences between the  $R$  and  $\gamma$  values for the test rig and in-flight conditions. In this study, the effects of including  $\gamma$  and  $R$  in the corrected speed calculation were investigated by comparing compressor performance characteristics at two different corrected speeds. The two different corrected speeds were found, based on either including or not including the effects of the different  $\gamma$  values, and performance characteristic curves were simulated for each corrected speed.

**Table 5: Comparison of the test rig and in flight  $R$  and  $\gamma$  values for the 1C stage simulations**

	Test Rig Condition	In Flight Condition
$R$ (J/kg · K)	287	287
$\gamma$ (based on volume average)	1.401	1.375

The results of either including or not including the effects of the different  $\gamma$  values in the corrected speed calculation are given in Figure 13. Note that in these speedlines, the horizontal axis represents the corrected mass flow rate, given by Eq. 4.6. Recall that location 1 represents the impeller inlet.

$$\dot{m}_{c1} = \dot{m}_1 \frac{\sqrt{T_{01}/T_{ref}}}{p_{01}/p_{ref}} \quad (4.6)$$

The purpose of the non-dimensional parameters is to ensure that the test rig simulations are run at the appropriate corrected speed to match the performance characteristics of the in-flight condition, in which the compressor runs at a higher rotational speed. It is clearly shown in Figure 13 that when  $\gamma$  is included in the corrected speed calculation, the results from the test rig simulations match the results from the in-flight condition with greater precision than when  $\gamma$  is not included in the calculation. When  $\gamma$  is not included in the calculation, the PR and corrected mass flow are both under predicted across the entire speedline, though these effects are more apparent towards the high mass flow end of the performance curve (the choke region).

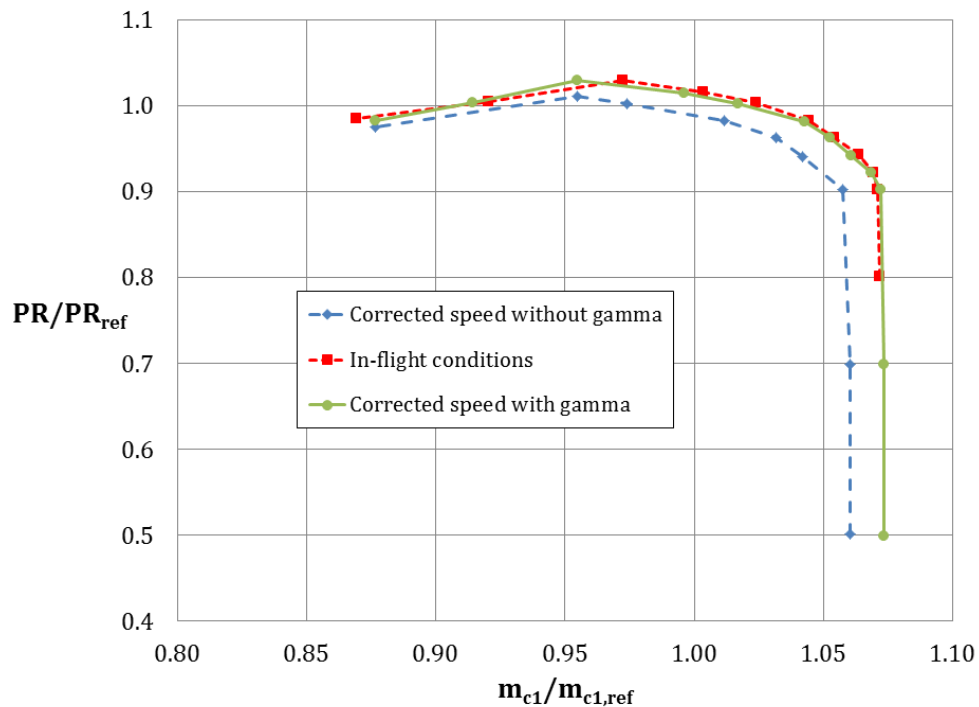


**Figure 13: Comparison of speedlines (normalized pressure ratio vs. corrected mass flow) for the 1C stage between the in-flight and test rig conditions with and without  $\gamma$  in the corrected speed calculation**

Thus the results of this comparison show that even for cases where the change in  $\gamma$  is relatively small, the effects of including or not including  $\gamma$  when matching the non-

dimensional parameters, specifically the corrected speed, can be significant. By including the change in  $\gamma$  between the test rig and in-flight conditions in the calculations a higher level of accuracy is maintained. From this point forward, only the corrected speed including  $\gamma$  will be used for all computations and plots, and it is denoted “test rig conditions”.

#### 4.2.2 Application of Reynolds number corrections for efficiency

Since the test rig and in-flight conditions differ in terms of rotational speed, density and viscosity,  $Re$  based on rotational speed ( $Re_N$ ) (Eq. 4.7) will be different for these two cases. More specifically the ratio of in-flight to test rig  $Re_N$  is roughly 3:1.  $Re$  corrections can be applied to correct for this difference to ensure that the test rig and in-flight conditions are within a reasonable margin after accounting for the difference in  $Re_N$ . Two  $Re$  corrections were tested: the Hutton correlation and the Ackeret correlation as presented in Eqs. 4.8 and 4.9, respectively (Turton, 1995, p. 37), where the subscript  $m$  denotes “model” which represents the test rig in this case and no subscript represents the in-flight case. These correlations were applied to the in-flight efficiency line to calculate the test rig speedline after accounting for the difference in  $Re_N$ , as shown in Figure 14. Although the Hutton and Ackeret correlations are more traditionally used in scaling up hydraulic machinery (Turton, 1995, p. 37), they provide a useful approximation for the inclusion of  $Re$  effects in this case.

$$Re_N = \frac{\rho ND^2}{\mu} \quad (4.7)$$

$$\frac{1 - \eta}{1 - \eta_m} = 0.3 + 0.7 \left( \frac{Re_m}{Re} \right)^{0.2} \quad (4.8)$$

$$\frac{1 - \eta}{1 - \eta_m} = 0.5 \left[ 1 - \left( \frac{Re_m}{Re} \right)^{0.2} \right] \quad (4.9)$$

With the application of these correlations to the in-flight efficiency line, the Hutton correlation showed an average difference of 0.7% as compared to the test rig efficiency line, whereas the Ackeret correlation showed an average difference of 1.8%. Nevertheless, both the Hutton and Ackeret correlations depicted the slight decrease in efficiency that arises from running the compressor at a lower  $Re$ . Therefore, this analysis showed that the test rig conditions, while running at the corrected speed including the change in  $\gamma$ , are dynamically similar within a minimal margin of error (0.7 – 1.8%).

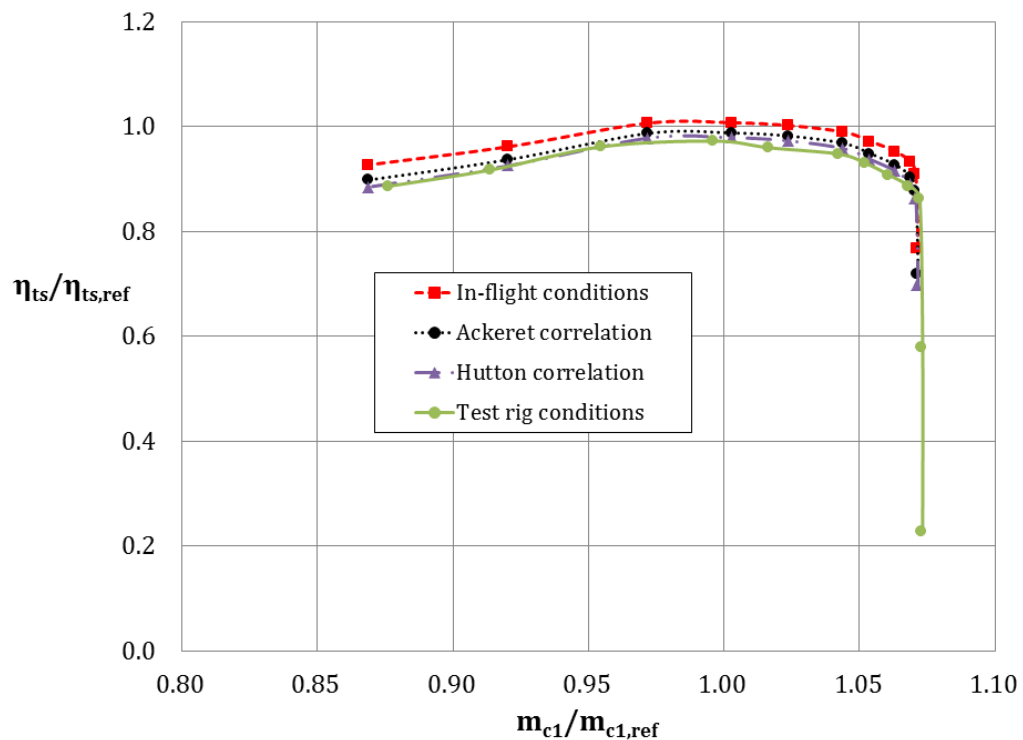


**Figure 14: Efficiency plot for test rig conditions after applying the Hutton and Ackeret Reynolds number corrections to the in-flight condition**

### 4.3 Boundary conditions

The boundary conditions for each of the compressor stages are very similar, with the exception of there being an extra boundary condition at the inducer/exducer interface for the 307C stage, thus they will both be described in the following

section. The boundary conditions are listed in Table 6, with the surfaces shown schematically in Figure 15, and are described in depth in §§4.3.1 – 4.3.4.

**Table 6: Summary of boundary conditions for each location in the centrifugal compressors**

Location	Boundary Condition
<b>Impeller Inlet</b>	Total pressure $\left(p_0 = p_s \left[1 + \frac{\gamma-1}{2} M^2\right]^{\frac{\gamma}{\gamma-1}}\right)$ , total temperature $\left(T_0 = T_s \left[1 + \frac{k-1}{2} M^2\right]\right)$ and flow angles ( $\alpha$ )
<b>Hub Surface</b>	$U = V = W = 0$ , and $Q = 0$ (adiabatic)
<b>Shroud Surface</b>	$U = V = W = 0$ , and $Q = 0$ (adiabatic)
<b>Blades</b>	$U = V = W = 0$ , and $Q = 0$ (adiabatic)
<b>Periodic Sides</b>	Rotational periodicity ( $\Delta p = 0$ across periodic surfaces)
<b>Impeller Exit/Diffuser Inlet</b>	Mixing plane interface (see §4.3.2 for details)
<b>Impeller Back-Face Bleed</b>	$\dot{m} = \% \text{ of } \dot{m}_1$
<b>Diffuser Walls</b>	$U = V = W = 0$ , and $Q = 0$ (adiabatic)
<b>Diffuser Outlet</b>	$p = p_s$ or prescribed $\dot{m}$

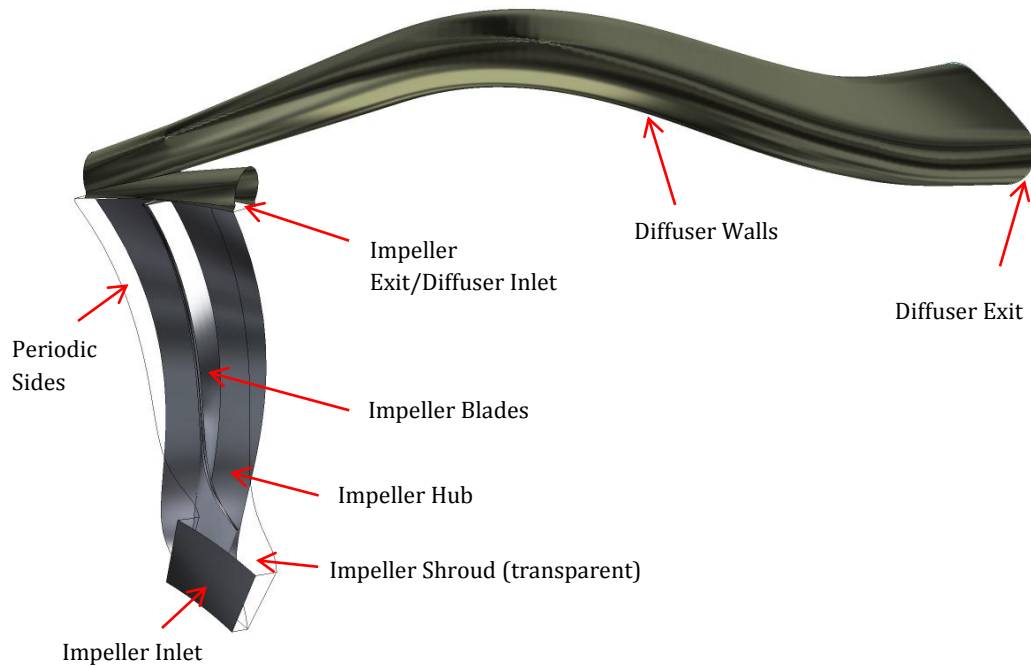


**Figure 15: Schematic of the boundary condition surfaces (1C compressor geometry)**

#### 4.3.1 *Impeller inlet*

The impeller inlet boundary condition was set in the subsonic flow regime as a stationary frame total pressure with prescribed flow angles. These inlet values were taken from the numerical results of the axial compressor stage exit (provided by P&WC), which is located before the centrifugal stage inlet in the aero-engine itself. The stationary frame total temperature was also prescribed as the heat transfer boundary condition at the impeller inlet, again taken from results from the previous axial compressor stage.

#### 4.3.2 *Impeller exit/diffuser inlet*

At the region where the rotating impeller meets the stationary diffuser ring, a mixing plane interface technique is used to branch the two reference frames. This method was investigated thoroughly in the previous work of Bourgeois (2008). The basic concept of the mixing plane approach is that circumferentially averaged fluxes are applied across the interface, profiles computed at the exit of the impeller (rotating frame of reference) are used as the inlet to the diffuser (stationary frame of reference) and fluxes for mass, momentum and energy are conserved across the interface. The solver iterates to find the steady state solution between these two reference frames.

#### 4.3.3 *Diffuser exit*

One of two different boundary conditions was applied to the diffuser exit depending on the location of the operating point on the speedline. In the stall region of the speedline, where overall pressure ratio is relatively constant, a specified exit mass flow condition was applied. Conversely, in the choke region of the speedline, where the mass flow is constant, a specified static pressure outlet condition was applied. In the region between the limits of stall and choke, one of the two conditions was applied. In this region, the mass flow rate exit and pressure exit were found to predict the same values for PR, mass flow and efficiency.

#### 4.3.4 Other boundary conditions

For the other boundary conditions listed in Table 6, all of the solid surfaces (hub surface, shroud surface, the blades and the diffuser walls) were set as no-slip, adiabatic, smooth walls. A small mass flow outlet was simulated at the exit of the impeller in an area called the impeller back-face bleed. Since only one impeller blade passage and one diffuser pipe were simulated, rotationally periodic boundary conditions were applied to represent the entire geometry. Mass, momentum, turbulence and heat transfer fluxes were all conserved across these boundaries, and the automatic mesh connection method was used since the grids were the same on each side of the periodic boundaries.

#### 4.4 Meshing

The meshes for both the 307C and 1C compressor stages were similarly setup, with some minor changes due to differences in the geometry. The mesh for the 307C case was created by Bourgeois (2008) and the mesh for the 1C case was created by personnel at P&WC, both using the commercial software ICEM CFD (Ansys ICEM CFD 13.0 User Guide, 2010). The number of elements in each section of the two geometries is presented in Table 7 and more details on each of the meshed sections are presented in §§4.4.1 - 4.4.3.

**Table 7: Summary of mesh types and number of elements for the two compressor cases**

<b>Compressor</b>	<b>Region</b>	<b>Mesh Type</b>	<b>Number of Elements</b>
<b>307C</b>	Inducer	Structured Hexahedral	~ 750,000
<b>307C</b>	Exducer	Structured Hexahedral	~ 1.1 M
<b>307C</b>	Diffuser	Unstructured Tetrahedral	~ 2.1 M
<b>TOTAL</b>	<b>Impeller + Diffuser</b>	-	<b>~ 3.95 M</b>
<b>1C</b>	Impeller	Structured Hexahedral	~ 1.1 M
<b>1C</b>	Diffuser	Unstructured Tetrahedral	~ 3.2 M
<b>TOTAL</b>	<b>Impeller + Diffuser</b>	-	<b>~ 4.3 M</b>

##### 4.4.1 Impeller mesh

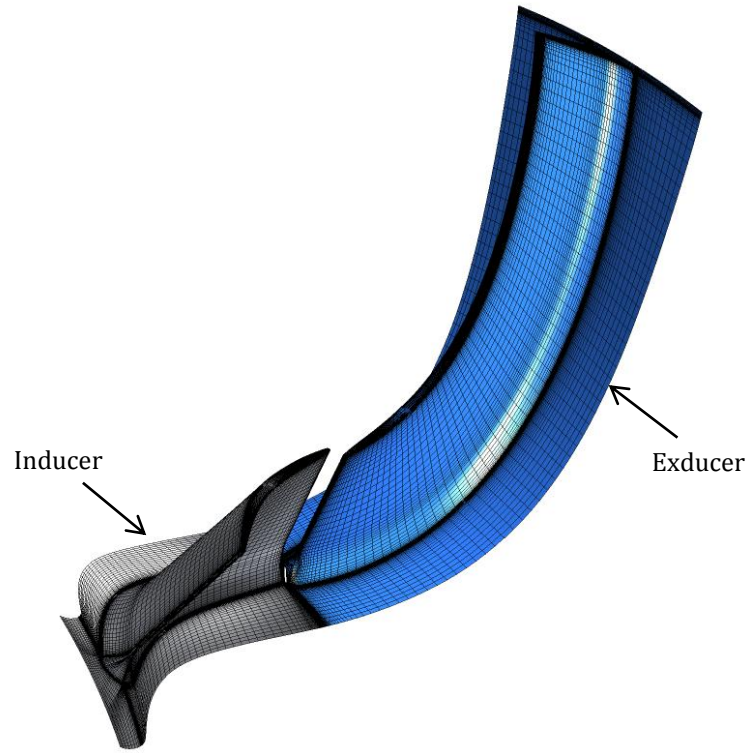
Both impellers were meshed using a structured hexahedral grid, with a higher mesh density near any walls surfaces to appropriately capture the boundary layer flow as



well as a high mesh density near the blade leading edge to capture any shock effects. There were some added complexities with the 307C impeller mesh (Figure 16a) because of the split impeller design; which necessitated an extra mesh interface at the intersection of the inducer and exducer. More details on this mesh can be found in (Bourgeois et al., 2011), which was the primary study using this geometry and mesh. On the other hand, the 1C impeller mesh (Figure 16b) is more straightforward since it is not a split impeller and there was no need for an additional interface. Because of the split impeller design and the slightly larger impeller size, the 307C impeller mesh contained approximately 750,000 more elements in the impeller than in the 1C compressor cases (Table 7).

#### *4.4.2 Diffuser mesh*

The diffusers were primarily meshed with an unstructured tetrahedral mesh, with some prism layer mesh at the diffuser exit to capture the boundary layer flow. The unstructured mesh was chosen because of the complex surface geometry throughout the diffuser domain, especially in regions near the diffuser inlet where there are several surface intersections.



(a) 307C



(b) 1C

Figure 16: Structured hexahedral mesh for the (a) 307C impeller and (b) 1C impeller

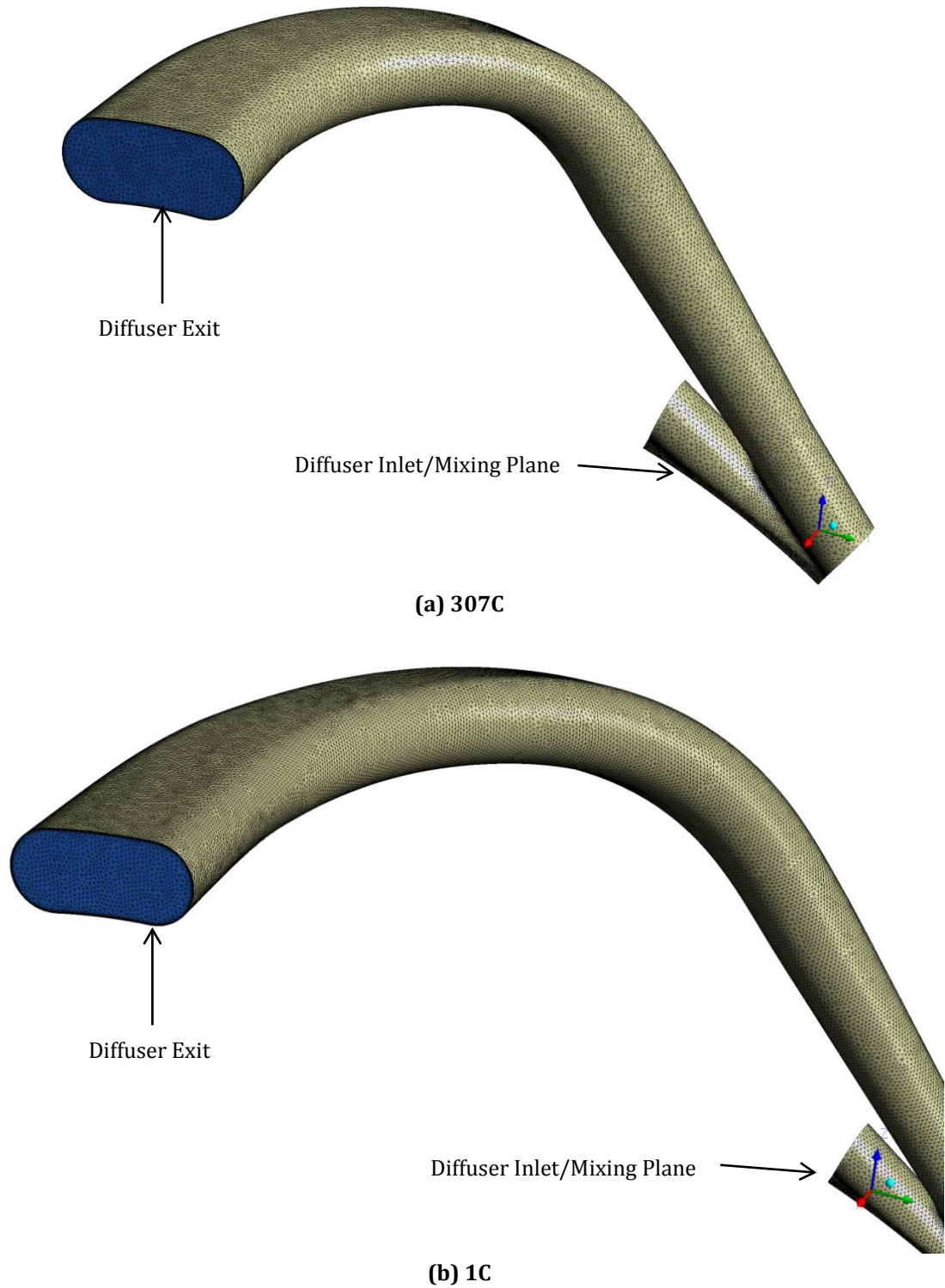
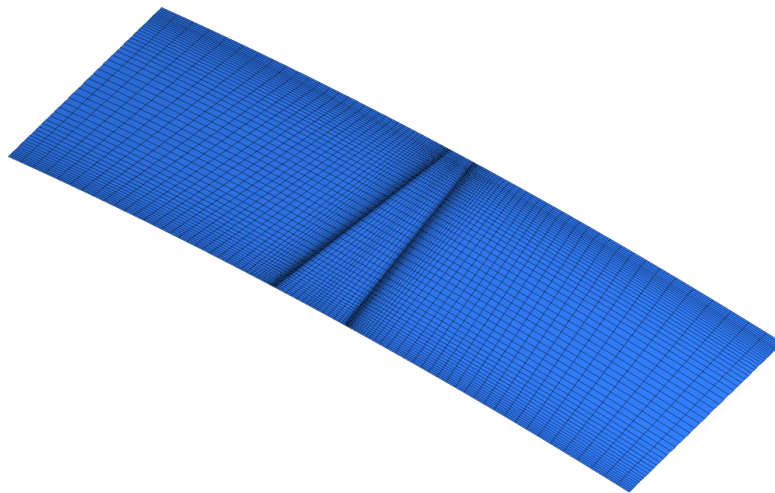


Figure 17: Unstructured tetrahedral diffuser mesh for (a) 307C compressor and (b) 1C compressor.

#### 4.4.3 *Mixing plane mesh*

As mentioned in the previous section discussing boundary conditions, a mixing plane technique was used to connect the impeller exit in the rotating reference frame to the diffuser inlet in the stationary reference frame. Because the impeller side of the mixing plane was meshed with a structured hexahedral mesh (Figure 18a) and the diffuser side of the mixing plane was meshed with an unstructured tetrahedral mesh (Figure 18b), these meshes had to be connected using a general grid interface (GGI) mesh connection to ensure continuity. GGI connections are able to stitch two mesh surfaces together, regardless of the node location, mesh type or surface shape (Ansys CFX-Solver Theory Guide, Version 13.0, 2010). These characteristics are convenient for these particular cases, since due to a mismatch in the number of impeller passages and diffuser pipes, the two sides of the mixing plane are not exactly the same size; which is not a concern when using this connection style.



**(a) Impeller side**

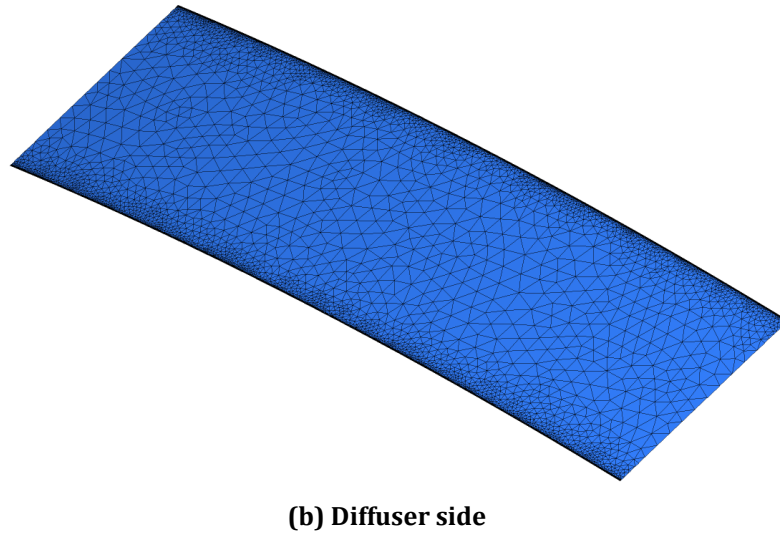


**Figure 18: Connection interface for the mixing plane. (a) Structured hexahedral impeller side and (b) unstructured tetrahedral diffuser side**

#### 4.4.4 $y^+$ values and wall functions

Different wall function approaches have been used for both the SST based models and the RSM-SSG model, however all the compressor meshes were created to have  $y^+$  values close to unity (1 – 10, or within the viscous sub-layer) wherever possible to ensure ideal near wall conditions regardless of the model used. Certain regions with more complex flow conditions, such as near the blade tips or near the mixing plane, have larger  $y^+$  values between 10 and 200, however they are still within the log layer. The SST models ( $\omega$ -based models) use automatic wall functions, which benefit from small values of  $y^+$  that are equal to or less than unity, thus establishing the need for the near wall mesh refinement. Automatic wall functions will switch from using wall functions to integrating to the wall based on feedback by the solver on the mesh spacing (Ansys CFX-Solver Theory Guide, Version 13.0, 2010). On the other hand, the RSM-SSG model uses scalable wall functions, which are improved from standard wall functions in that they can be applied to refined meshes. With standard wall functions, the first node normal to a wall surface needed to be in the log layer ( $30 < y^+ < 300$ ) (Figure 19), however with scalable wall functions, the first node can be in the viscous sublayer or the log layer, and the wall functions will be applied once a limit of  $y^+$  is reached by the solver (i.e. once the solver discovers a

node in the log layer) (Ansys Inc., 2010). In other words, the scalable wall functions will simply disregard any elements in the viscous sublayer. Thus, both model types can be run using the same mesh.

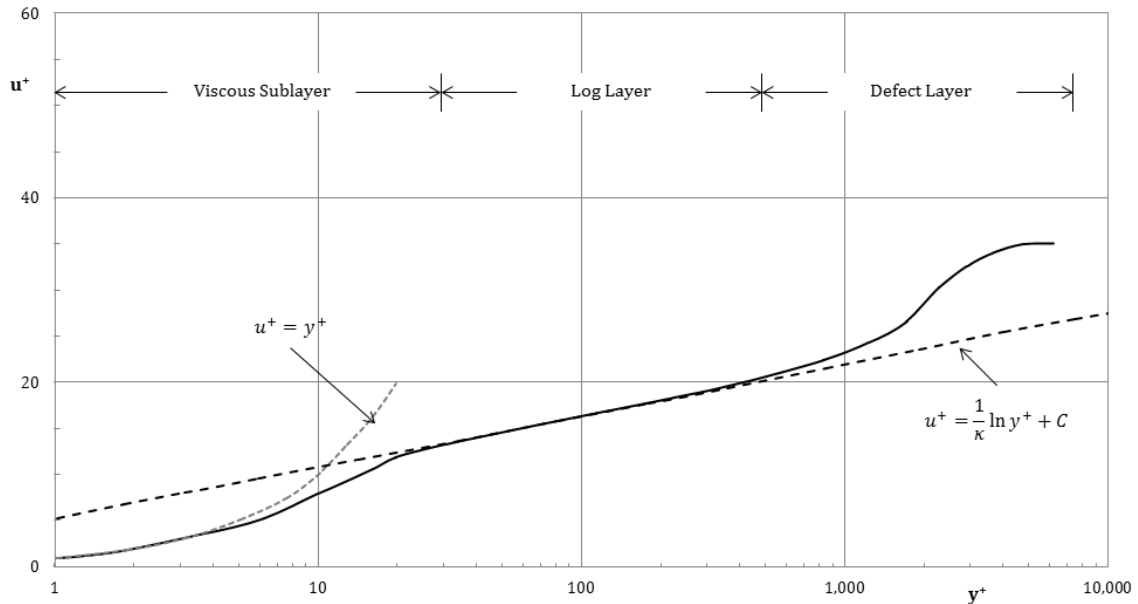


**Figure 19: Law of the wall, adapted from Wilcox (2006, p. 17)**

#### 4.4.5 Grid independence

Grid independence studies have been completed for both of the test cases. Bourgeois et al. (2011) performed a detailed grid independence study for the 307C compressor case, and personnel at P&WC performed a grid independence study for the 1C case compressor case prior to the simulations presented herein.

#### 4.5 Solver description

ANSYS CFX 13.0 was used for the simulations of the different compressors stages. CFX 13.0 is a coupled solver that uses a finite volume method to discretize the domain. It uses a pseudo time-stepping method for steady state solutions, which gradually steps the solution forward towards the final steady solution.

Some of the previous results for the 307C compressor were computed using ANSYS CFX 11.0 and the data were extracted from Bourgeois et al. (2011). An investigation

was conducted to compare any differences between the two solvers and it was found that in terms of bulk parameters (e.g. characteristic curves, efficiency curves), the differences between the two solvers is minimal (<1%). Some discrepancies were found in the flow fields at regions of high separation and low momentum, such as in the diffuser exit, however the differences were deemed to be negligible.

#### 4.5.1 Advection schemes

In terms of advection schemes, a high resolution scheme was used for the continuity, momentum and energy equations. The high resolution scheme is a second-order upwind scheme that uses a non-linear variable,  $\beta$ , at each node, as shown in Eq. 4.10 (Barth & Jespersen, 1989), where  $\phi$  is the quantity of interest, the subscripts “ $ip$ ” and “ $up$ ” denote the values at the integration point and the upwind node, respectively, and  $\vec{r}$  is the vector between the integration point and the upwind node.

$$\phi_{ip} = \phi_{up} + \beta \nabla \phi \cdot \Delta \vec{r} \quad (4.10)$$

A first-order upwind scheme was used for all turbulence quantities. The first-order scheme uses the same concept shown in Eq. 4.10, however  $\beta$  has a value of 0 in this case and thus,  $\phi_{ip} = \phi_{up}$ . Turbulent transport equations for  $k$  and  $\epsilon$  (for example) are source dominated as opposed to convection dominated, and thus a first-order scheme is acceptable for these quantities.

#### 4.5.2 Solver control and output control

Each simulation was run for at least 500 iterations and convergence criteria were set at  $10^{-5}$  for residuals and 0.001 (or 0.1%) for the global balances of the conservation equations. Some of the simulations did not reach the residual target of  $10^{-5}$  (between  $10^{-4}$  and  $10^{-5}$ ) for all parameters, however these simulations were run until the residuals levelled out to ensure convergence.

Monitor points were set for three bulk parameters within the impeller/diffuser system as a further check for solution convergence. The simulation was not considered converged until all of these monitor points reached steady state values.

First was the total-to-static pressure ratio, defined by the ratio of the static pressure at the diffuser outlet to the total pressure at the impeller inlet as shown in Eq. 4.11. Second was the total-to-total temperature ratio, defined by Eq. 4.12. Finally, the maximum Mach number in the diffuser passage was monitored to determine whether or not the stage was choked (Mach number greater than 1 in the diffuser). All three parameters were computed in the stationary reference frame.

$$PR = \frac{p_4}{p_{01}} \quad (4.11)$$

$$TR = \frac{T_{04}}{T_{01}} \quad (4.12)$$

Note that all of the aforementioned information relating to solver control and output control was strictly for the 1C simulations and the SST-CC simulations for the 307C case. Details on the RSM-SSG setup and results from the 307C case can be found in the original paper (Bourgeois et al., 2011).

#### **4.6 Summary**

This chapter outlined the numerical setup for both the 307C and 1C centrifugal compressor cases. Geometry, meshing, boundary conditions and solver setup were discussed as well as the application of non-dimensional parameters to match the in-flight and test rig conditions. The application of the non-dimensional parameters revealed the importance of including  $R$  and  $\gamma$  in the corrected speed calculation. The next chapter outlines the numerical setup of the simplified geometry, which is based on the geometry of the 1C compressor described in this chapter.



## 5. SIMPLIFIED GEOMETRY – NUMERICAL SETUP

---

In this work, a simplified geometry case is used to isolate curvature effects from the complex centrifugal compressor case. This case idealizes the flow through one impeller passage, while still maintaining the same curvature and flow characteristics of the 1C centrifugal stage. The current chapter gives details on the geometry, the idealizations that were applied (as compared to the 1C centrifugal case), as well as the numerical setup for the simulations in terms of meshing, boundary conditions and solver description.

### *5.1 Description of the geometry*

The geometry for the simplified compressor impeller was based on the 1C centrifugal stage in development by P&WC. A single impeller passage of that stage is presented in Figure 20. By eliminating the blades as well as the rotation in the system, the impeller was simplified to a stationary curved duct style geometry (Figure 21), with a similar curvature to the actual impeller. This curved section represents a  $10^\circ$  section of the full axisymmetric geometry (shown in Figure 22).  $10^\circ$  was chosen to be close to the actual impeller passage pitch, since the 1C impeller consists of 28 blade passages, or  $(360^\circ/28) \approx 13^\circ$  per passage.

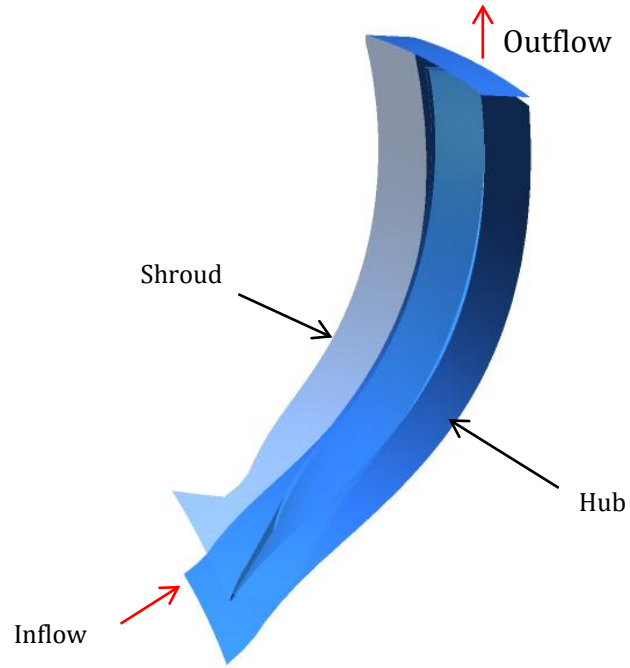


**Figure 20: Centrifugal impeller passage for the 1C compressor stage**

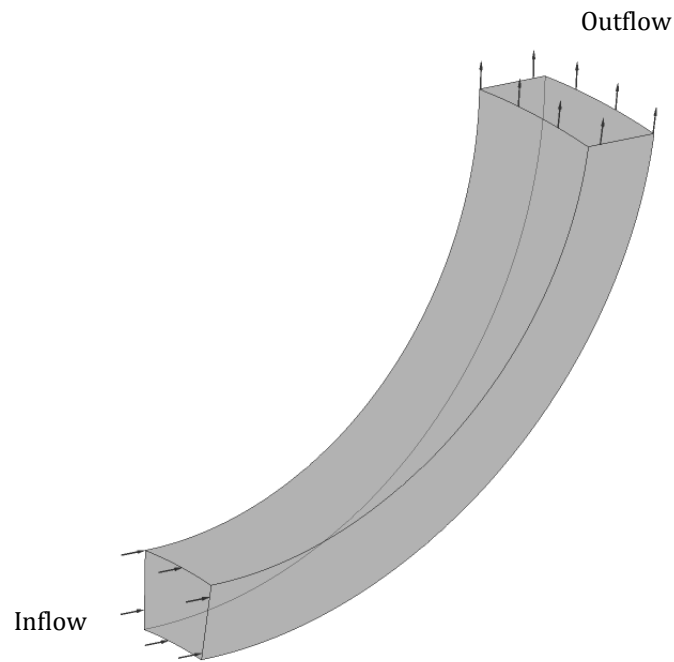


**Figure 21: Simplified version of a centrifugal compressor impeller passage**

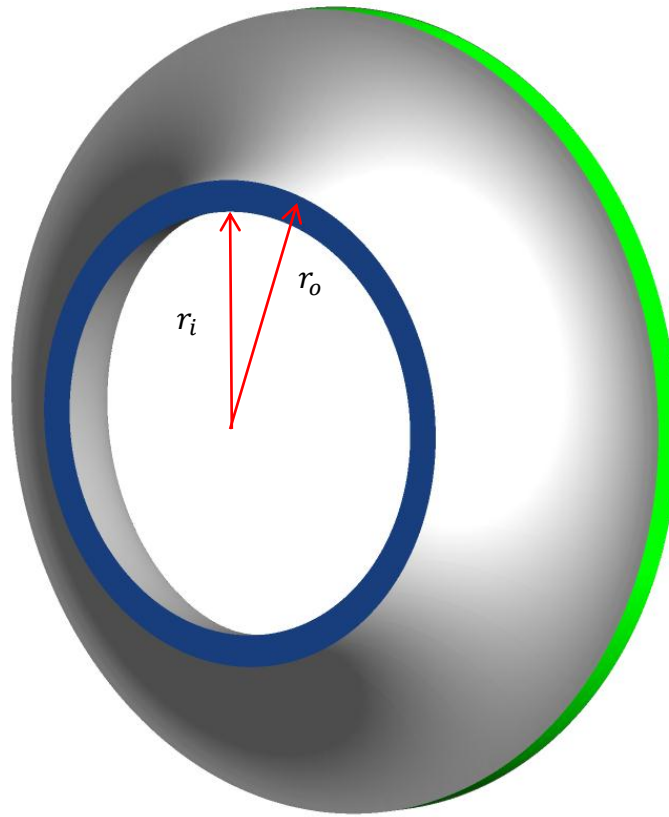


**Figure 22: Full 360° rotation of the simplified geometry**

To eliminate the effects of developing flow, the geometry was altered by adding an additional section in front of the curved portion, as shown in Figure 23. The length of this straight section was calculated based on an entrance length ( $L_e$ ) calculation for turbulent flows, as shown in Eq. 5.1 (White, 2011, p. 354). This equation is traditionally used for circular pipes, but for this case the hydraulic diameter for an annulus (Eq. 5.2) was substituted in place of the traditional pipe diameter. In Eq. 5.2,  $r_o$  and  $r_i$  represent the outer and inner radii of the annulus, respectively, measured from the centreline (see Figure 22). The entrance length calculated using Eq. 5.1 was extended by  $\sim 10\%$  to further ensure fully developed flow, since the mentioned approximations were used, resulting in an entrance length of  $40D_h$ .

$$\frac{L_e}{D_h} \approx 4.4Re_{D_h}^{1/6} = 4.4 \left( \frac{\rho U D_h}{\mu} \right)^{1/6} \quad (5.1)$$

$$D_h = 2(r_o - r_i) \quad (5.2)$$

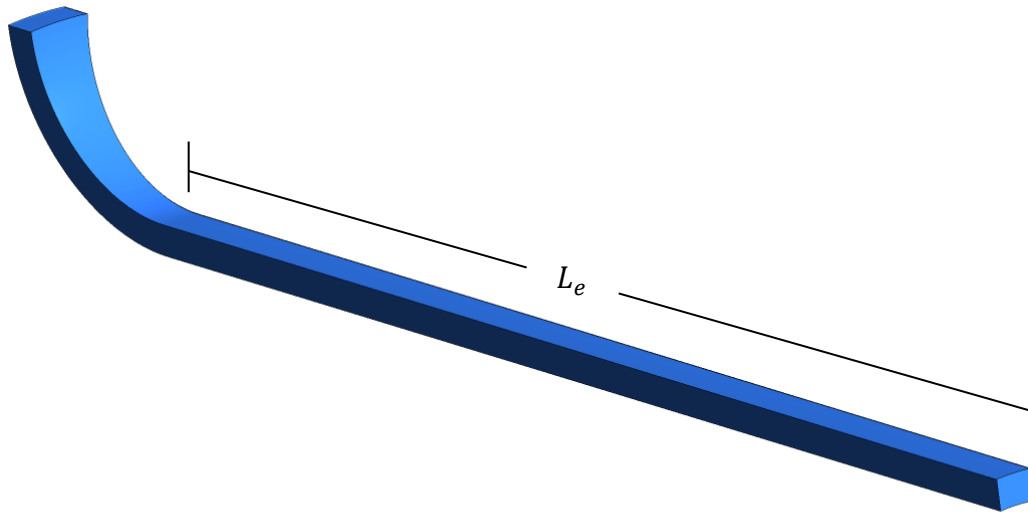


**Figure 23: Straight section added to ensure fully developed flow at the curved section inlet**

## ***5.2 Idealizations from the centrifugal case***

The simplified geometry contains idealizations in regards to matching the 1C centrifugal case. These idealizations relate to the geometry as well as the flow field, and include: no blades or rotation, unidirectional curvature, fully developed flow in the curved section and constant temperature.

### ***5.2.1 No blades or rotation***

The main idealization in the simplified geometry is the absence of rotation and blades to generate a pressure rise, as is the case in a centrifugal compressor. Rotation and curvature have similar effects, depending on the frame of reference of the flow (Piquet, 1999, p. 612). Thus, by removing rotation effects, the curvature effects in the stationary reference frame can be compared between the simplified geometry and the centrifugal compressor.

Furthermore, as was described in the literature review chapter, pressure gradients can detract from curvature effects since pressure gradients have similar effects. In

addition to the pressure rise generated by the rotating blades, the centrifugal compressor impeller imparts a converging cross section to aid in increasing the velocity of the flow. This converging section, in combination with the rotation of the impeller, induces more pressure gradients in the flow. In the simplified geometry, the height of the cross section remains constant, which limits the presence of pressure gradients.

### *5.2.2 Unidirectional curvature*

In both the centrifugal impeller and the simplified geometry cases, the dominant curvature is in the longitudinal (or streamwise) direction. However, in the centrifugal impeller case, the passage is curved (or “twisted”) in the circumferential direction, which was not modelled in the simplified case. The unidirectional curvature is idealized, however in both cases the longitudinal curvature is the dominant curvature direction, so this simplification is justifiable.

### *5.2.3 Fully developed flow*

With the addition of a long straight section in the simplified geometry, the effects of developing flow are eliminated in the curved section. With fully developed flow, another complexity is removed from the simplified geometry test case. In the centrifugal case, the inlet profiles are taken from the upstream axial compressor outlet, which are not symmetric, fully developed profiles.

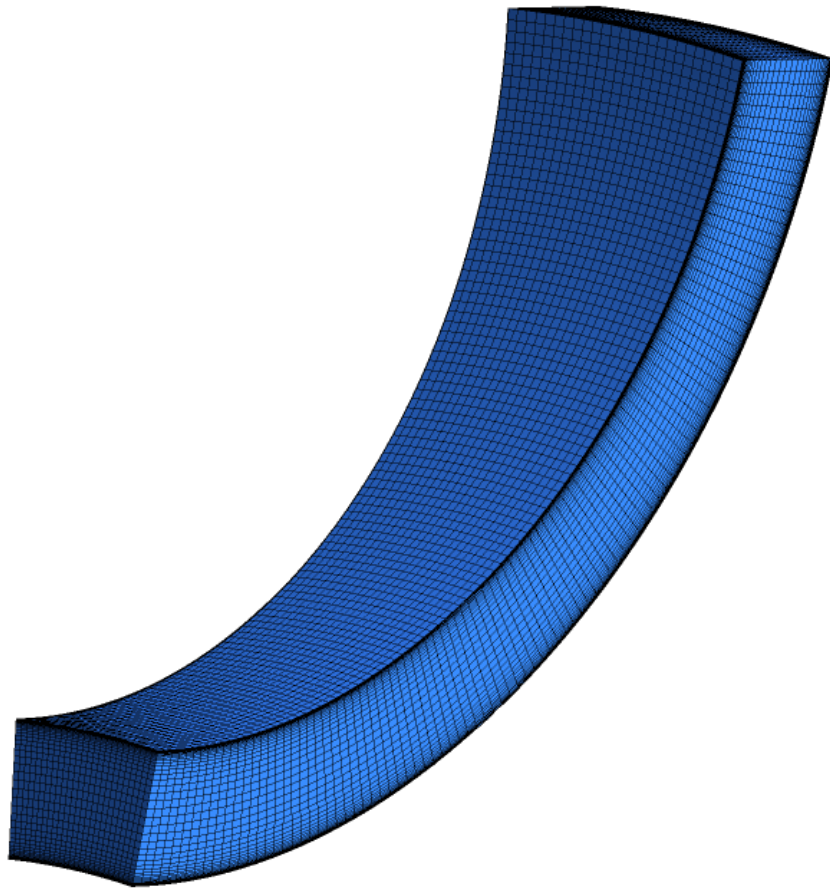
### *5.2.4 Constant temperature*

In the 1C centrifugal compressor, there is a large increase in temperature from inlet to outlet. This is an inherent characteristic in compressors; however in the simplified geometry, the simulations were performed under isothermal conditions, again to remove any added complexities from the flow.

## **5.3 Meshing**

The geometry was meshed using the commercial meshing software ICEM CFD (Ansys ICEM CFD 13.0 User Guide, 2010). A structured blocking method was used to

generate a structured hexahedral mesh with added layers near the wall surfaces to fully capture the boundary layer, as shown in Figure 24 (a) and (b).  $y^+$  values were set to be  $\sim 1$  immediately adjacent to all wall surfaces, to benefit from the automatic wall functions used with the SST and SST-CC models. The same mesh was used for the RSM-SSG simulations, and scalable wall functions were used to eliminate any issues with the small  $y^+$  values and the  $\epsilon$  formulation of the RSM-SSG model.



(a)

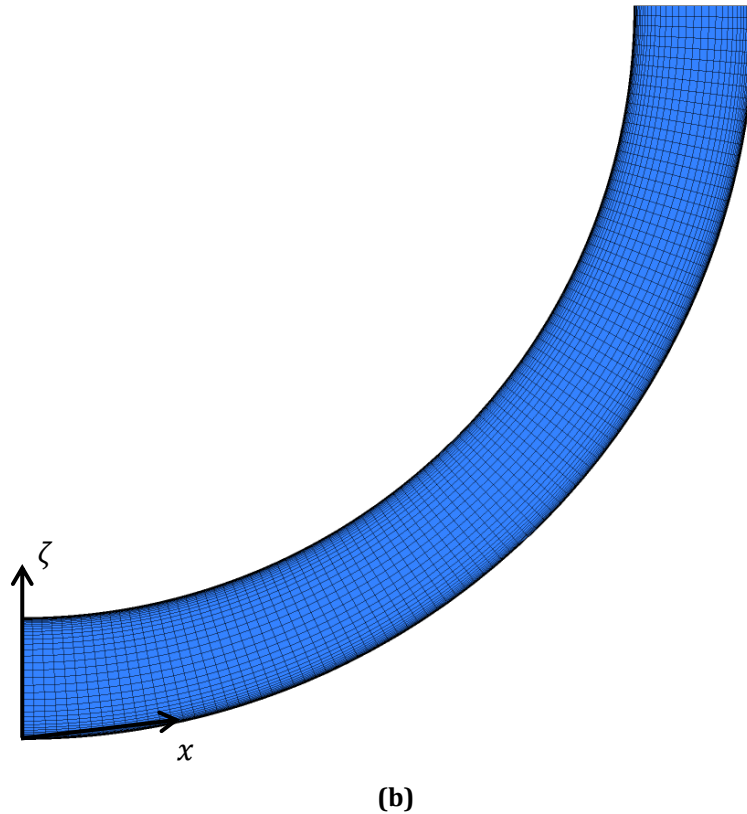


**Figure 24: Hexahedral mesh used in the simplified geometry. (a) Isometric view and (b) side view**

### 5.3.1 Grid independence study

A grid independence study was completed for the curved section only, using three meshes with different grid densities and an increasing numbers of elements. The study was performed using the SST turbulence model only. Details on the meshes are presented in Table 8. The following mass flow averaged (MFA) variables were compared at the domain outlet to show mesh independence: total pressure, turbulence kinetic energy (TKE) and streamwise velocity. Using these variables, the three meshes were compared in terms of percent differences as shown in Table 9. These comparisons showed that all of the differences were less than 1%, and are therefore minimal enough to ensure solution independence, and consequently the coarse mesh was used from this point forward since it required the least computational time. Mean velocity and turbulence kinetic energy profiles were also compared at the outlet of the curved section and showed nearly no difference across

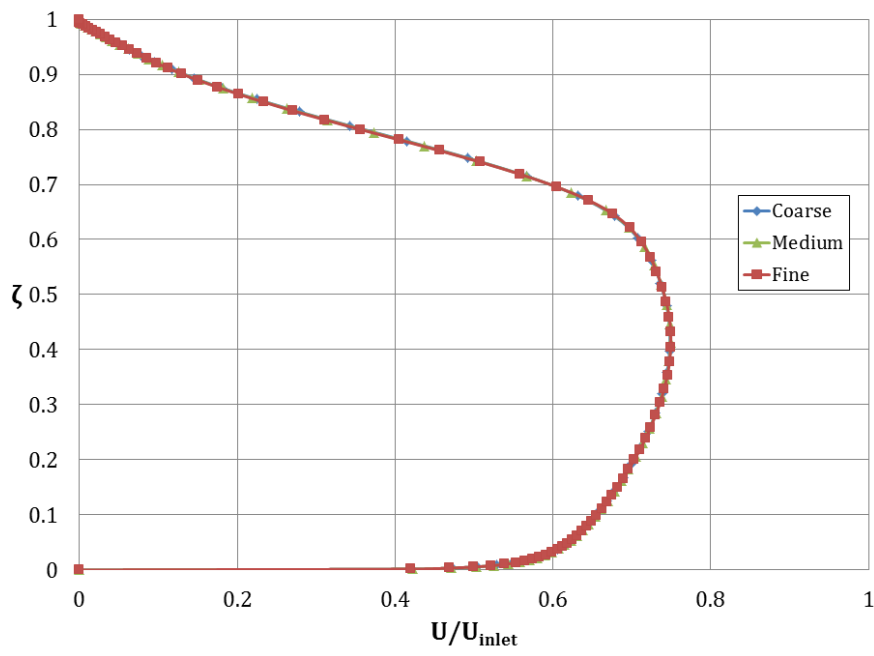
the section (see Figure 25). Note that in Figure 25,  $\zeta = 0$  represents the concave surface and  $\zeta = 1$  represents the convex surface, in the curvilinear coordinate system shown in Figure 24.

**Table 8: Details on the meshes for the grid independence study**

Name	Number of Elements	Multiple of previous mesh
Coarse	141075	-
Medium	224315	1.59
Fine	435527	1.94

**Table 9: Comparison of mass flow averaged (MFA) outlet flow variables for the three meshes**

Comparison	% Difference in MFA Total Pressure (Pa)	% Difference in MFA TKE ( $\text{m}^2/\text{s}^2$ )	% Difference in MFA Velocity (m/s)
Coarse vs. Medium	0.19%	0.27%	0.09%
Medium vs. Fine	0.16%	0.19%	0.07%
Coarse vs. Fine	0.35%	0.46%	0.16%



**(a)**



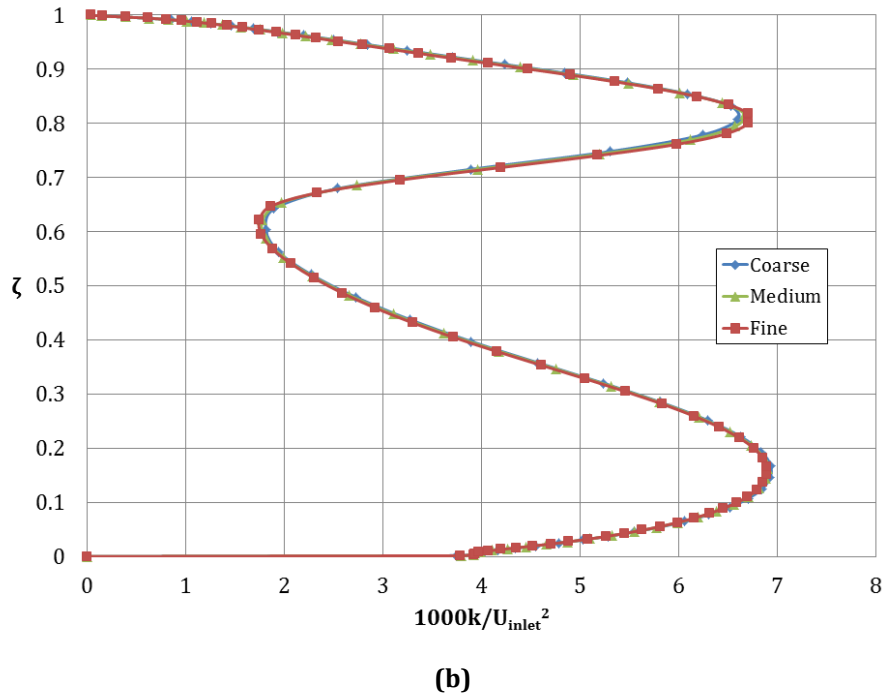


Figure 25: Comparison of velocity and TKE at the outlet using different meshes. (a) Velocity and (b) TKE

#### 5.4 Boundary conditions

The inlet condition was set as a normal velocity of 150 m/s so that  $Re_{D_h}$  ( $2.9 \times 10^5$ ) of the annulus cross section at the inlet was similar for both the centrifugal compressor impeller and simplified geometry.  $Re_{D_h}$  was used as opposed to  $Re_N$  ( $\rho ND^2/\mu$ ) because the simplified geometry does not rotate. The outlet was set to a static pressure outlet of 0 Pa to simulate a free opening into the surrounding atmosphere. The convex and concave surfaces were set as no-slip smooth wall boundary conditions. Periodic boundary conditions were used to simulate the full  $360^\circ$  geometry using a  $10^\circ$  section.

#### 5.5 Solver description

The commercial solver ANSYS CFX 13.0 was used for the steady state simulations. The same high resolution schemes used in the centrifugal cases were used for the continuity and momentum equations, as well as all turbulence quantities.

Automatic wall functions were used for the SST and SST-CC models, whereas scalable wall functions were used for the RSM-SSG model. Further details on the different wall functions of on the advection schemes can be found in §4.4.4 and §4.5.1, respectively.

### 5.5.1 Turbulence models

The same three turbulence models (SST, SST-CC and RSM-SSG models) used in the centrifugal compressor cases were also used in these simulations. Details on each of these models can be found in §3.2.

### 5.5.2 Convergence criteria

Each simulation was run for 200 iterations and convergence criteria were set at  $10^{-7}$  for residuals and 0.001 (0.1%) for the global balances of the conservation equations. Monitor points were set at five different locations to measure the changes in the mean velocity throughout the domain. In all cases, both the residuals and the monitor points reached a steady state and were within the designated convergence criteria.

## 5.6 Summary

This chapter described details on the simplified geometry in terms of the geometry itself, the idealizations and limitations of the geometry and flow characteristics, and the numerical setup of the problem. Meshing, boundary conditions and solver details were discussed. The next two chapters discuss the results from each of the compressor cases: the 307C and the 1C, respectively. Both of these cases are related back to the simplified geometry discussed in this chapter, however this relation is more so between the simplified geometry and the 1C compressor, since they share a more similar curvature and  $Re_{D_h}$ .

## 6. 307C COMPRESSOR RESULTS

---

This compressor has been tested previously, numerically and experimentally, by Bourgeois et al. (2011). In that previous study, the  $k - \epsilon$  model, the SST model, the SST-RM (SST with reattachment modification) model and the RSM-SSG model were tested against available experimental data. The current investigation will use the previous experimental and numerical data (RSM-SSG) to compare against the results from the SST-CC model. Note that in all the following plots, the results have been normalized to protect P&WC proprietary data.

The results from the simulations are examined in two different aspects. First, the results from the SST, SST-CC and RSM-SSG simulations are compared in terms of their characteristic curves for total-to-static pressure ratio and total-to-static efficiency, as well as against experimental data at the impeller-diffuser interface and at the diffuser exit. Second, the SST-CC model results are investigated in terms of the effects of the production multiplier,  $f_{r1}$ .

### 6.1 Global performance – PR and efficiency

Past experiments were completed on the centrifugal compressor stage at P&WC in Longueuil, Quebec by Bourgeois et al. (2011). Shakedown tests were performed to obtain the characteristic curves for the centrifugal stage, including pressure ratio and efficiency for 100% design speed and laser Doppler velocimetry (LDV) measurements were taken at different locations along the stage, providing velocity profiles for comparison.

The speedline for the 307C stage is shown in Figure 26. This shows the variation in total-to-static stage PR with corrected inlet mass flow rate, with stall being represented by the far left points and choke being represented by the far right points on the speedline. From this plot, it may be seen that there are differences in the performance predictions by the SST, SST-CC and RSM-SSG models.

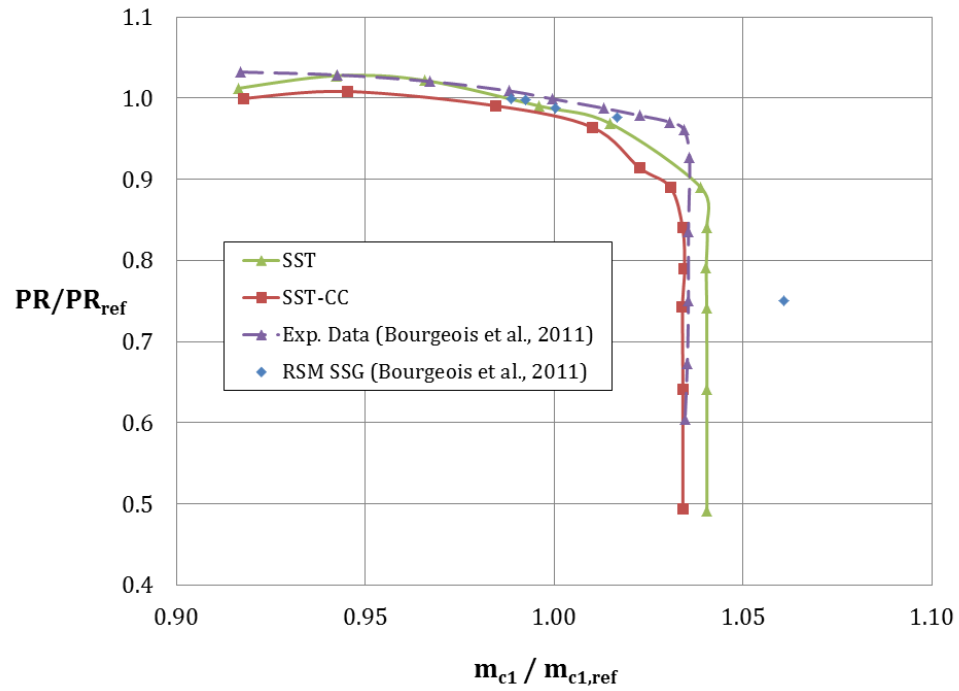


Figure 26: Comparison of 307C compressor speedlines from the SST and SST-CC models with experimental data and RSM-SSG results from Bourgeois et al. (2011) at 100% design speed

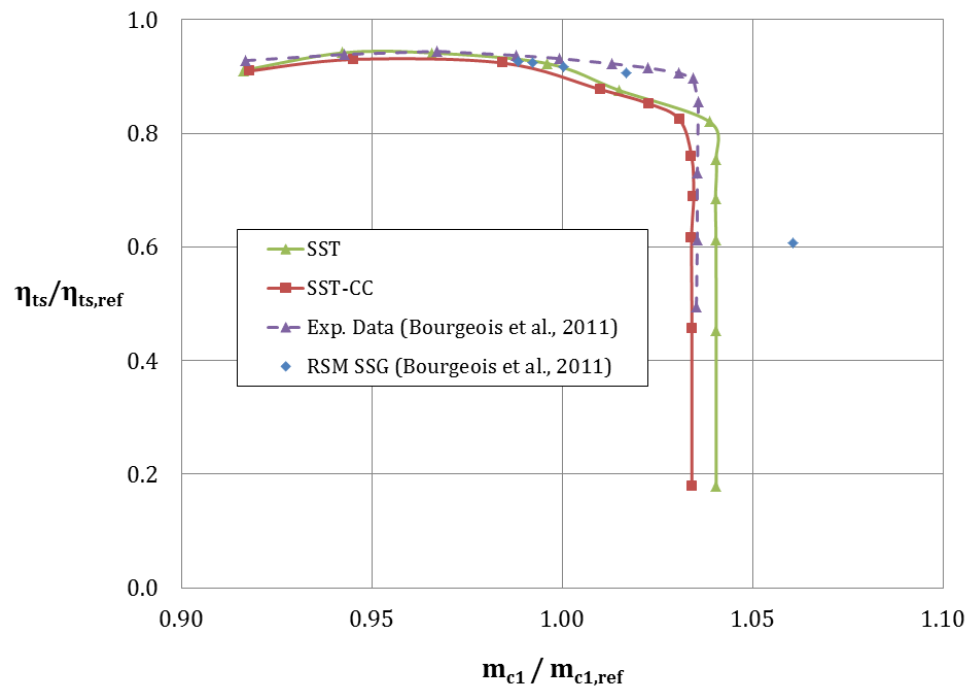


Figure 27: 307C compressor total-to-static efficiency line for the SST, SST-CC models compared to experimental data and RSM-SSG results from Bourgeois et al. (2011) at 100% design speed

Each of these models demonstrates improved performance, in terms of matching the experimental data, in different regions along the speedline; the SST model shows a better prediction over the SST-CC model towards the stall side, while the SST-CC model shows improvement of the choke point. At the stall point, both models underpredict the PR at stall, the SST by 1.9% and the SST-CC by 3.1%. At the choke point, the SST-CC slightly underpredicts the choke mass flow, although the prediction is within 0.15% of the experimental value. The SST model on the other hand, still yields impressive results, but overpredicts the choke mass flow by 0.47%. Both models underpredict the PR in the region between stall and choke, in the region from approximately  $\dot{m}_{c1}/\dot{m}_{c1,ref}$  1.01 to choke. The PR predicted by the SST model is very close to the experimental values in the regions from  $\dot{m}_{c1}/\dot{m}_{c1,ref}$  0.94 – 1.01. The maximum percent errors occur at the corner point of the speedline where the PR is underpredicted by both the SST and SST-CC models by 7.3%. The RSM-SSG results from Bourgeois et al. (2011) show good agreement with the experimental data around the design point, however the choke region was not well predicted by the RSM-SSG model. Points near stall were not computed for the RSM-SSG model and so a comparison near stall will not be discussed here.

The total-to-static efficiency line for the 307C is shown in Figure 27 for the SST and SST-CC models as well as experimental data and RSM-SSG results extracted from Bourgeois et al. (2011). The efficiency lines show similar trends to the speedlines, however, towards the stall side the SST-CC and SST results match the experimental data better than in the speedline. This is particularly evident in the SST-CC case, which has shifted upwards closer to the experimental data. Differences in efficiency between the experimental data and the SST and SST-CC models at the far stall point are 1.7% and 1.8%, respectively. On the choke side, there is still a difference in the choke mass flow prediction between the SST and SST-CC models, which is carried over from the speedline. Figure 27 also shows similar results between the SST-CC and SST model in the region before the choke point, although the efficiency is still underpredicted, showing maximum differences of approximately 8%.

## 6.2 Comparison with experimental data – flow field

Experimental data of the flow field for the 307C compressor are available at two different locations: the impeller-diffuser interface (or the mixing plane) and the diffuser exit. LDV measurements were taken by Bourgeois et al. (2011), providing axial and circumferential velocity profiles at the mixing plane as well as axial and circumferential velocity contours at the diffuser exit.

### 6.2.1 Impeller-Diffuser Interface (Mixing Plane)

Figure 28 and 29 show the comparisons of velocity profiles at the impeller-diffuser interface (the mixing plane) for the radial and circumferential velocities, respectively, normalized by the blade tip speed,  $U_2$ . On the  $\zeta$  axis, 0 represents the hub and 1 represents the shroud.

At this location, it is clear that the velocity profiles predicted by the SST and SST-CC models are very similar for both the circumferential and radial directions. Both the SST and SST-CC models predict results that are similar to the RSM-SSG and experimental results from Bourgeois et al. (2011). Slight differences arise in the radial velocity profiles between the SST and SST-CC models, and the RSM-SSG model in the near wall region on the shroud side ( $\zeta = 1$ ), shown in Figure 28 where there are no experimental data available. Both the SST-CC and SST models predict negative velocities, whereas the RSM-SSG does not. Also, significant differences arise in the circumferential velocity profiles between the SST and SST-CC models and the RSM-SSG model in the region near  $\zeta = 1$ , shown in Figure 29. Both the SST and SST-CC models predict a significant decrease in the circumferential velocity near  $\zeta = 1$ , while the RSM-SSG model predicts a significant increase. Experimental data are not available in this near wall region to evaluate the models. Overall, the curvature correction in the SST-CC model does not seem to have large effects on the shape of the velocity profile at this location, as compared to the SST model.

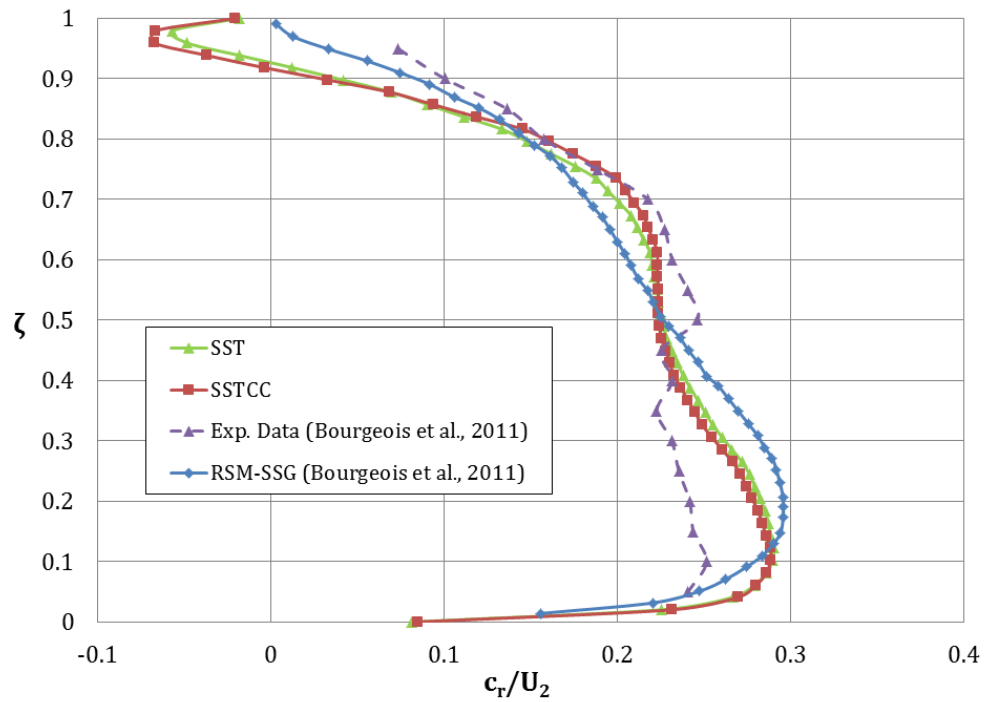


Figure 28: Radial velocity,  $c_r$ , at the mixing plane, normalized by the blade tip speed,  $U_2$

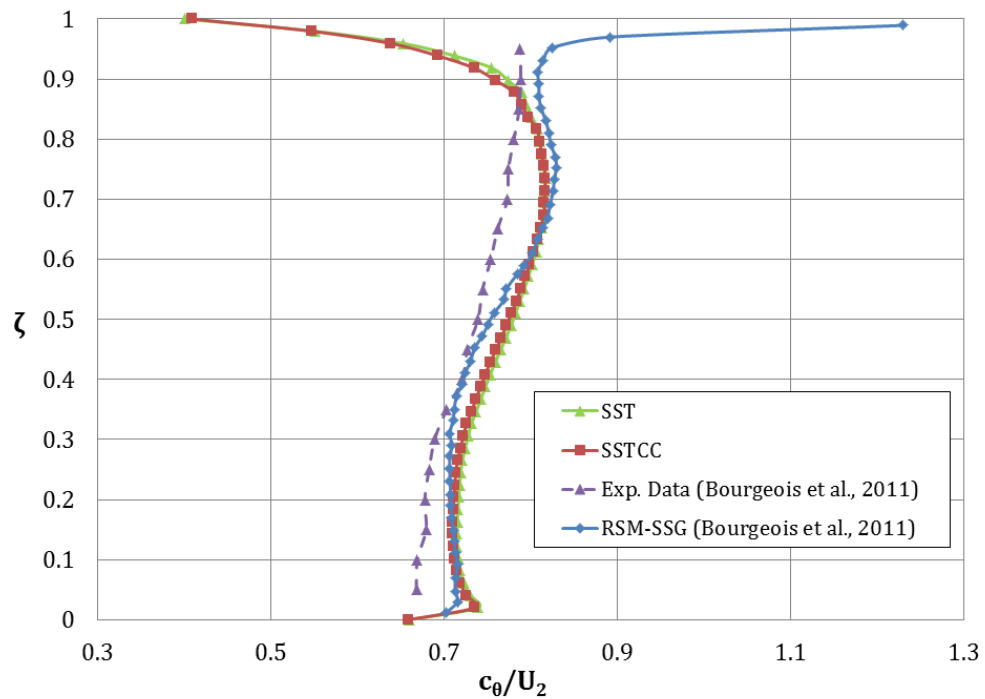


Figure 29: Circumferential velocity,  $c_\theta$ , at the mixing plane, normalized by the blade tip speed,  $U_2$

### 6.2.2 Diffuser Exit

Figure 30 shows the comparison of the axial velocity contours (primary flow direction) at the diffuser exit for the SST and SST-CC models, with the experimental data. Overall, the axial velocity predictions by the SST and SST-CC results agree well with the experimental data. On the left hand side of the diffuser exit, the SST model predicts a large region of close to zero velocity, whereas the SST-CC model does not predict such a large region, which is more consistent with the experiments. Towards the centre of the diffuser, the SST-CC model predicts very low velocity flow, which is inconsistent with the experimental data. Both models slightly underpredict the peak velocity in the high speed region on the right hand side of the diffuser exit. Overall, both models perform well in predicting the general shape of the velocity field, despite each having different local deficiencies.

Figure 31 shows the circumferential velocity contours for the SST and SST-CC models, as well as for experimental data from Bourgeois et al. (2011). The circumferential direction is the in-plane component of velocity at the diffuser exit. The circumferential velocity contours show similar trends to the axial velocity contours in that the SST and SST-CC models each have localized deficiencies. In the red coloured (high velocity) region on the right hand side, the SST model predicts a much larger high velocity zone than found in the experiments, while the SST-CC predicts a more reasonable distribution. On the other hand, the blue coloured zone (low velocity region) is better predicted using the SST model which predicts a much smaller negative velocity region, more like the experimental data. Therefore, it is difficult to conclusively say which of the two models is better matched to the experimental data; both models have performed fairly well in capturing the axial velocity flow field in this region.



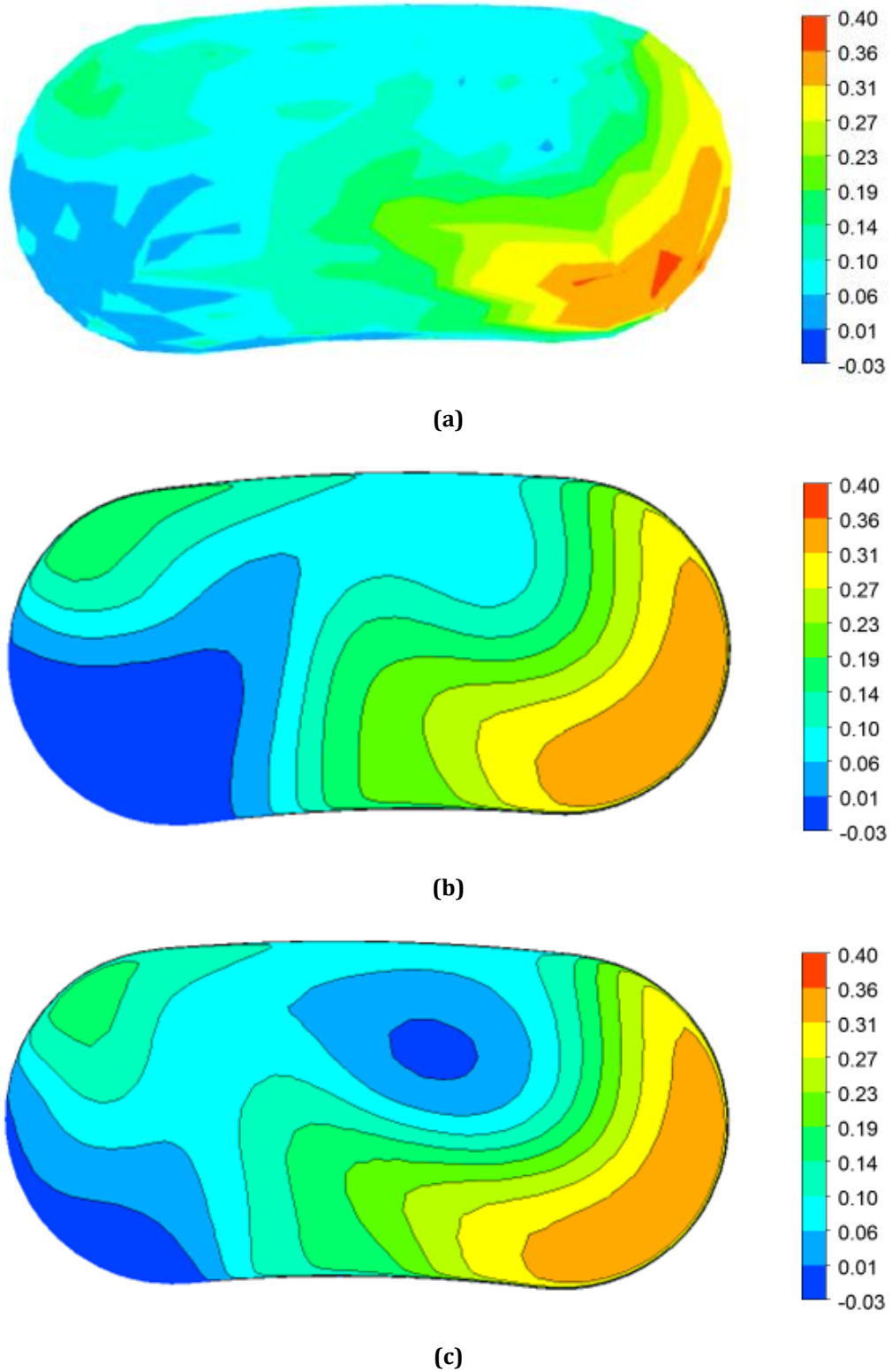


Figure 30: Axial velocity contours at the diffuser exit, normalized by the blade tip speed. (a) Experimental data (Bourgeois et al., 2011) (b) SST model (c) SST-CC model

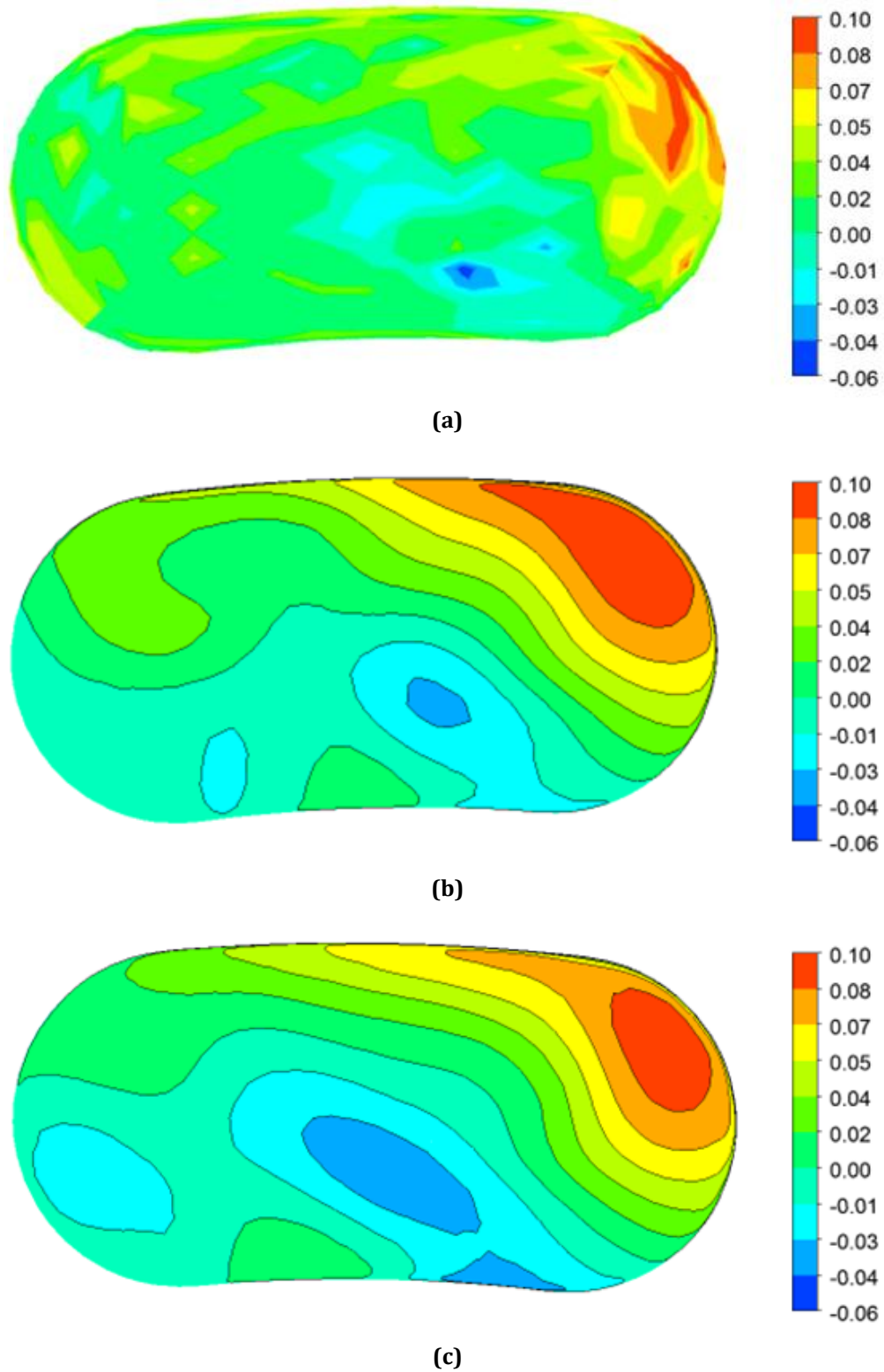


Figure 31: Circumferential velocity contours at the diffuser exit, normalized by the blade tip speed. (a) Experimental data (Bourgeois et al., 2011) (b) SST model (c) SST-CC model

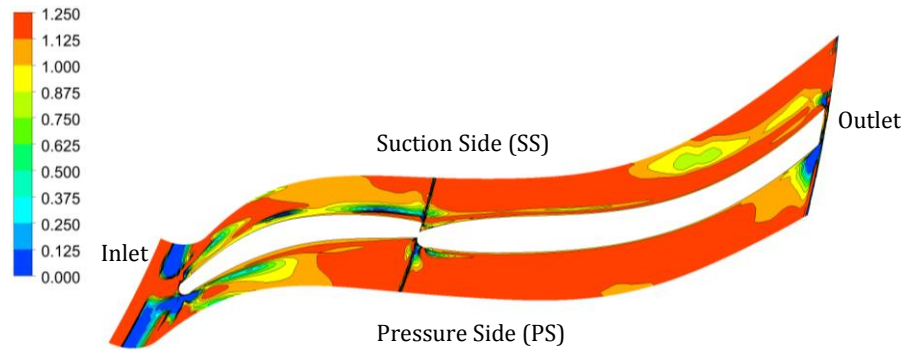
### 6.3 Investigation of the production multiplier, $f_{r1}$

The difference between the SST and SST-CC models occurs in the production of TKE term,  $P_k$ . The SST-CC model includes a production multiplier term,  $f_{r1}$ , which either limits or increases  $P_k$  depending on the presence of curvature. For example, consider a concave curvature, which enhances turbulence. This curvature would lead to a multiplier between 1 and 1.25, effectively increasing the magnitude of the production term. On the other hand, a convex curvature, which suppresses turbulence, which would result in a multiplier between 0 and 1, in effect decreasing the production term. With this in mind, it is interesting to look at the effect of the production multiplier in a geometry that is quite complex.

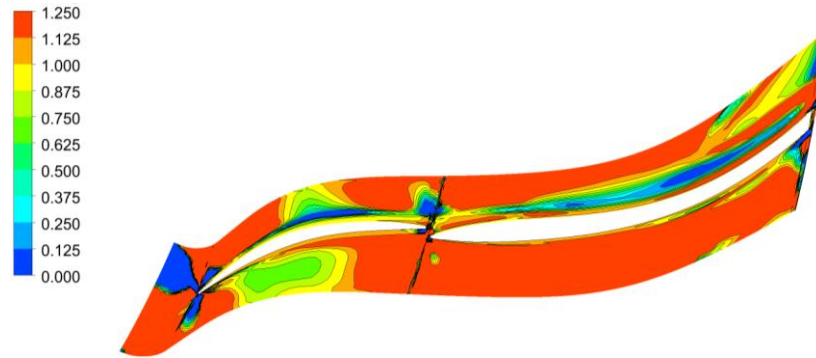
Figure 32 shows the development of  $f_{r1}$  at different spanwise locations (5, 25, 50, 75 and 95%) in the compressor impeller, progressing from the hub to the shroud. In terms of curvature, this means progressing from CCV to CVX curvature. In this figure, the left side is the impeller inlet and the right is the impeller exit, the top is the suction side (SS) and the bottom is the pressure side (PS).

The development of  $f_{r1}$  across the span of the impeller demonstrates the implementation of the  $f_{r1}$  term and the magnitude of the effect it has on the turbulence production term. Starting at 5% span (Figure 32a), a large region of  $f_{r1} > 1$  is visible in the exducer section as well as in the inducer region. From a qualitative perspective, this effect is as expected, since CCV curvature tends to enhance production, and 5% span is close to the CCV side of the impeller. Advancing towards the CVX side of the impeller (the shroud), a gradual reduction is seen in the magnitude of  $f_{r1}$ , as would be expected from the decreased turbulence production that comes from a CVX surface. This is more apparent looking at the exducer section, where  $f_{r1}$  changes from primarily between 1.125 and 1.25 at 5% span, to very few values above 1 at 75% span (Figure 32d). This transition also occurs in the inducer region, although it is not as drastic, likely because the inducer is not as curved as the exducer. The 95% span region (Figure 32e) shows the reduction in turbulence production that is consistent with the presence of a CVX

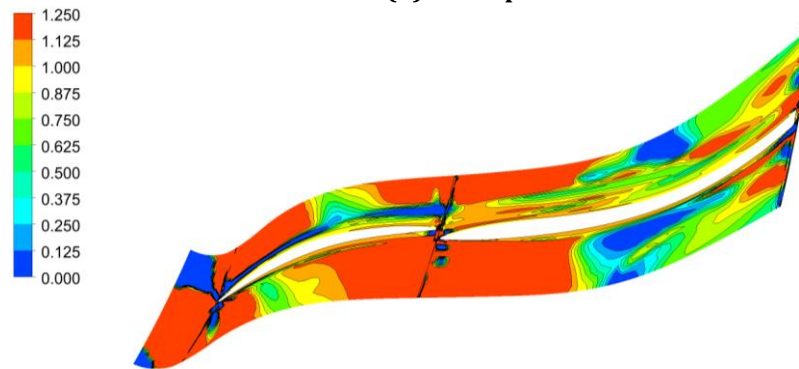
curvature (the shroud), generally indicating  $f_{r1} < 1$ . On the whole it is interesting to see the magnitude of the effect of  $f_{r1}$  on the production of TKE.



(a) 5% span



(b) 25% span



(c) 50% span

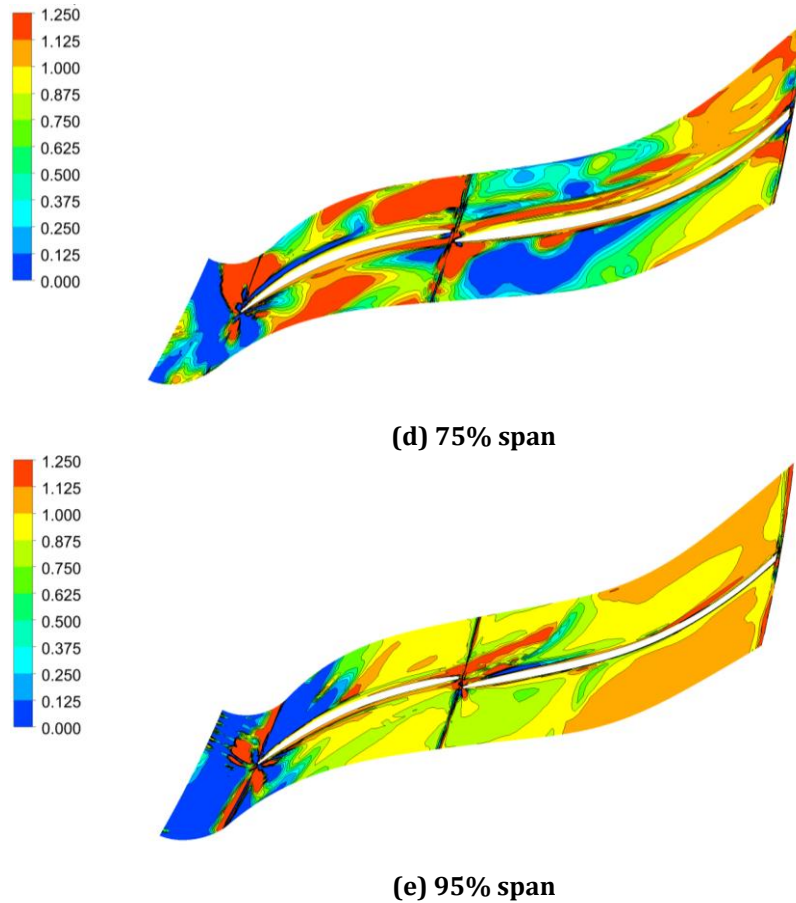


**Figure 32: Development of the  $f_{r1}$  parameter in the 307C, progressing spanwise in the impeller starting at the hub: (a) 5%, (b) 25%, (c) 50%, (d) 75% and (e) 95% span.**

Another representation of  $f_{r1}$  that is visually more relatable to the simplified geometry case is the circumferentially averaged meridional plot, shown in Figure 33. In this plot, the  $f_{r1}$  values are circumferentially averaged and then collapsed in the theta direction to produce a 2D axial-radial plane (Ansys CFX-Solver Theory Guide, Version 13.0, 2010). The 307C does not encompass the same curvature as the simplified geometry, and also has the added complexity of a split impeller, which is not accounted for in the simplified geometry. For this reason, the 307C plot is not directly compared to the simplified geometry, however it is still an interesting plot to consider from a qualitative perspective. Referring to Figure 33, it can be seen that in the 307C impeller, the curvature correction is functioning properly, predicting increased production near the concave (hub) surface particularly in the exducer region where the curvature is higher. The increased production is

represented by the  $f_{r1}$  value above 1. Furthermore, near the convex (shroud) surface in the exducer, an  $f_{r1}$  value less than 1 is predominant, with values as low as between 0.250 and 0.375. These trends are consistent with the decrease in production of TKE that is expected with a convex surface.

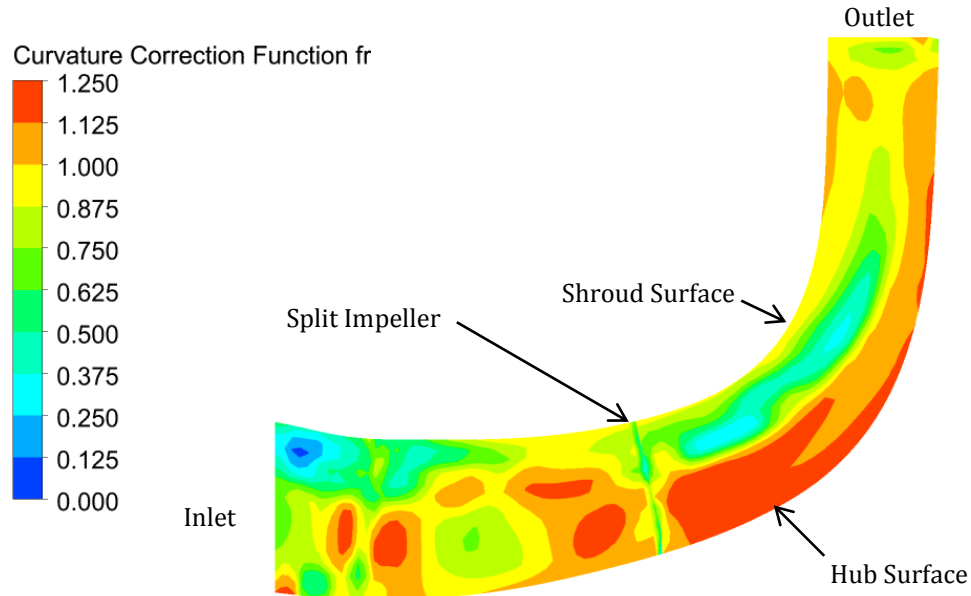


Figure 33: Meridional plot of  $f_{r1}$  (circumferentially averaged) for the 307C compressor

#### 6.4 Summary

The 307C results were discussed in detail in this chapter. The SST-CC and SST models were compared to the RSM-SSG model and experimental results in terms of global performance parameters, as well as against velocity distributions at two different locations in the compressor stage (the mixing plane and diffuser exit). Comparing speedlines, the SST-CC outperformed the SST model on the choke side, but underpredicted both the experimental data and the SST model curve near the stall side. Minor differences were found between the SST and SST-CC models at the mixing plane location. At the diffuser exit, the SST and SST-CC models each showed local deficiencies in performance as compared to experimental data. A series of plots of  $f_{r1}$  at different spanwise locations revealed trends consistent with known curvature effects: higher  $f_{r1}$  values near the concave hub and lower values near the

convex shroud. The next chapter discusses the results from the 1C compressor. The 1C case will focus on global performance parameters, as well as on comparing different curvature terms between the 1C and simplified geometry cases.

## 7. 1C COMPRESSOR RESULTS

---

The second centrifugal compressor (1C) test case is analyzed in this chapter. This analysis considers comparing the SST and SST-CC models in terms of global performance parameters, analyzing the  $f_{r1}$  term and the eddy viscosity of the 1C and the simplified geometry.

### 7.1 *Limitations of this case*

At the time of writing, experimental data have not been collected for the 1C compressor case, however, a measurement campaign is planned for LDV measurements similar to the 307C case in the near future. Therefore, this comparison is solely based on comparing the SST, SST-CC and RSM-SSG models in a relative sense as well as comparing details between the 1C compressor and the simplified geometry. Despite lacking a direct comparison with experimental data, the numerical results presented will provide an excellent framework for future research once the experiments have been completed.

### 7.2 *Global performance - PR and efficiency*

As in the 307C compressor case, the 1C compressor was also investigated in terms of global performance parameters. While a comparison cannot be made against experimental data as in the 307C compressor case, some conclusions can be made about the relative performance of the three different turbulence models.

Figure 34 presents the compressor speedline for the 1C compressor case. Comparing the SST and SST-CC models, it can be seen that both models predict a similar curve. However, the SST-CC model predicts either lower values of PR at the same mass flow (stall side) or lower values of mass flow at the same PR (choke side). On average, the SST and SST-CC predictions differ by approximately 0.60% in terms of PR. The largest differences in PR prediction appear in the central region between stall and choke, where differences are closer to 2%, and the smallest differences appear in the choke region, where the difference in predicted PR is within 0.15%. In comparison to the 307C results presented in the previous chapter,



the SST-CC models shows the same trends of a lower prediction in PR and mass flow. Thus, the relative performance of the SST-CC model as compared to the SST model is consistent across the two different compressor cases, despite having different curvatures and different impeller configurations, which is promising.

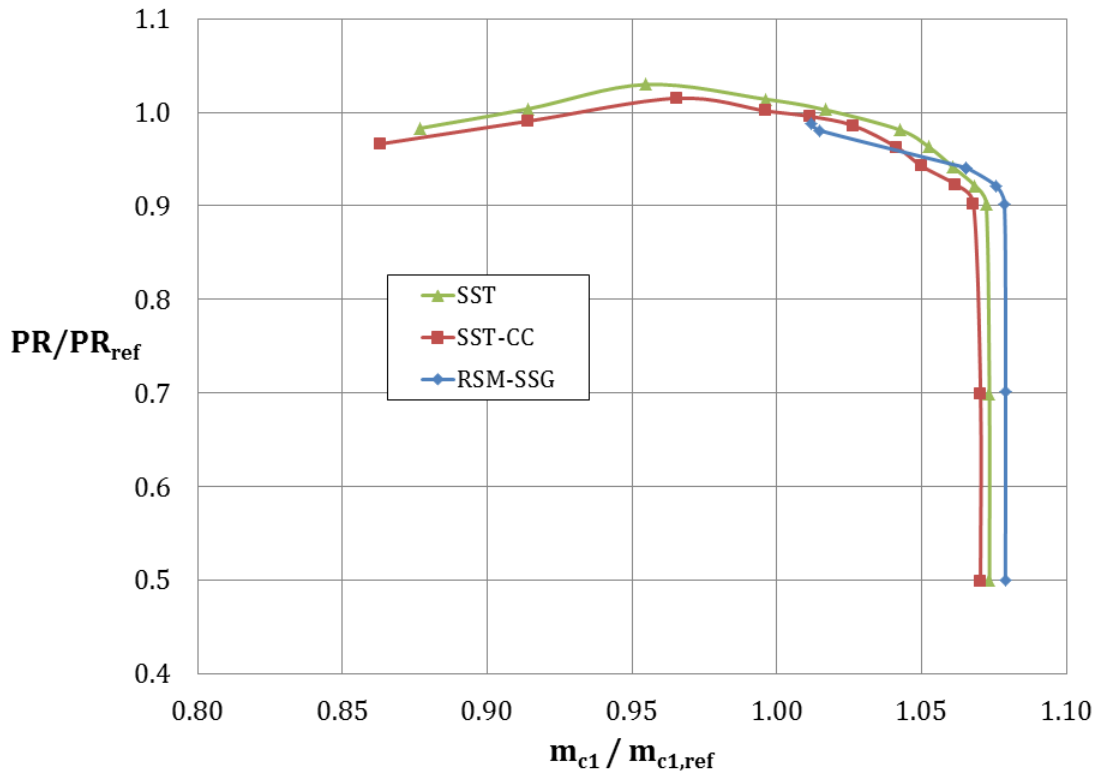


**Figure 34: 1C compressor speedline for the SST, SST-CC and RSM-SSG models at 100% design speed**

Results using the RSM-SSG model results could not be obtained further into stall, which is likely due to the numerical stiffness of the RSM-SSG model. The resulting simulations generally failed after a small number of iterations. In the choke region, the RSM-SSG model results show a small overprediction of choke mass flow relative to the SST model, only 0.5% higher than the SST model. In comparison with the difference between these two models in the 307C case (2.4%), this difference is quite small. Heading towards stall, the RSM-SSG model is closer to the SST-CC model results, which is different from what was seen in the 307C case.

Figure 35 presents the total-to-static efficiency line for the SST, SST-CC and RSM-SSG models. Again, as compared to the 307C case, the SST-CC and SST models are showing similar trends in terms of total-to-static efficiency prediction. Towards the stall side, the SST-CC and SST results start to collapse onto the same curve, and on the choke side, the difference between the choke mass flow magnitude is still prevalent. Finally, in terms of the RSM-SSG results, similar trends are seen in the total-to-static efficiency line as were discussed in the previous paragraph regarding the speedline results.

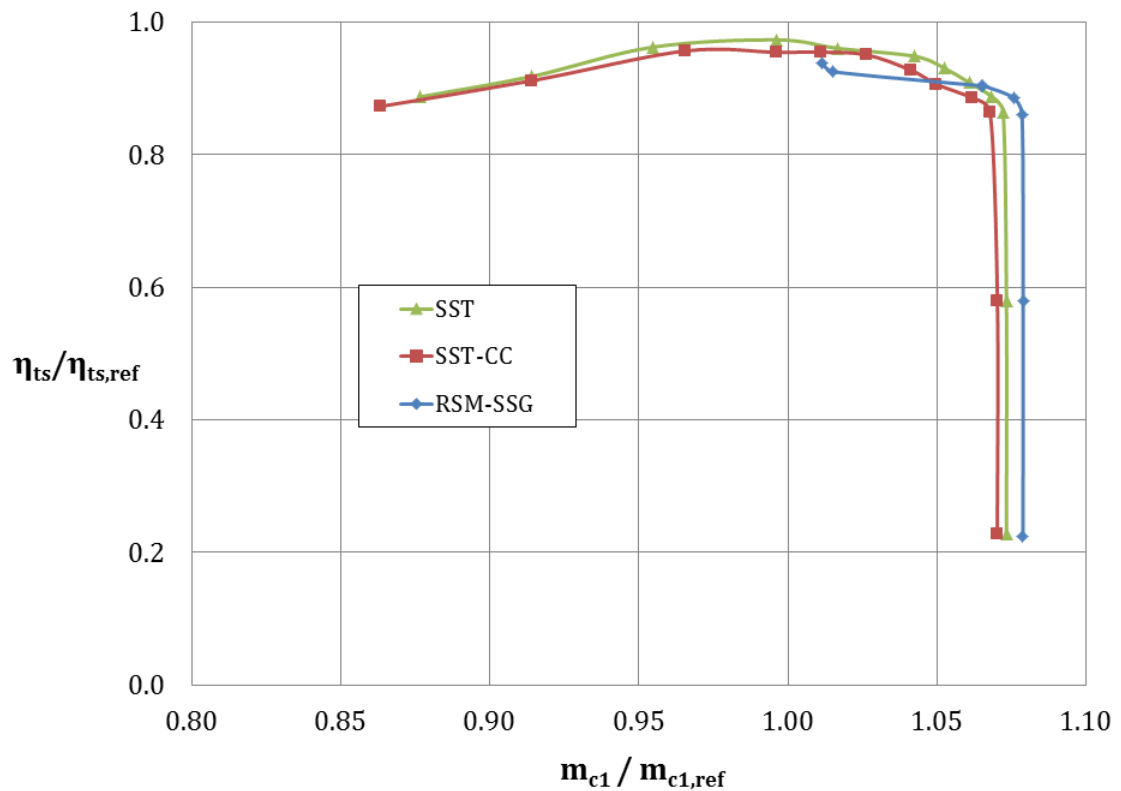


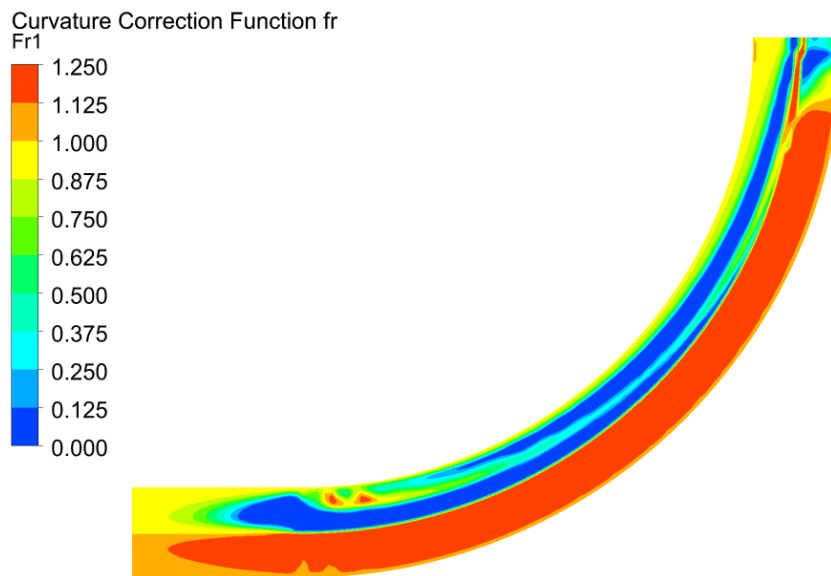
**Figure 35: 1C compressor total-to-static efficiency line for the SST, SST-CC and RSM-SSG models at 100% design speed**

Further comparisons can be made regarding the different turbulence models once the planned experiments have been completed. This will allow the SST-CC model to be thoroughly evaluated in the two compressor cases, which will reveal any consistent trends between the models as compared to experimental data.

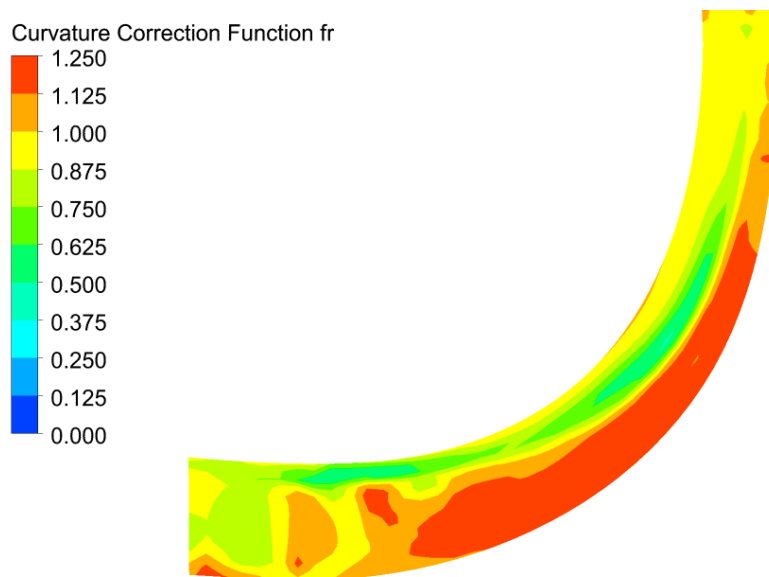
### 7.3 Investigation of the production multiplier, $f_{r1}$

In terms of the effects of curvature, it is interesting to compare the  $f_{r1}$  multiplier distribution in both the 1C and simplified geometry cases. This comparison can be used to evaluate whether or not the simplified geometry is predicting similar adaptation to curvature (with the SST-CC model) as seen in the 1C case.

Figure 36 presents contours of  $f_{r1}$  for the simplified geometry (a) and the 1C compressor (b). It should be noted that in the 1C case, the circumferential average (meridional contour) is plotted so there is a stronger resemblance between the 1C and the simplified geometry. Both of these contours qualitatively demonstrate that the curvature correction in the SST-CC model is functioning as expected; both show a large region of increased production near the concave (hub) surface, a region of decreased production near the convex (shroud) surface and a multiplier near 1 (i.e. No correction) prior to the curved section of the geometry.



(a)



(b)

**Figure 36: Contours of  $f_{r1}$  for (a) the simplified geometry and (b) the 1C compressor (meridional)**

Consider the simplified geometry case, which shows some interesting developments in  $f_{r1}$ . First, there are very sharp gradients across the centreline of the geometry. In this area, there is a rapid change from  $f_{r1} = 1.25$  to 0. Although the sharp gradient is not physically realistic in terms of curvature effects, its appearance is likely due to the change in sign of the primary velocity gradient at the centreline and the corresponding formulation of  $f_{r1}$ . Second, there is a large region near the concave side with maximum  $f_{r1}$ . This region is interesting since the limiter of 1.25 in the definition of  $f_{r1}$  clearly has a strong effect in this region.

An investigation of the 1C case (Figure 36b) reveals similar regions as in the simplified geometry case. For example, the gradients across the centreline still appear in the 1C case (as they should due to the change in curvature direction), however, contrary to the simplified case, the gradients are not nearly as sharp, and the  $f_{r1}$  minimum value is closer to 0.5 as opposed to 0 in the simplified case. Based on the comparison, it can be concluded that the simplified geometry seems to be representing the extreme case, shifting from maximum to minimum  $f_{r1}$ , whereas the

1C case exhibits a more reasonable response to curvature effects. Furthermore, the region of high  $f_{r1}$  value is also present near the concave wall in this case, however the 1C contours do not show as large of a region of max  $f_{r1}$  as is seen in the simplified geometry case. The  $f_{r1}$  profile at 50% streamwise (or 45°) shown in Figure 37 demonstrates the primary differences between the transition from concave to convex curvature at the centreline, as well as the differences between the region of large  $f_{r1}$  near the concave wall. It can be seen that both cases show the same trends in regards to curvature effects, but the simplified geometry covers the entire spectrum of  $f_{r1}$ . Again, it appears that the simplified geometry seems to accentuate the effects of  $f_{r1}$  as compared to the 1C case. Since the primary difference between the two cases is the presence or absence of rotation, it is possible that the rotation of the impeller in the 1C case can be somehow attributed to the appeared “suppression” of  $f_{r1}$ .

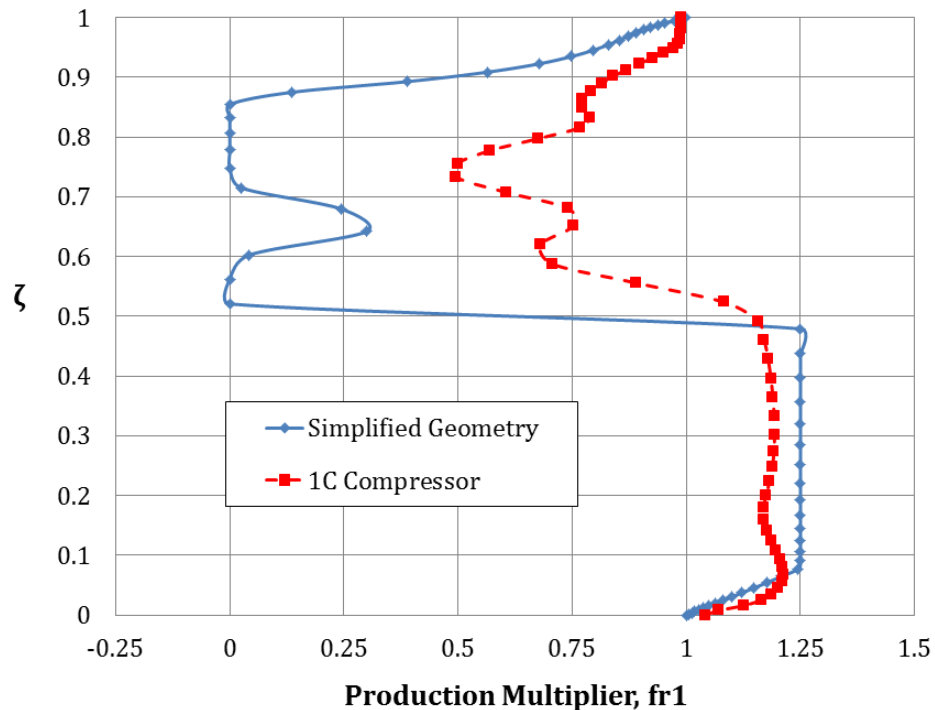


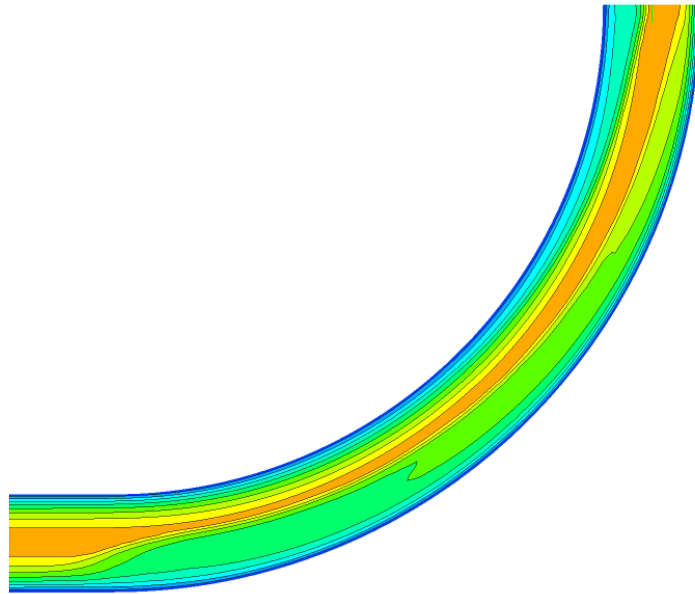
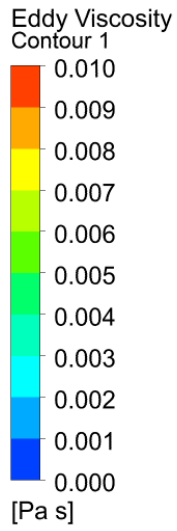
**Figure 37: Production multiplier for the simplified geometry at 45° and the 1C compressor at 50% streamwise**

Spanwise contours of  $f_{r1}$  at 5, 25, 50, 75 and 95% span were also investigated for the 1C case, as in the 307C case. These contours can be found in Appendix II, §A. Similar to what was seen in the 307C case, the 1C contours show a shift from  $f_{r1} > 1$  near the concave hub to  $f_{r1} \leq 1$  near the convex shroud. Therefore, the trends are consistent across the two compressor stages. Due to the qualitative similarities between the same contours in the 307C case, the 1C contours are not discussed in detail. For a more detailed discussion on the spanwise contours of  $f_{r1}$  in the 307C case, refer to back to §6.3.

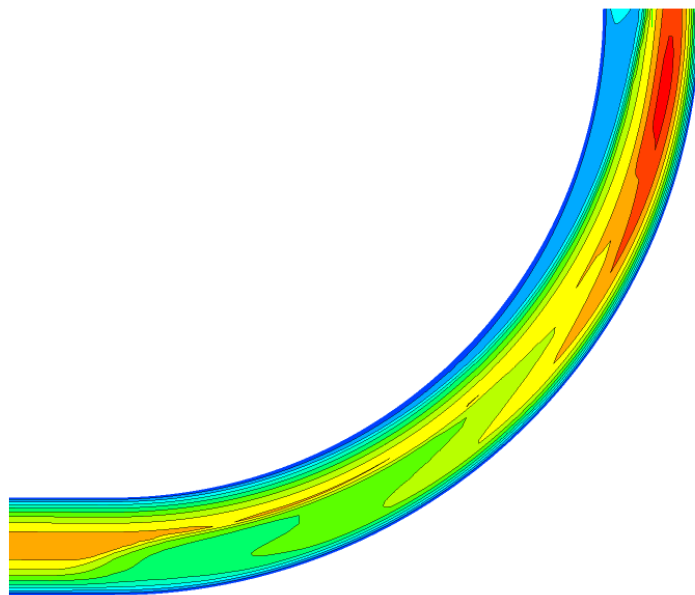
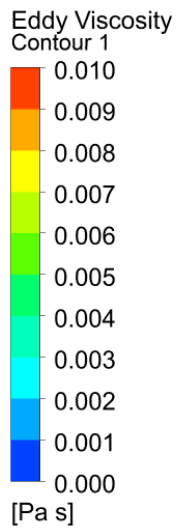
#### **7.4 Comparison of eddy viscosity**

Another evaluation of the general qualitative performance of the curvature correction is in the prediction of the eddy viscosity, as shown in Figure 38 for the simplified geometry case and Figure 39 for the 1C case. Dufour et al. (2008) also investigated the eddy viscosity, comparing it in the Radiver test case (Ziegler et al., 2003) to evaluate the SARC model. They qualitatively showed that the SARC correction was working properly in their centrifugal test case. Thus it is logical to compare the eddy viscosity distribution for the SST-CC model as well since the SARC model is the basis of the correction for the SST-CC model.

Considering the simplified geometry case first, the eddy viscosity is plotted for the SST and SST-CC models in Figure 38 (a) and (b), respectively. The SST prediction of the eddy viscosity in Figure 38a does not appear to show any sensitivity to curvature by predicting a roughly symmetric profile of eddy viscosity across the entire span (from concave to convex). Also, the maximum values of eddy viscosity are relatively constant in the near wall regions. This is contrary to the SST-CC model in Figure 38b, where it can be seen that there is a clear response to the curved walls, deduced from an increased eddy viscosity region appearing near the concave wall and a decreased eddy viscosity region near the convex wall. These local maxima and minima are especially apparent near the exit of the curved section, at  $\theta = 90^\circ$ .



(a)



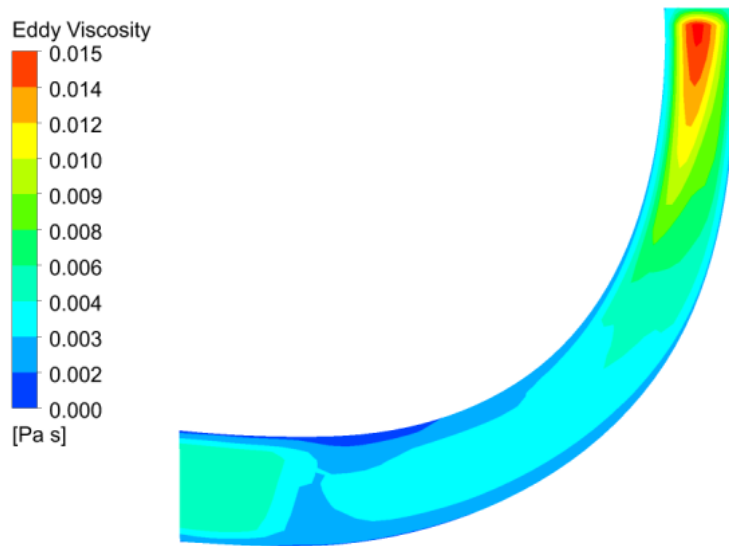
(b)

**Figure 38: Contours of eddy viscosity for the curved section of the simplified geometry. (a) SST model and (b) SST-CC model**

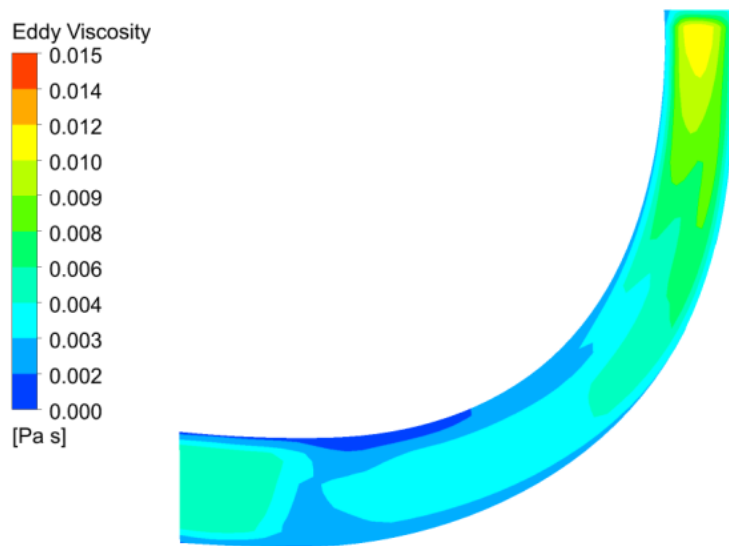
Considering the meridional contours of eddy viscosity in the 1C case (Figure 39), it can be seen that the trends and differences between the SST (a) and SST-CC (b) models are not as apparent. Observation shows that the SST model predicts a larger peak of eddy viscosity near the impeller exit as compared to the SST-CC model, with both peaks occurring near the spanwise centreline. These peaks are likely related to the rotation of the impeller, since this region should be greatly affected by the rotating blade tips. In comparison to the results obtained by Dufour et al. (2008) for the SARC model, the eddy viscosity distributions are not as weighted towards the concave and convex surfaces. In their study of the Radiver test case, they found that there was a more prominent difference between the corrected and uncorrected versions of the S-A model near the hub and shroud surfaces, showing a visible difference between the increased and decreased turbulence associated with these curvatures. In other words, the distribution they found for the SARC model was more similar to the eddy viscosity results in the simplified geometry shown in the SST-CC contour in Figure 38b.

In summary, the eddy viscosity contours for the 1C compressor did not show the same trends as in the simplified geometry or as in the comparison of the SARC model in centrifugal compressors by Dufour et al. (2008). The reasoning for the lack of sensitivity to curvature in terms of eddy viscosity in the SST-CC contour in Figure 39b is unknown, but could be further investigated.





(a)



(b)

**Figure 39: Contours of eddy viscosity for the 1C compressor (meridional contour). (a) SST model and (b) SST-CC model**

## 7.5 Summary

Results were presented for the 1C compressor case in terms of global performance parameters (speedlines and total-to-static efficiency), and in terms of a comparison

with the simplified geometry case. The production multiplier,  $f_{r1}$ , and eddy viscosity contours were compared between the 1C compressor and the simplified geometry. Similar trends were found between the two cases in the production multiplier, showing regions of increased  $f_{r1}$  near the concave (or hub) surface and regions of decreased  $f_{r1}$  near the convex (or shroud) surface. However, the simplified geometry seems to accentuate the effects of  $f_{r1}$  as compared to the compressor case. The SST-CC eddy viscosity contours were consistent in showing the appropriate effects of curvature in the simplified geometry case, however these trends were not clear in the compressor case. The following chapter discusses a further investigation into the simplified geometry to examine the differences between the SST and SST-CC models in terms of predicting mean flow fields, turbulent kinetic energy, Reynolds normal stresses and the production of turbulent kinetic energy.

## 8. SIMPLIFIED GEOMETRY INVESTIGATION

---

In this chapter, the SST-CC model is analyzed additionally from different perspectives to further examine the differences between the SST and SST-CC models in terms of flow field and, thus, curvature effects. First, the work is discussed in terms of flow and geometry parameters, as well as curvature, and how it fits in with previous work on curved duct style geometries. Second, additional plots including mean velocity, turbulence kinetic energy (TKE), Reynolds normal stress and TKE production profiles are discussed. The performance of the SST-CC model is measured relative to the RSM-SSG model, since the latter is more sensitive to curvature than the eddy viscosity based SST models. Finally, a brief discussion is made on the analysis of the different terms in the  $f_{r1}$  formulation.

Throughout this section, the vertical axis,  $\zeta$ , represents the traverse from concave (zero) to convex (unity) curvature in the geometry, and all plots were taken in the periodic boundary condition plane. Figure 40 shows a schematic of the plot locations and the coordinate system. An additional measurement location (before inlet) was added at a location upstream of the  $0^\circ$  section, once the flow was fully developed from the straight section, to show the unaffected inlet profiles into the curved section.

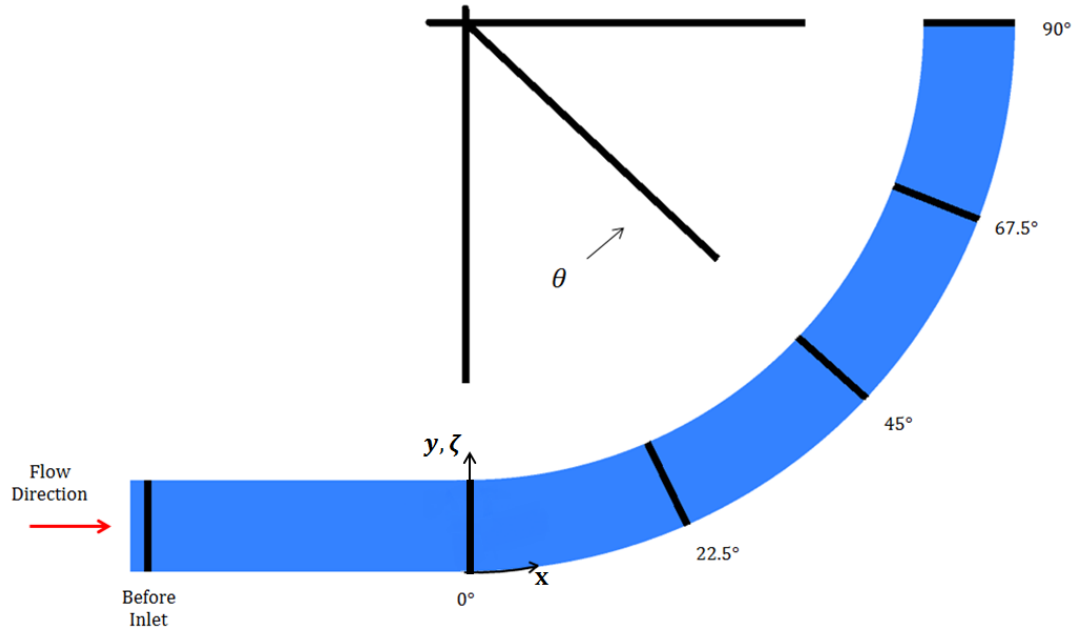


Figure 40: Schematic of the measurement locations and the coordinate system used

### 8.1 Curvature and flow parameters

The main purpose of the simplified geometry is to represent the geometry and flow conditions of the 1C compressor impeller passage as accurately as possible. However, the geometry can also be related back to previous experiments using curved ducts in Table 3 via different flow and geometry parameters to examine where the current work fits in, and the curvature can be described in terms of  $K_w \delta$ .

In terms of flow parameters, the simplified geometry was designed to have a  $Re_{D_h}$  (based on the hydraulic diameter of the inlet annulus and the mean flow velocity), that matched that of the 1C compressor impeller. This resulted in a value of a  $Re_{D_h} = 2.9 \times 10^5$  between the two cases. In terms of fitting in with the experimental work completed (shown in Table 3, §3.1.3), this corresponds to a  $Re_H$  of  $1.45 \times 10^5$ . This  $Re_H$  corresponds to roughly the midpoint of the experimental  $Re_H$ , with there still being some experimental work completed at higher  $Re_H$ . This is not a concern, since the objective of this geometry was to match the flow conditions of the 1C compressor impeller and not to investigate the effects of a higher  $Re_H$ . Finally, this case fits into the category with existing streamwise pressure gradients, since an

effort was not made to remove any pressure gradient effects. This was based on the logic that the 1C impeller has existing pressure gradients, therefore the simplified geometry should not completely eliminate them.

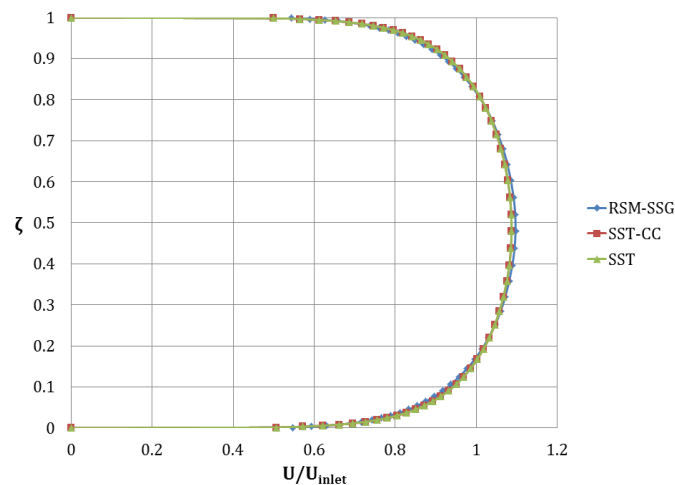
A calculation of the magnitude of curvature,  $K_w\delta$ , in the simplified geometry, based on the average radius of curvature and the height of the inlet (fully developed) boundary layer, reveals a  $K_w\delta$  value of  $\sim 0.07$ . In relation to the general scale mentioned by Patel and Sotiropoulos (1997), this is nearest to “moderate curvature”. Also recall the literature states that this scale of values is not widely accepted and the effects of curvature are larger than implied by the order of magnitude of this term (Piquet, 1999). Relative to the previous experimental work in Table 3, this value is higher than many of the cases, however there are a few experiments with higher  $K_w\delta$  (or  $\delta/R_c$ ). Despite this case being in the “moderate” curvature category and not in the “high” curvature category, there is no implication that the curvature is not strong enough to show an effect on the flow field and turbulence quantities. In fact, the following sections will show that the effects of curvature are present in this case and have a significant effect, as seen by the profiles of mean velocity and different turbulence quantities for the SST, SST-CC and RSM-SSG models.

## **8.2 Mean velocity profiles**

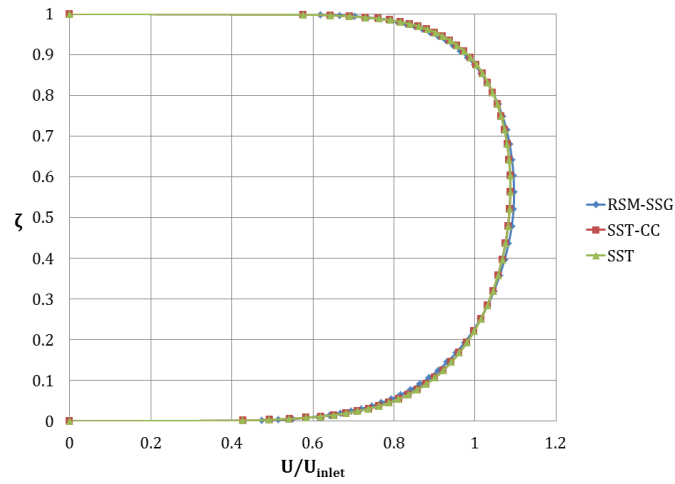
The mean velocity profiles before the inlet and from  $\theta = 0^\circ$  to  $\theta = 90^\circ$  along the curved section are shown in Figure 41. One of the first observations is that before the inlet (Figure 41a) the RSM-SSG model and the SST-based models predict the same turbulent velocity profile, corresponding to the expected profile at this  $Re$  ( $2.9 \times 10^5$ ). Moving downstream to the  $0^\circ$  and  $22.5^\circ$  locations, it can be seen that although the velocity profiles gradually become asymmetric, differences between the SST-CC and SST models are virtually non-existent. In the  $45^\circ$  plot, it can be seen that even halfway downstream, there is only a small difference between the SST and SST-CC models. Nevertheless, at  $45^\circ$ , the uncorrected and corrected SST models first begin to show differences between each other and as compared to the RSM-SSG

results. Upon reaching  $67.5^\circ$  downstream, the differences begin to be more apparent, with the SST-CC model trending towards the RSM-SSG results on both the convex and concave sides of the curved section. Near  $\zeta = 0.5$ , the three models predict roughly the same maximum velocity. At  $90^\circ$ , significant differences between the SST and SST-CC models appear throughout the entire section, with the SST-CC matching the RSM-SSG velocity more closely than the SST model. That being said, on the concave side ( $\zeta = 0$ ), fairly sizeable differences (approximately 18%) are still seen between the SST-CC and RSM-SSG models. All in all, from the velocity profiles it can be seen that the SST-CC model is predicting a mean velocity field that is closer to the RSM-SSG results, suggesting that the SST-CC model is showing an improvement over the SST model.

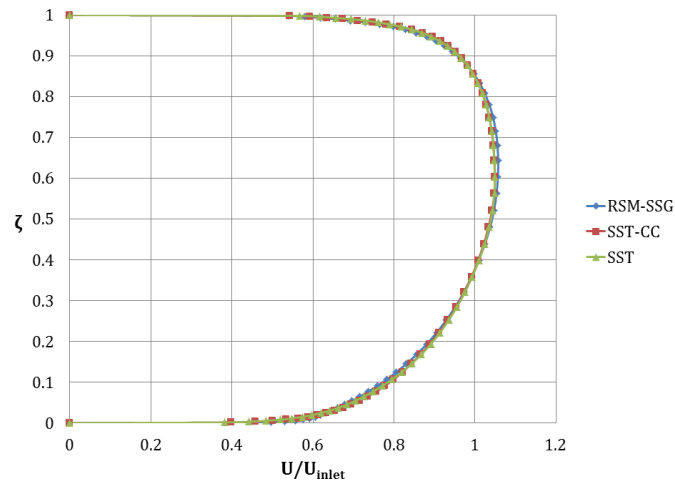
Smirnov and Menter (2009) found similar results with the SST-CC model by investigating the flow through a  $180^\circ$  curved duct geometry, and comparing velocity profiles for the SST and SST-CC models with the RSM-BSL model and experimental data. They found the same trends of the SST-CC model, showing better agreement than the SST model with the RSM-BSL curve, at the  $90^\circ$  and  $180^\circ$  locations. Nevertheless, the largest differences between the SST-CC and RSM-BSL models were still substantial, showing maximum differences near the concave wall of roughly 20%.



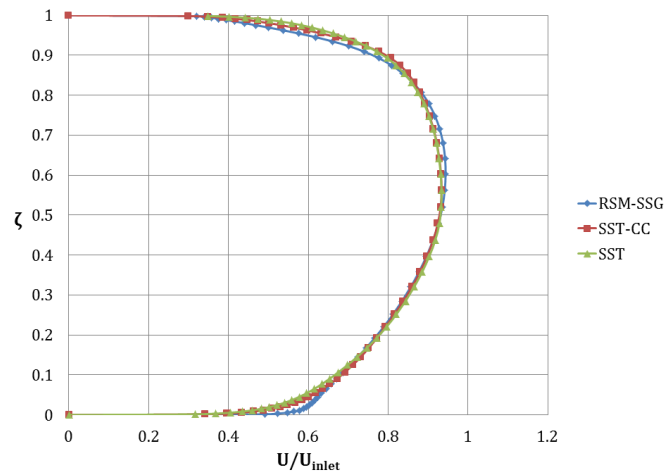
(a) Before Inlet



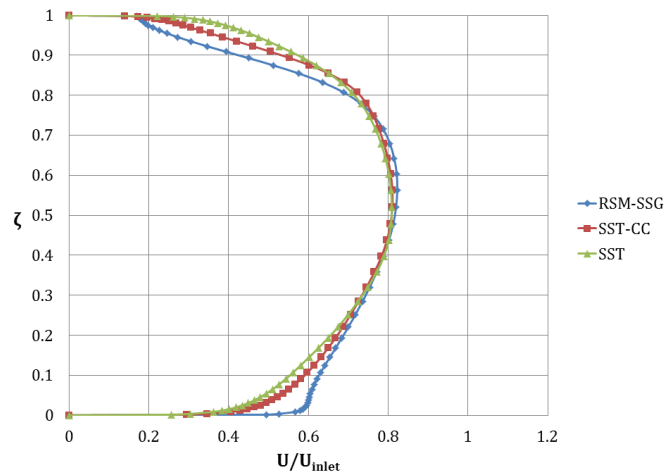
(b) 0°



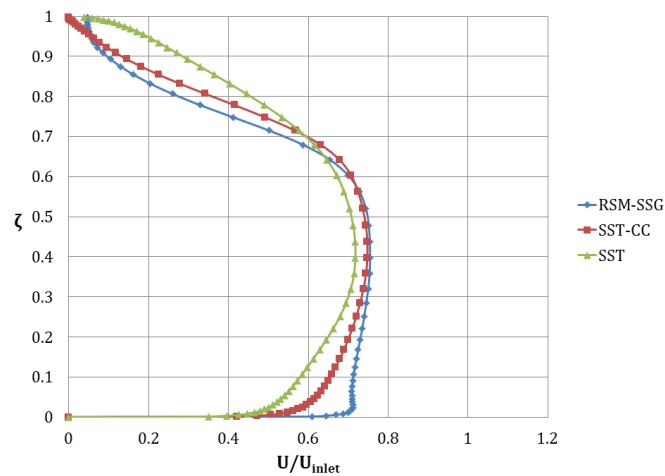
(c) 22.5°



(d) 45°



(e) 67.5°



(f) 90°

**Figure 41: Velocity profiles at different streamwise locations along the simplified geometry: (a) Before inlet, (b) 0°, (c) 22.5°, (d) 45°, (e) 67.5° and (f) 90°.**

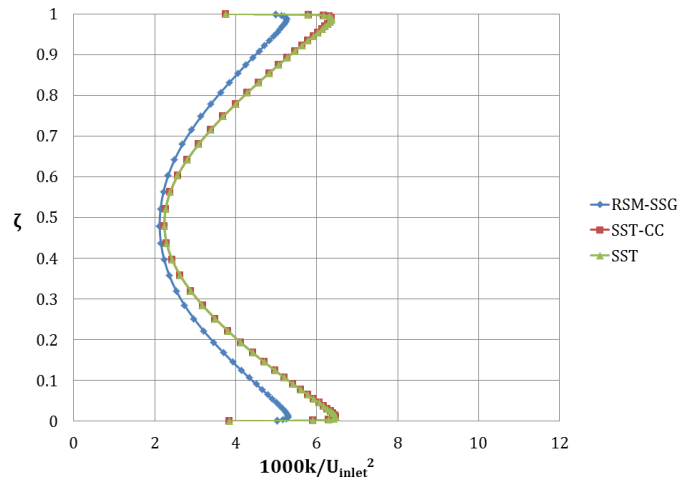
### 8.3 Turbulent kinetic energy (TKE) profiles

The TKE profiles at the same six locations are presented in Figure 42. Contrary to the velocity profiles, the TKE profiles show variation between the three models throughout the entire curved section. Starting before the curved inlet, in Figure 42(a), it can be seen that the TKE profiles are turbulent and fully symmetric, however there are differences between the RSM-SSG and SST based models in the prediction of the wall peaks, with the SST and SST-CC models overpredicting the RSM-SSG TKE curve.

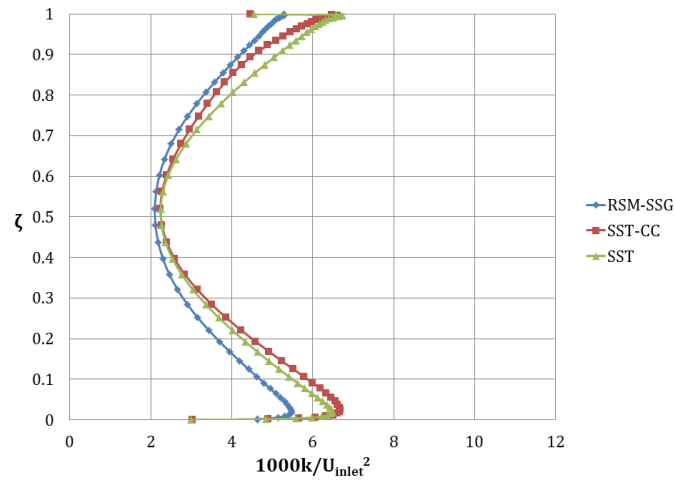


Progressing downstream to the inlet of the curved section ( $0^\circ$ ), it can be seen that asymmetry of the profiles begins to appear. At this location, the SST-CC model is predicting reduced TKE on the convex side and increased TKE on the concave side as compared to the SST model. The RSM-SSG model is still very symmetrical and does not show any effects of curvature at this location. Larger variations between the three models start to appear at  $22.5^\circ$ . It can be seen that the SST-CC model matches the RSM-SSG model very closely as opposed to the SST model, which shows larger differences throughout the profile. Both models predict the same results near the centreline of the curved section ( $\zeta = 0.5$ ). These trends continue into the  $45^\circ$  plot, where the SST-CC model matches the RSM-SSG model very well. This indicates that the SST-CC model is behaving appropriately as compared to the original SST (uncorrected) model, based on the known curvature effects that there is enhanced TKE near the concave side and suppressed TKE near the convex side (Patel & Sotiropoulos, 1997). At  $67.5^\circ$ , the SST-CC model is still behaving accordingly, based on known curvature effects, but matches much better on the concave side than on the convex side. Towards the convex side, the SST-CC qualitatively matches the shape of the RSM-SSG prediction, but quantitatively, the SST model predicts a curve closer to the RSM-SSG results, whereas the SST-CC model underpredicts the RSM-SSG results. Finally, in the  $90^\circ$  plot, the SST-CC model is reacting to the curvature accordingly by showing the same trends as in the previous locations, however the differences are not as drastic. In fact the SST-CC and SST models predict nearly the same TKE profile. The RSM-SSG model is predicting a very high peak towards the convex side, which may be due to the onset of recirculating flow in this region.

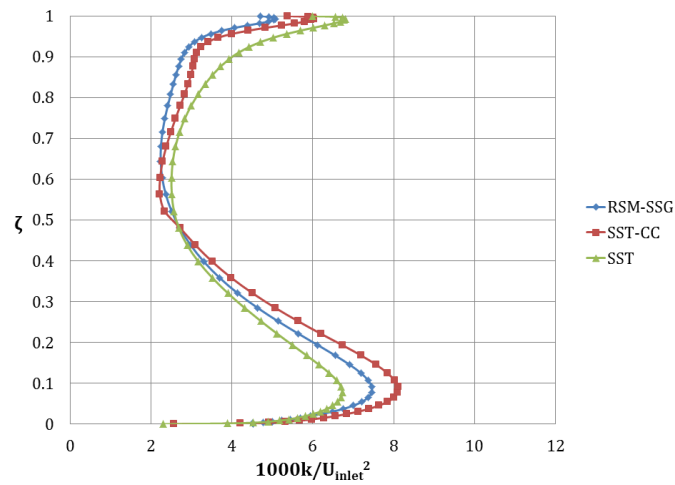
Overall, the SST-CC model shows promising results, effectively predicting the appropriate effects of curvature and matching well with the RSM-SSG results in most cases.



(a) Before inlet



(b)  $0^\circ$



(c)  $22.5^\circ$

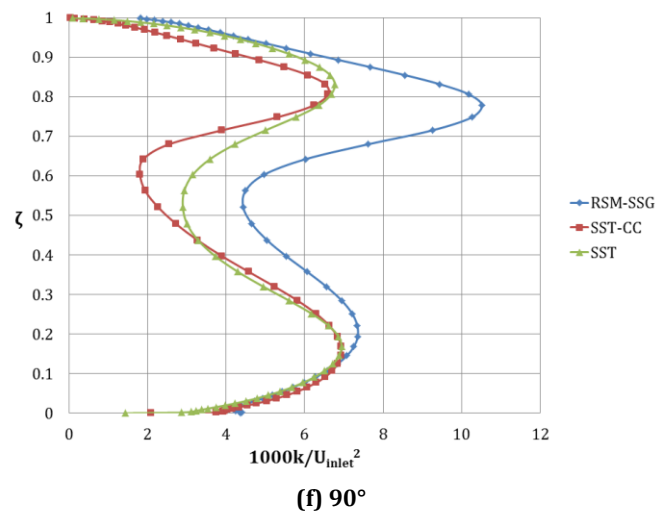
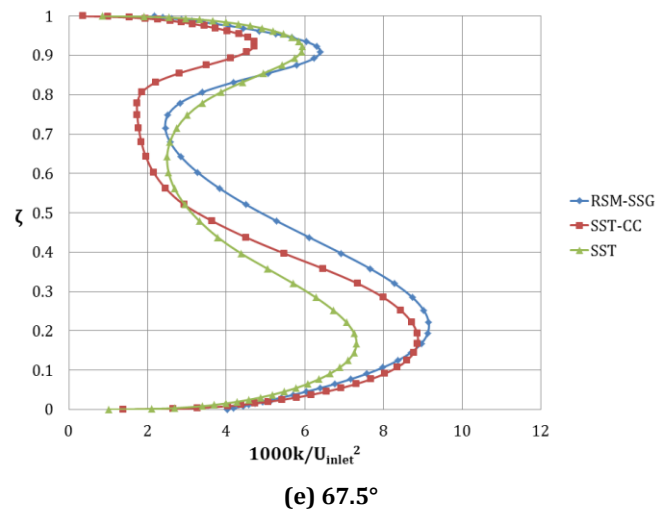
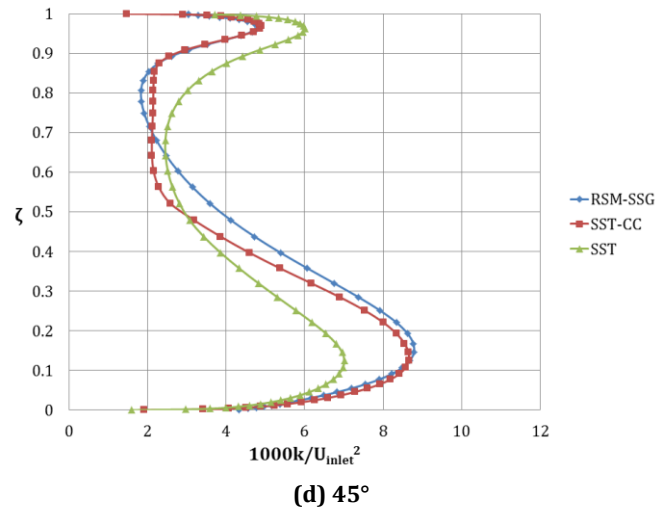


Figure 42: TKE profiles at different streamwise locations along the simplified geometry

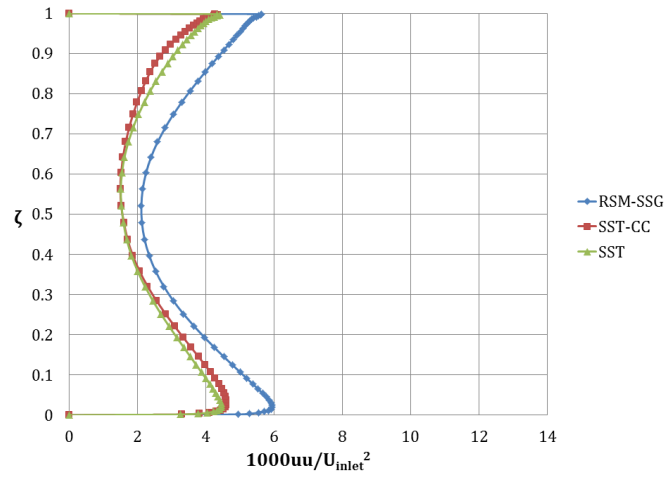
#### 8.4 Reynolds normal stresses

Eddy viscosity models, such as the SST model, assume local isotropy of the turbulent length scale and for this reason are known to perform poorly in flows with sudden changes in the mean strain rate, or when the flow and strain principal axes are not aligned, for example in flows with streamline curvature. The RSM-SSG model does not suffer from this problem because it does not make the local isotropy assumption. The poor performance in eddy viscosity models is particularly apparent in the Reynolds normal stresses (Wilcox, 2006, p. 304). An investigation of the three Reynolds normal stresses has revealed different trends in both the in-plane ( $\overline{uu}$  and  $\overline{vv}$ ) and out-of-plane ( $\overline{ww}$ ) directions. The following paragraphs will first discuss a comparison between the SST and SST-CC models, and then a comparison is made between the SST-CC and RSM-SSG models. For the plots of the Reynolds normal stresses (absolute value) for  $0 - 90^\circ$ , refer to Figures 43, 44 and 45 for the Reynolds  $\overline{uu}$ ,  $\overline{vv}$  and  $\overline{ww}$  stresses, respectively. The Reynolds normal stresses before the inlet are not included in this comparison.

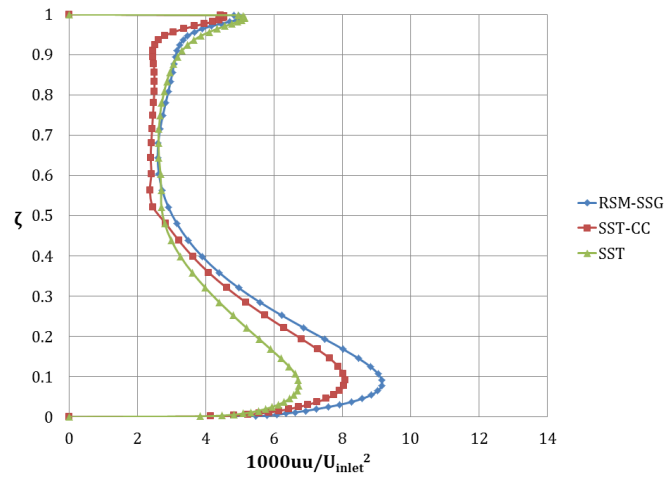
In all of the investigated locations ( $0^\circ$  to  $90^\circ$ ), there were differences between the SST and SST-CC model predictions. The SST-CC model predictions were consistent with documented curvature effects, showing an increase in turbulent stresses near the concave side and a corresponding decrease on the convex side as compared to the SST model. This trend was present in both the in-plane and out-of-plane Reynolds normal stresses. It is also noteworthy that at the centre of the geometry ( $\zeta = 0.5$ ), the SST and SST-CC models matched well, suggesting that there is no curvature correction occurring here. On average, the SST-CC model showed an equal or better agreement than the SST model as compared to the RSM-SSG model for the in-plane normal stresses ( $\overline{uu}$  and  $\overline{vv}$ ); however, the SST-CC model performed poorly on the concave side of the section in predicting the  $\overline{ww}$  stresses, with the SST model being closer to the RSM-SSG results in all cases from  $0^\circ$  to  $90^\circ$ .

A comparison of the SST-CC and RSM-SSG results revealed different trends in the  $\overline{uu}$ ,  $\overline{vv}$  and  $\overline{ww}$  stresses. First, in the primary in-plane direction (x), the  $\overline{uu}$  normal

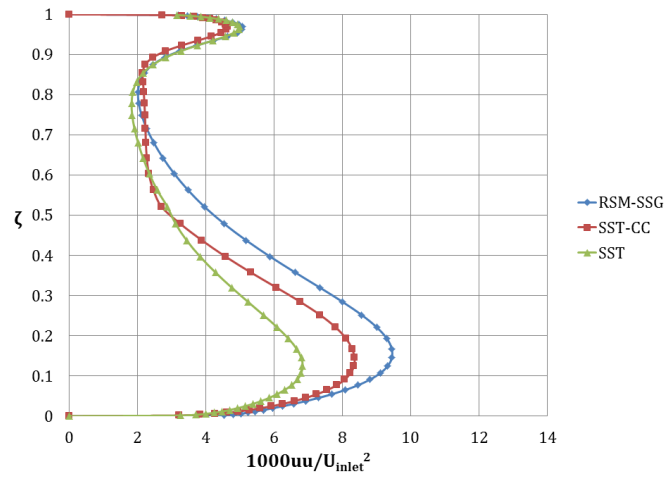
stress was underpredicted as compared to the RSM-SSG model at all locations. At  $90^\circ$  in particular, unusual results appeared for the RSM-SSG model, showing a large peak in  $uu$  on the convex side, which is clearly responsible for the same large peak on the TKE plot in Figure 42f. The SST-CC and SST models predicted a peak that is approximately 80% smaller than the RSM-SSG peak. In terms of the flow field, this is a low momentum region and, thus, an onset of separation is possible, as described in the previous section, which could be causing the overly large RSM-SSG peak. Considering the second in-plane direction ( $y$ ), no clear trends were observed in the  $\overline{v'v'}$  stress when progressing from  $0^\circ$  to  $90^\circ$ . In general, the  $\overline{v'v'}$  stress tended to be overpredicted as compared to the RSM-SSG model on the convex side, however this did not occur at  $67.5^\circ$ . The same can be said about the concave side, where the majority of the locations showed an underprediction as compared to the RSM-SSG results, however at  $0^\circ$ , the SST-CC model shows a large overprediction. In the out-of-plane direction ( $z$ ), trends in  $\overline{w'w'}$  stress were seen towards the concave and convex sides of the domain. The concave side showed a consistent overprediction of  $\overline{w'w'}$  stress from the SST-CC model as compared to the RSM-SSG model. The convex side on the other hand showed a gradual change from overprediction to underprediction of the RSM-SSG results. From  $0^\circ$  to  $45^\circ$ , the  $\overline{w'w'}$  stress was overpredicted, however the magnitude of the overprediction reduces, progressing downstream. At  $67.5^\circ$ , the SST-CC model slightly underpredicted the RSM-SSG results and finally at  $90^\circ$ , the  $\overline{w'w'}$  stress is underpredicted. Considering this trend in  $\overline{w'w'}$ , it is apparent that the  $\overline{w'w'}$  stress is transitioning from the convex to concave side of the curved section. This would indicate an increase in turbulent stress on the concave side and a decrease on the convex side, which would be consistent with known curvature effects.



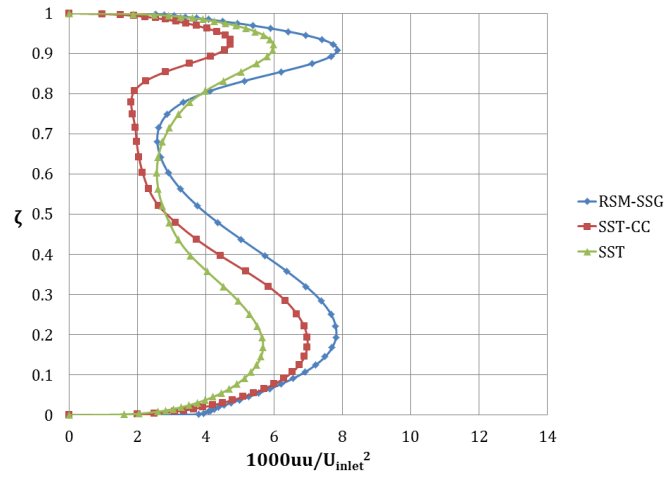
(a) 0°



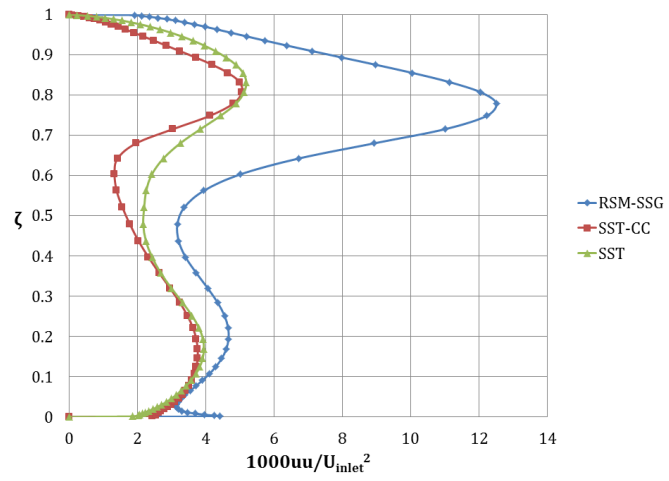
(b) 22.5°



(c) 45°

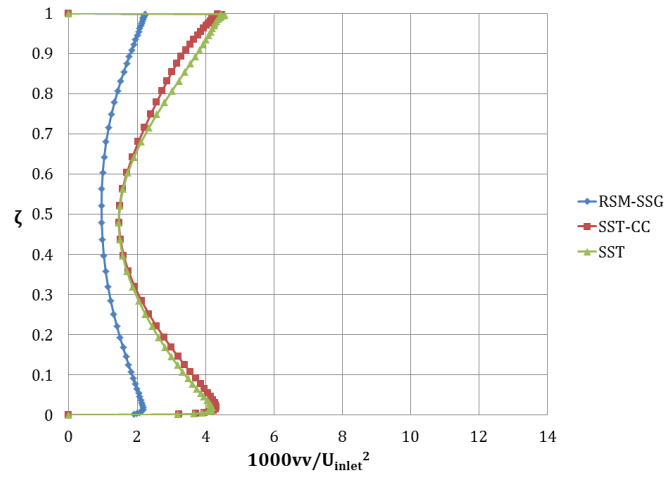


(d) 67.5°

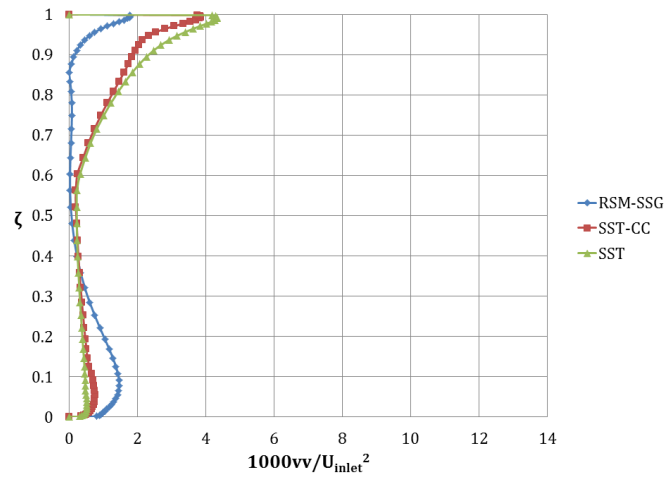


(e) 90°

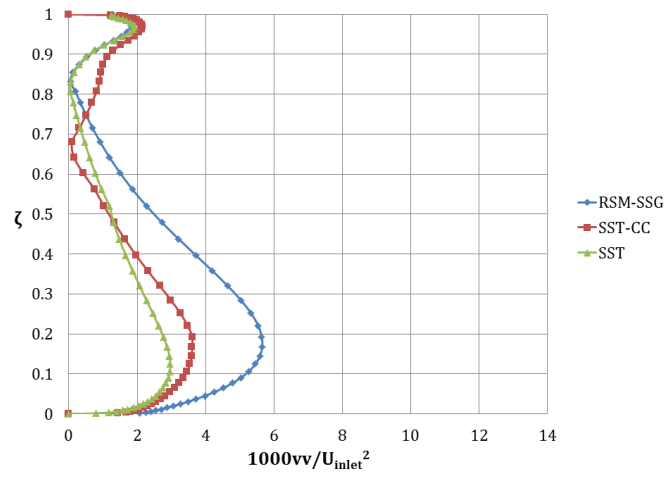
Figure 43: Reynolds  $\overline{uu}$  normal stress for 0 - 90° in the simplified geometry



(a)  $0^\circ$

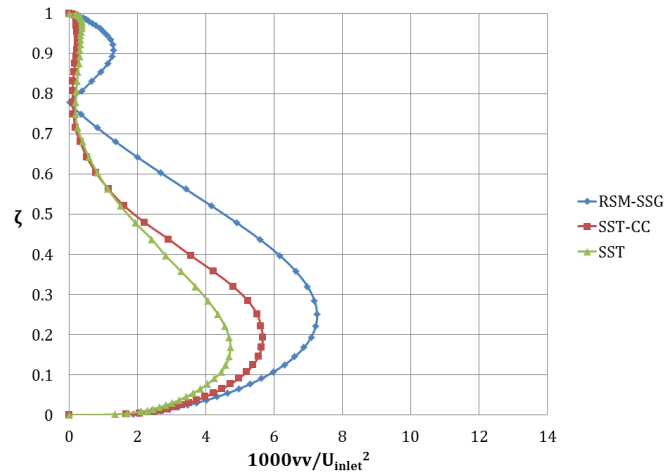


(b)  $22.5^\circ$

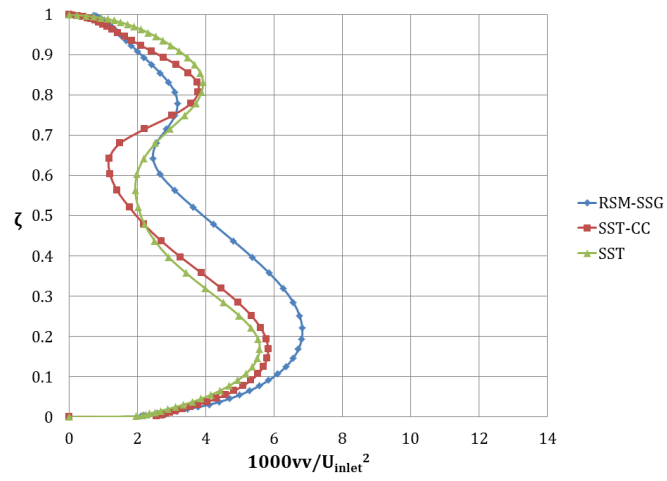


(c)  $45^\circ$



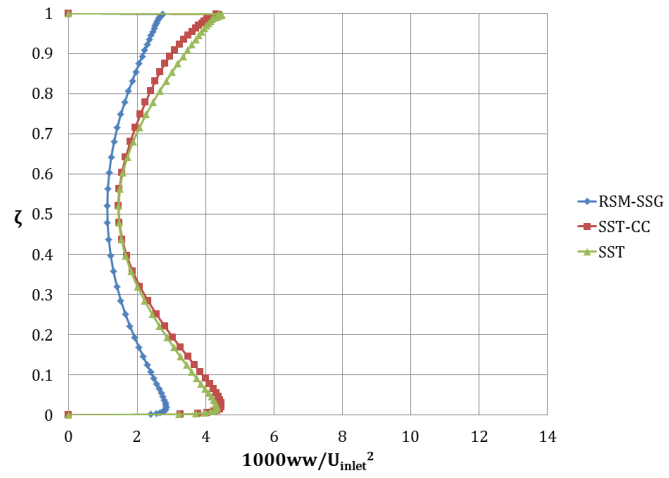


(d)  $67.5^\circ$

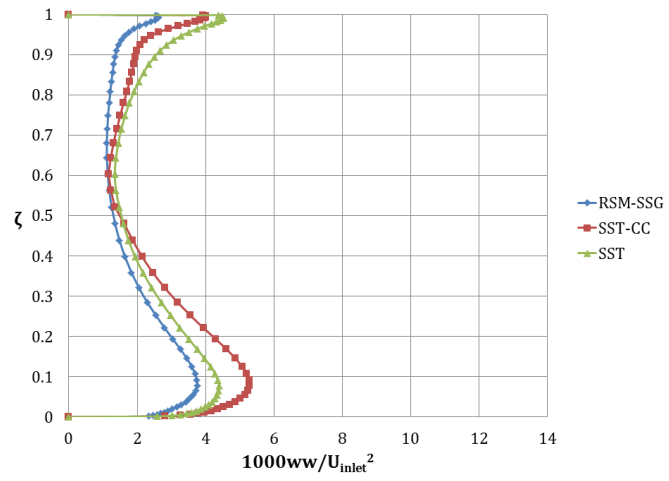


(e)  $90^\circ$

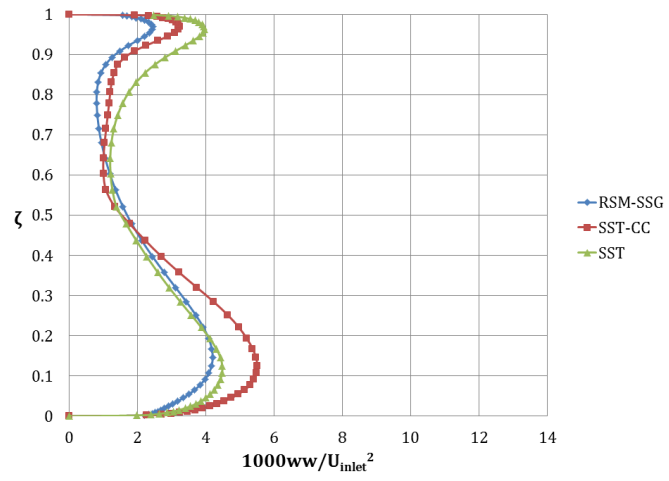
Figure 44: Reynolds  $\overline{v'v'}$  normal stress for  $0 - 90^\circ$  in the simplified geometry



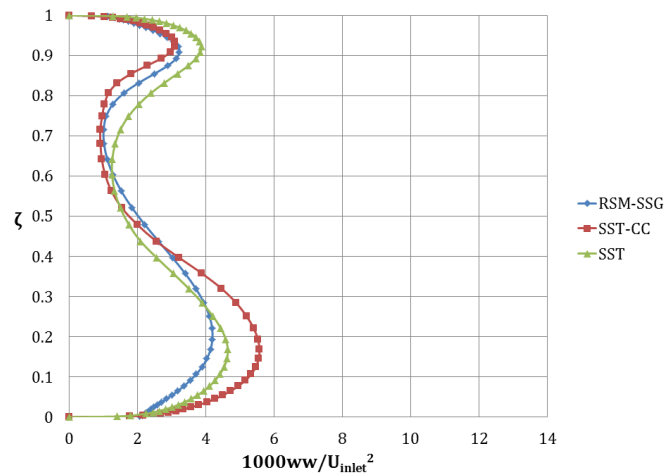
(a)  $0^\circ$



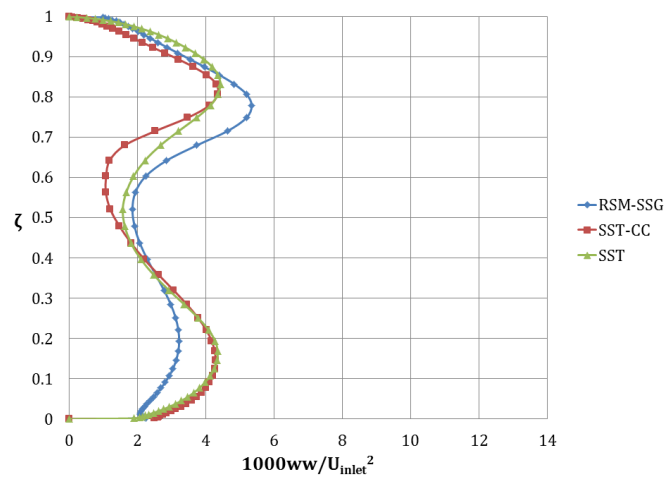
(b)  $22.5^\circ$



(c)  $45^\circ$



(d) 67.5°



(e) 90°

**Figure 45: Reynolds  $\overline{ww}$  normal stress for 0 – 90° in the simplified geometry**

In general, the SST-CC model performed well, showing higher stresses near the concave side and lower stresses near the convex side, relative to the SST model. Thus, overall, the SST-CC model is predicting the correct trends in Reynolds stresses due to curvature effects as compared to the SST model, which suggests an improvement with the curvature correction addition. Relative to the RSM-SSG model, the SST-CC models shows some trends in both the in-plane and out-of-plane Reynolds stresses, however there were no obvious trends with the  $\overline{vv}$  stress.

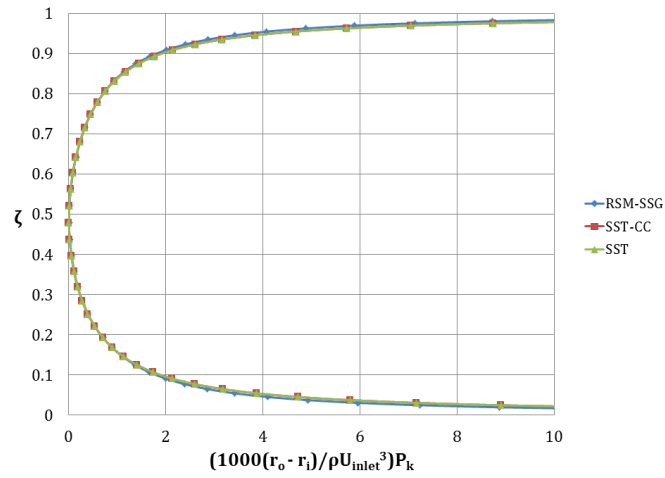
### 8.5 Production of TKE Profiles

As stated previously, the difference between the SST-CC and SST models is the multiplier ( $f_{r1}$ ) of the turbulence kinetic energy production term,  $P_k$  (Eq. 8.1), in the SST-CC model equations. For this reason, it is interesting to investigate the differences between  $P_k$  at different streamwise locations in the geometry.

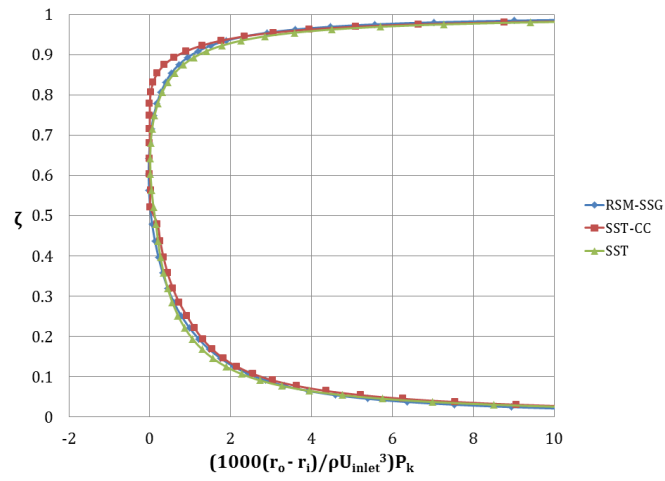
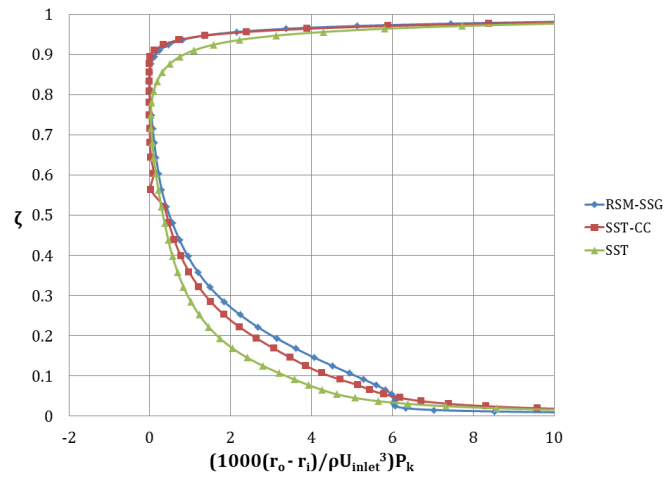
$$P_k = -\rho \overline{u_i u_j} \frac{\partial U_i}{\partial x_j} \quad (8.1)$$

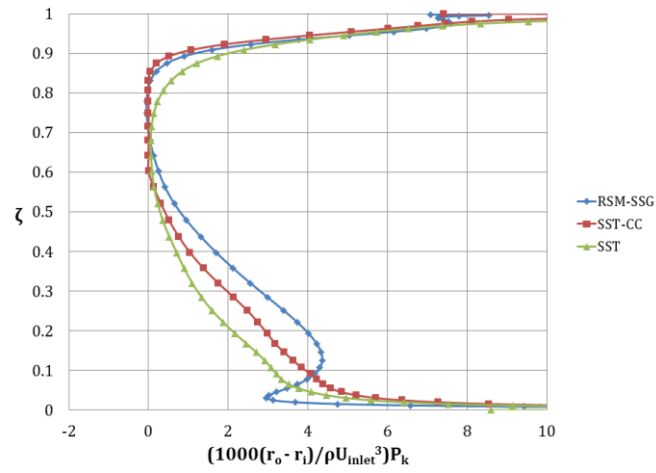
Figure 46 presents a comparison of  $P_k$  in the SST and SST-CC models, relative to the RSM-SSG model. Notice that in the SST-CC model, the curve plotted is  $f_{r1}P_k$ , since this represents the “full” production term, whereas in the SST and RSM-SSG cases, the “full” production term is simply  $P_k$ . Also, these plots are limited by the scale to show the differences in the central region, since the wall peaks show much larger values.

Starting before the inlet (a), all three models predicted symmetric profiles, as expected since this is simply a fully developed duct flow. Overall, from that section progressing towards the 90° exit, similar trends are seen between the models. From 0° (b) to 45° (d), the SST-CC model showed increased turbulence production near the concave side and decreased turbulence production near the convex side, relative to the SST model. This corresponds to  $f_{r1}$  values greater than 1 near the concave side and less than 1 near the convex side, as was seen in the comparison with the 1C results in §7.3. The RSM-SSG model also showed a resulting sensitivity to curvature and matches well with the SST-CC curve. At 67.5° (e), the SST-CC model still showed the same trends relative to the SST model, however it underpredicts the peak on the convex side. This is consistent with what was seen in the in-plane normal stresses as discussed in the previous section. Finally, at 90° (f), the same large peak was found in the RSM-SSG results, which greatly overpredicts the SST and SST-CC models. Also at 90°, the SST-CC predicts the opposite trends with respect to curvature, the reasoning for which requires further investigation.

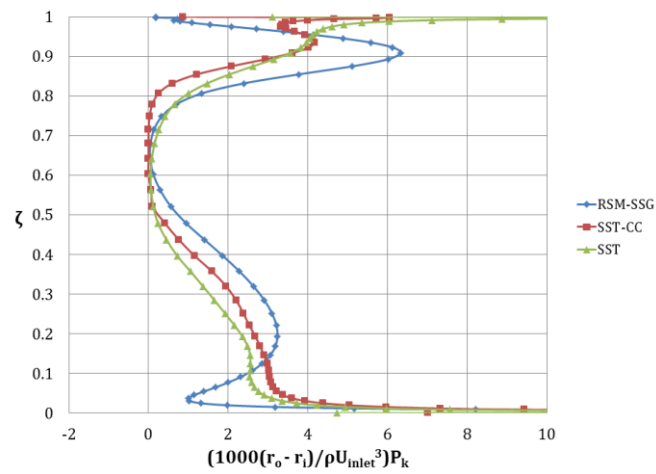


(a) Before inlet

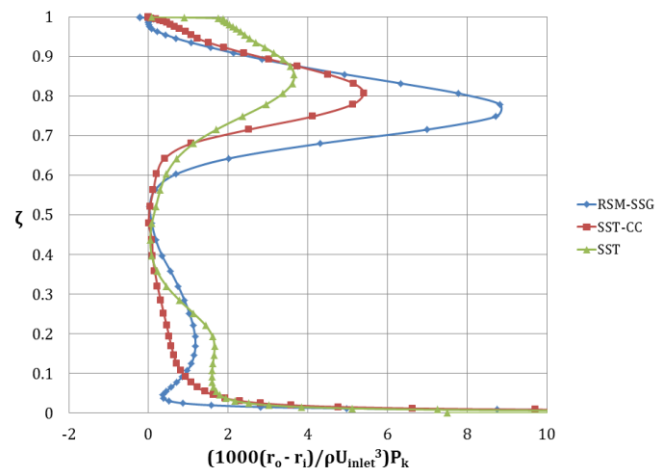
(b)  $0^\circ$ (c)  $22.5^\circ$



(d) 45°



(e) 67.5°



(f) 90°

Figure 46: Normalized TKE production at streamwise locations along the simplified geometry

### 8.6 Analysis of the $f_{r1}$ formulation

The inclusion of the production multiplier,  $f_{r1}$ , in the  $k$  and  $\omega$  transport equations in the SST-CC model is the only factor that separates the SST-CC model from the original SST. For convenience, the equations that outline the formulation of  $f_{r1}$  (Eqs. 3.33 - 3.41 from §3.2.1.4) are repeated here, renumbered as Eqs. 8.2 – 8.10. Since the final formulation of  $f_{r1}$  (Eq. 8.2) simply incorporates the limiter of 1.25 and prevents negative values of  $f_{r1}$ , consider the formulation of  $f_{rotation}$  (Eq. 8.3).  $f_{rotation}$  is based on two separate terms,  $r^*$  and  $\tilde{r}$  (Eqs. 8.4 and 8.9), both of which are primarily based on the strain rate tensor and the rotation rate tensor. An analysis of the formulation of the different terms in the  $f_{rotation}$  provides some insight on the behaviour of the  $f_{r1}$  term, as seen in the contour of  $f_{r1}$  in the simplified geometry in Figure 47. Note that this same image is seen in Figure 36(a), however it is reproduced here for reader convenience.

$$f_{r1} = \max(\min(f_{rotation}, 1.25), 0.0) \quad (8.2)$$

$$f_{rotation} = (1 + c_{r1}) \frac{2r^*}{1 + r^*} (1 - c_{r3} \tan^{-1}(c_{r2}\tilde{r})) - c_{r1} \quad (8.3)$$

$$r^* = \frac{S}{\Omega} \quad (8.4)$$

$$S = \sqrt{2S_{ij}S_{ij}} \quad (8.5)$$

$$\Omega = \sqrt{2\Omega_{ij}\Omega_{ij}} \quad (8.6)$$

$$S_{ij} = \frac{1}{2} \left( \frac{\partial U_i}{\partial x_j} + \frac{\partial U_j}{\partial x_i} \right) \quad (8.7)$$

$$\Omega_{ij} = \frac{1}{2} \left( \frac{\partial U_i}{\partial x_j} - \frac{\partial U_j}{\partial x_i} \right) + 2\epsilon_{mji} \Omega_m^{rot} \quad (8.8)$$

$$\tilde{r} = 2\Omega_{ik} S_{jk} \left[ \frac{DS_{ij}}{Dt} + (\epsilon_{imn} S_{jn} + \epsilon_{jmn} S_{in}) \Omega_m^{rot} \right] \frac{1}{\Omega D^3} \quad (8.9)$$

$$D^2 = \max(S^2, 0.09\omega^2) \quad (8.10)$$

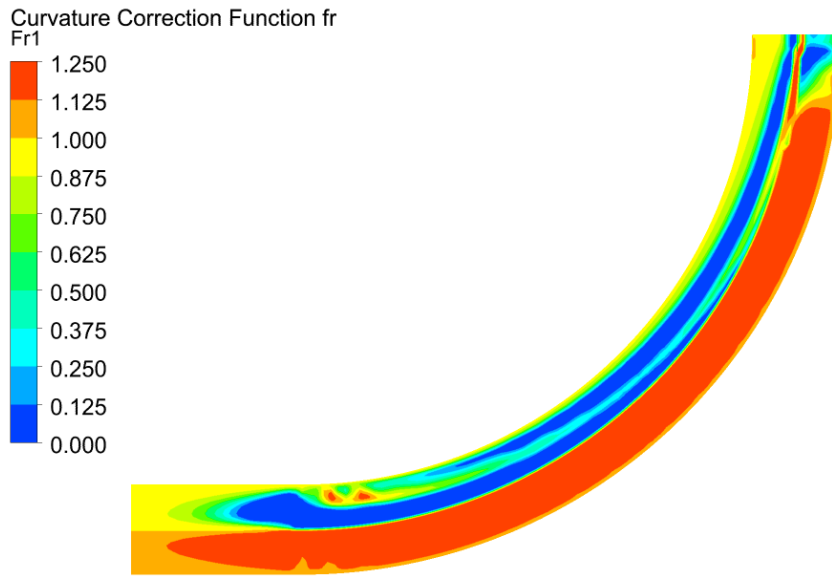


**Figure 47: Contour of  $f_{r1}$  in the simplified geometry**

One development in  $f_{r1}$  that could be explained by its formulation is the rapid transition from  $f_{r1} = 1.25$  to  $f_{r1} = 0$  at the centerline of the curved section. Conceptually this switch makes sense, since at the centerline, the flow will either be closer to the concave or convex walls, and should be corrected accordingly. However, in terms of flow field, one would expect a more gradual transition from concave to convex correction, as opposed to this almost step function appearance. At the centreline, the primary velocity gradients ( $\partial U/\partial y$  and  $\partial V/\partial x$ ) switch from positive to negative, thus creating a location of zero gradient. This means that near the centreline, both the magnitude of the strain rate tensor ( $S$ , Eq. 8.4) and the



magnitude of the rotation rate tensor ( $\Omega$ , Eq. 8.5) become very small values. Therefore, the ratio of  $S/\Omega$  (or  $r^*$ , Eq. 8.3) becomes a ratio of two small values, which makes  $f_{r1}$  very sensitive in this region. This sensitivity could be attributed to the rapid change in  $f_{r1}$ .

A full investigation of the different terms in the  $f_{r1}$  formulation, including an investigation of the  $\tilde{r}$  term has not been completed at the time of submission of this thesis, and thus the discussion is limited to the above.

### **8.7 Summary**

The simplified geometry was related back to past work on curved ducts, in terms of curvature magnitude, Reynolds number and streamwise pressure gradients. The simulations were analyzed further by considering streamwise velocity, TKE, Reynolds normal stresses and the TKE production from  $0 - 90^\circ$ , and before the inlet to the curved section. The evaluation of the SST-CC model was based on a comparison with the RSM-SSG model, which has an increased sensitivity to curvature. In general, the SST-CC model trends towards the RSM-SSG model curve for the mean velocity and TKE profiles. The SST-CC model showed the appropriate increase and decrease of TKE near concave and convex surfaces (Patel & Sotiropoulos, 1997). In terms of normal stresses, different trends were found for different Reynolds normal stress components, but no obvious trends were found with the  $\overline{v'v'}$  stress. The SST-CC matches the RSM-SSG model well in the  $\overline{u'u'}$  and  $\overline{v'v'}$  components, but poorly in the  $\overline{w'w'}$  component, especially on the convex side. The  $\overline{w'w'}$  stresses seem to shift from the convex to concave side of the curved section. The production of TKE profiles demonstrated the same trends as the TKE, showing the appropriate sensitivity to curvature and matching well with the RSM-SSG, except at  $90^\circ$  where the RSM-SSG model shows a large peak near the convex side. The rapid transition of  $f_{r1}$  at the centerline is likely attributed to a division of small values, and thus a sensitivity of  $f_{r1}$  in this region. The next chapter discusses the overall conclusions of this work.

## 9. CONCLUSIONS

---

The current work investigated the effects of curvature in terms of numerical modelling for three test cases, consisting of two centrifugal compressor stages and a simplified geometry, to improve the understanding of the flow physics associated with curvature and the effectiveness of a curvature corrected turbulence model in predicting curvature. The following observations and conclusions were made.

The effects of curvature are dependent on many factors including the curvature magnitude and directionality, as well as the Reynolds number and the presence of streamwise pressure gradients. Many researchers have investigated these effects both experimentally and numerically using simplified cases such as curved ducts. The experimental studies primarily focus on the physical mechanisms behind curvature, whereas the numerical studies tend to focus on the testing and development of turbulence models. More recently, researchers have investigated the formation of “curvature corrected” turbulence models, which use different methods to account for known curvature effects. One of these such models is the SST-CC model developed by Smirnov and Menter (2009), which uses a production multiplier to either increase or decrease the production of TKE dependent on the mean flow strain rate tensor, vorticity tensor and other factors. This model has been shown to perform well in predicting some global characteristics in a centrifugal compressor test case, however the researchers did not go into detail to characterize the flow field and describe where and how the curvature correction is accounting for curvature effects. Therefore, this work completed that task by investigating the performance and functionality of the SST-CC model in two centrifugal compressors stages, and a simplified geometry based on a centrifugal impeller passage.

The three geometries considered were the 307C compressor, the 1C compressor and a simplified geometry. Both compressors were designed by P&WC and had similar geometries, with the 1C representing a more compact stage. The simplified

geometry was a curved section with flow characteristics and curvature similar to that of the 1C compressor.

In the first (307C) compressor stage the SST-CC, SST and RSM-SSG models were compared with available experimental data in terms of global performance and flow field prediction. In the speedline and efficiency line, the SST-CC model predicted the choke region within 0.15% of the experimental data, showing an improvement over the SST model, which overpredicted the choke mass flow by 0.47%. Towards the stall side of the speedline, both models underpredicted the experimental data, the SST by 1.9% and the SST-CC by 3.1%. This discrepancy was not found towards the stall side of the efficiency line, where both models matched the experimental data well. In terms of flow field comparison, minor differences were found between the SST-CC and SST models, with each of the models showing local deficiencies relative to the experimental data. The 307C results were also qualitatively evaluated in terms of the distribution of the production multiplier. Spanwise contours of  $f_{r1}$  revealed that the SST-CC model was appropriately predicting the effects of curvature, showing a value of  $f_{r1}$  above unity near the concave hub (increased turbulence production), which gradually decreased to values of  $f_{r1}$  below unity near the convex shroud (decreased turbulence production).

In the second (1C) compressor stage, experimental data was unavailable for comparison and thus the SST-CC model was evaluated using a comparison between the 1C geometry and the simplified geometry (based on the 1C). This, in turn, also evaluated the effectiveness of the simplified geometry itself in terms of capturing the curvature effects in the more complex compressor stage. A brief qualitative comparison of speedlines and efficiency lines was made based on the relative differences of the SST-CC and SST models, which showed consistent trends between the 307C and 1C performance lines. In both cases the SST-CC curve shows the effects of predicting a lower PR and lower mass flow at all points as compared to the SST curve. However, this is only a qualitative comparison and the evaluation of performance will be further enforced by experimental data in the near future. Contours of  $f_{r1}$  and eddy viscosity were compared between the 1C and simplified

geometry cases. The  $f_{r1}$  comparison of the SST-CC model showed that both the 1C geometry and showed the same effects of increased  $f_{r1}$  near the concave surface and decreased  $f_{r1}$  near the convex surface, however the simplified geometry seemed to accentuate these effects, showing an  $f_{r1}$  range of 0 to 1.25, where the 1C case showed a more reserved 0.375 – 1.25 range. A comparison of the eddy viscosity was also made, based on the work of Dufour et al. (2008), which revealed the correct increase and decrease of eddy viscosity near the concave and convex walls in the simplified case, but this difference was not apparent in the 1C case.

Finally, a further investigation into the mean and turbulent flow fields was conducted on the simplified geometry. The SST, SST-CC and RSM-SSG model were compared and an evaluation of the SST-CC model was made based on a comparison against the RSM-SSG model, which is naturally more sensitive to curvature effects. In a comparison of mean velocity, TKE, Reynolds normal stress and production of TKE profiles, the SST-CC model showed the correct sensitivity to curvature for most cases, and tended to trend towards the RSM-SSG results. For the Reynolds normal stress predictions, more obvious trends were found in the  $\overline{uu}$  stress than in the  $\overline{vv}$  and  $\overline{ww}$  stresses. A brief investigation of the terms in  $f_{r1}$  showed that an apparent sensitivity in the formulation of  $f_{r1}$  at the centerline could be causing a large  $f_{r1}$  gradient in this region.

Overall, this work investigated the SST-CC model in terms how it captures curvature effects and how it performs relative to the original SST model in a practical turbomachinery application. It successfully showed that the SST-CC model is reacting appropriately for each of the compressor cases, as well as in a simplified geometry based on a centrifugal impeller, by comparing different turbulence quantities and the production multiplier,  $f_{r1}$ . This work is useful for furthering the validation of the SST-CC model in turbomachinery applications, as well as aiding in the development of future turbomachinery components for both aerospace and other industrial applications.

## **10. RECOMMENDATIONS FOR FUTURE WORK**

---

Future research could be directed towards expanding on the results of the 1C compressor case by comparison with experimental data, completing a more in-depth comparison of the 1C compressor and simplified geometry and iterating with the design of the simplified geometry to improve the connection to the compressor flow.

At the time of submission of this thesis, a LDV measurement campaign is planned for the 1C centrifugal stage. These experiments will result in detailed velocity profiles at the compressor inlet, mixing plane and diffuser exit. Once completed, both global performance and flow field information will be available for the 1C compressor stage as was presented for the 307C compressor stage. With this information, a thorough comparison could be made between the SST-CC and SST speedlines, efficiency lines, flow fields and the available experimental data. The results could also be related back to the 307C results to evaluate the consistency of the predictions across two similar compressor applications.

In addition to comparing the 1C results to experimental data, additional research could be completed by further investigating the relationship between the 1C compressor and the simplified geometry. Quantities such as TKE, Reynolds normal stresses and the production of TKE could be compared between the simplified geometry and the equivalent locations in the 1C compressor. This would provide a further analysis of the representation of the 1C turbulence quantities by the simplified geometry.

Furthermore, the design of the simplified geometry could be altered to represent other flow characteristics of the 1C compressor case. This could be done by testing a converging cross section or a system rotation to isolate the effects of a pressure gradient or link the effects of rotation and curvature between the simplified geometry and 1C.

Finally, in terms of the curvature correction itself, the maximum value of the  $f_{r1}$  limiter could be adjusted to be larger than 1.25. It would be interesting to investigate the effects of changing the limiter, specifically in the concave region where the maximum value was prevalent in the simplified geometry.

## REFERENCES

---

- Ansys Inc. (2010). Ansys CFX-Solver Theory Guide, Version 13.0. USA: Ansys.
- Ansys Inc. (2010). Ansys ICEM CFD 13.0 User Guide. USA: Ansys.
- Baldwin, B. S., & Lomax, H. (1978). Thin layer approximation and algebraic model for separated turbulent flows. *Proceedings of the 16th Aerospace Sciences Meeting*. Huntsville: AIAA Paper No. 78-257.
- Barth, T. J., & Jespersen, D. C. (1989). The design and application of upwind schemes on unstructured meshes. *27th Aerospace Sciences Meeting*. 89-0366. AIAA.
- Bernard, P., & Wallace, J. (2002). *Turbulent flow: analysis, measurement and prediction*. Hoboken, NJ: John Wiley & Sons Inc.
- Bourgeois. (2008). Numerical mixing plane studies with validation for aero-engine centrifugal compressor design. Master's Thesis, The University of Western Ontario.
- Bourgeois, J. A., Martinuzzi, R. J., Savory, E., Zhang, C., & Roberts, D. A. (2011). Assessment of turbulence model predictions for an aero-engine centrifugal compressor. *ASME Journal of Turbomachinery*, 133, 011025-1.
- Boussinesq, J. (1877). Théorie de l'écoulement tourbillant. Mém. présentés par Divers Savants Acad. Sci. Inst. Fr. 23, 46-50.
- Boyce, M. P. (2003). *Centrifugal compressors: a basic guide*. Tulsa, Oklahoma: PennWell Corporation.
- Bradshaw, P. (1973). Effects of streamline curvature on turbulent flow. *AGARDograph*, AG-169.
- Brun, K., & Kurz, R. (2009). The compressor operating range: stall, surge and choke. *Mechanical Engineering*, 131(5), 52.
- Cengel, Y. A., & Boles, M. A. (2006). *Thermodynamics: An Engineering Approach*, 5th ed. New York, NY: McGraw-Hill Higher Education.
- Denton, J. D. (2010). Some limitations of turbomachinery CFD. *Proceedings of the ASME Turbo Expo 2010: Power for Land, Sea and Air*, (pp. GT2010-22540).

- Dhakal, T. P., & Walters, D. K. (2009). Curvature and rotation sensitive variants of the k-w SST turbulence model. *Proceedings of the ASME Fluids Engineering Division Summer Conference 2009, Part C*, pp. 2221-2229.
- Dixon, S. L., & Hall, C. A. (2010). *Fluid Mechanics and Thermodynamics of Turbomachinery, 6th ed.* Oxford: Elsevier Butterworth-Heinemann.
- Dufour, G., Cazalbou, J.-B., Carbonneau, X., & Chassaing, P. (2008). Assessing rotation/curvature corrections to eddy-viscosity models in the calculations of centrifugal-compressor flows. *ASME Journal of Fluids Engineering*, 130(9), 091401.
- Durbin, P. (2011). Review: Adapting scalar turbulence closure models for rotation and curvature. *Journal of Fluids Engineering*, 133(6), 061205.
- Etemad, S., & Sundén, B. (2006). Numerical investigation of turbulent heat transfer in a rectangular sectioned 90 degree bend. *Numerical Heat Transfer, Part A: Applications*, 49(4), 323-343.
- Girimaji, S. S. (1997). A Galilean invariant explicit algebraic Reynolds stress model for turbulent curved flows. *Physics of Fluids*, 9(4), 1067-1077.
- Holloway, A. G., Roach, D. C., & Akbary, H. (2005). Combined effects of favourable pressure gradient and streamline curvature on uniformly sheared turbulence. *Journal of Fluid Mechanics*, 526, 303-336.
- Kim, W. J., & Patel, V. C. (1994). Origin and decay of longitudinal vortices in developing flow in a curved rectangular duct (data bank contribution). *ASME Journal of Fluids Engineering*, 116(1), 45-52.
- Kozulovic, D., & Rober, T. (2006). Modelling the streamline curvature effects in turbomachinery flow. *Proceedings of the ASME Turbo Expo, Part B*, (pp. 1239-1248).
- Launder, B. E., & Spalding, D. B. (1974). The numerical computation of turbulent flows. *Computer Methods in Applied Mechanics and Engineering*, 3, 269-289.
- Marconcini, M., Rubecchini, F., Arnone, A., & Ibaraki, S. (2008). Numerical investigation of a transonic centrifugal compressor. *ASME Journal of Turbomachinery*, 130, 011010-1.
- Menter, F. R. (1994). Two-equation eddy-viscosity turbulence models for engineering applications. *AIAA Journal*, 32(8), 1598-1605.



- Mokhtarzadeh-Dehghan, M. R., & Yuan, Y. M. (2003). Measurements of turbulence quantities and bursting period in developing turbulent boundary layers on the concave and convex walls of a 90° square bend. *Experimental Thermal and Fluid Science*, 27(1), 59-75.
- Munch, C., & Métais, O. (2007). Large eddy simulations in curved square ducts: variation of the curvature radius. *Journal of Turbulence*, 8, 1-18.
- Patel, V. C., & Sotiropoulos, F. (1997). Longitudinal curvature effects in turbulent boundary layers. *Progress in Aerospace Sciences*, 33(1-2), 1-70.
- Piquet, J. (1999). *Turbulent flows: models and physics*. Germany: Springer-Verlag.
- Pope, S. B. (2000). *Turbulent Flows*. Cambridge, UK: Cambridge University Press.
- Raisee, M., Alemi, H., & Iacovides, H. (2006). Prediction of developing turbulent flow in 90° curved ducts using linear and non-linear low-Re k-epsilon models. *International Journal for Numerical Methods in Fluids*, 51(12), 1379-1405.
- Roberts, D. A., & Steed, R. (2004). A comparison of steady state centrifugal stage CFD analysis to experimental rig data. *ANSYS User's Conference*. Pittsburgh.
- Smirnov, P. E., & Menter, F. R. (2009). Sensitization of the SST turbulence model to rotation and curvature by applying the Spalart-Shur correction term. *ASME Journal of Turbomachinery*, 131(4), 041010-1.
- So, R. M., & Mellor, G. L. (1973). Experiment on convex curvature effects in turbulent layers. *Journal of Fluid Mechanics*, 60(1), 43-62.
- Sotiropoulos, F., & Ventikos, Y. (1998). Flow through a curved duct using nonlinear two-equation turbulence models. *AIAA Journal*, 36(7), 1256-1262.
- Spalart, P. R., & Allmaras, S. R. (1994). A one-equation turbulence model for aerodynamic flows. *Recherche Aerospaciale*, 1(1), 5-21.
- Spalart, P. R., & Shur, M. (1997). On the sensitization of turbulence models to rotation and curvature. *Aerospace Science and Technology*, 1(5), 297-302.
- Speziale, C., Sarkar, S., & Gatski, T. (1991). Modelling the pressure-strain correlation of turbulence: an invariant dynamical systems approach. *Journal of Fluid Mechanics*, 227, 245-272.
- Tsujita, H., Mizuki, S., Gaku, M., & Atsumasa, Y. (2003). Numerical investigation of loss generation mechanisms of flow in turbomachinery by using a curved square duct. *Journal of Thermal Science*, 12(3), 219-224.

- Turton, R. K. (1995). *Principles of Turbomachinery, 2nd ed.* London, United Kingdom: Chapman & Hall.
- Wallin, S., & Johansson, V. A. (2002). Modelling streamline curvature effects in explicit algebraic Reynolds stress turbulence models. *International Journal of Heat and Fluid Flow*, 23(5), 721-730.
- White, F. M. (2011). *Fluid Mechanics, 7th ed.* New York, NY: McGraw-Hill.
- Wilcox, D. C. (1988). Re-assessment of the scale-determining equation for advanced turbulence models. *AIAA Journal*, 26(11), 1299-1310.
- Wilcox, D. C. (2006). *Turbulence Modeling for CFD, 3rd ed.* California: DCW Industries, Inc.
- Xu, J., Ma, H., & Huang, Y. (2008). Nonlinear turbulence models for predicting strong curvature effects. *Applied Mathematics and Mechanics (English Edition)*, 29(1), 31-42.
- York, W. D., Walters, D. K., & Leylek, J. H. (2009). A simple and robust eddy-viscosity formulation for curved and rotating flows. *International Journal of Numerical Methods for Heat and Fluid Flow*, 19(6), 745-776.
- Ziegler, K. U., Gallus, H. E., & Niehuis, R. (2003). A study on impeller-diffuser interaction Part I: Influence on the performance. *ASME Journal of Turbomachinery*, 125, 173-182.

## APPENDIX I – SAMPLE CALCULATIONS

---

### A. Total-to-static efficiency

**Equation:**

$$\eta_{ts} = \frac{h_{4s} - h_{01}}{h_{04} - h_{01}} = \frac{c_{p,4}T_{4s} - c_{p,1}T_{01}}{c_{p,4}T_{04} - c_{p,1}T_{01}}$$

**Known:**

$T_1, T_4, T_{01}, T_{04}, c_{p,1}, c_{p,4}$  and  $p_4/p_1$

**Solution method:**

- First,  $P_{r1}$  is found by interpolating using  $T_1$  in Appendix 1, Table A-17 (Cengel & Boles, 2006, p. 936)
- Then  $P_{r4}$  is found using the relation (Cengel & Boles, 2006, p. 365):

$$\frac{p_4}{p_1} = \frac{P_{r4}}{P_{r1}} \text{ or } P_{r4} = P_{r1} \frac{p_4}{p_1}$$

- Using  $P_{r4}$ , the isotropic exit temperature,  $T_{4s}$  is found using interpolation in Appendix 1, Table A-17 (Cengel & Boles, 2006, p. 936)

**Notes:**

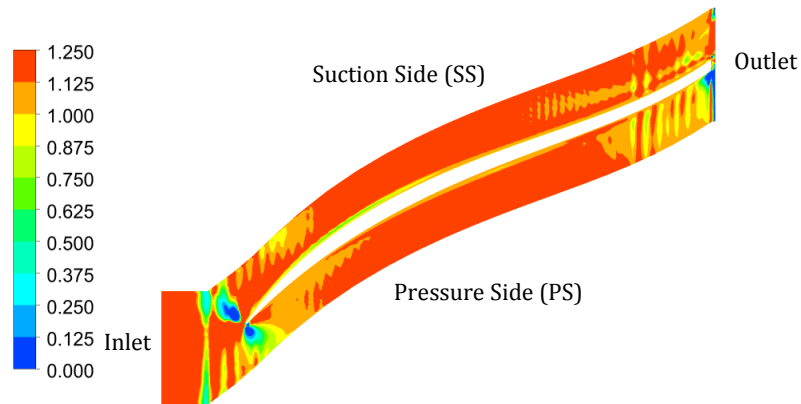
- The subscripts '1' and '4' represent the impeller inlet and diffuser exit, respectively
- All variable values are mass flow averaged quantities at the two different locations

## APPENDIX II – ADDITIONAL PLOTS

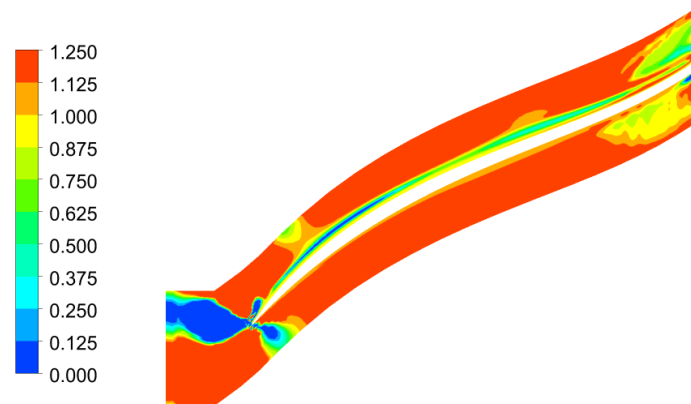
---

### A. 1C compressor results - $f_{r1}$ spanwise contours

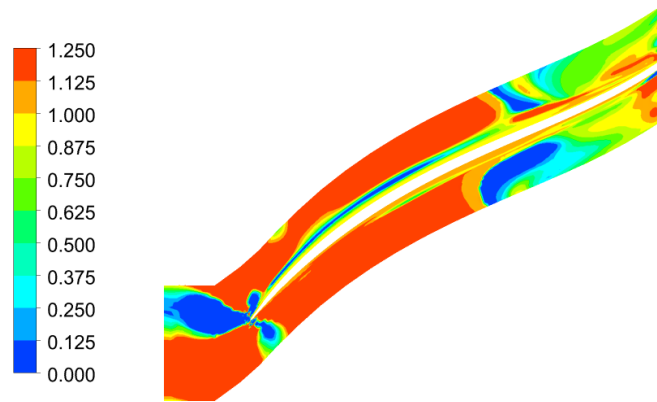
This appendix contains additional figures from 1C  $f_{r1}$  investigation in §7.3. The spanwise contours of  $f_{r1}$  for 5, 25, 50, 75 and 95% span are shown in Figure 48. For a brief discussion on these contours, refer to §7.3 ; or for a more detailed discussion of the same contours in the 307C case, refer to §6.3.



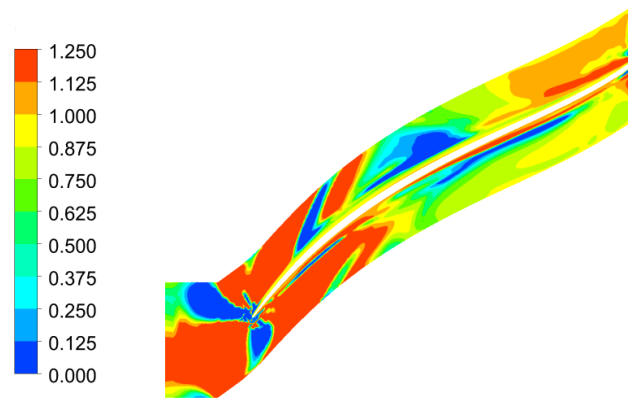
(a) 5% span



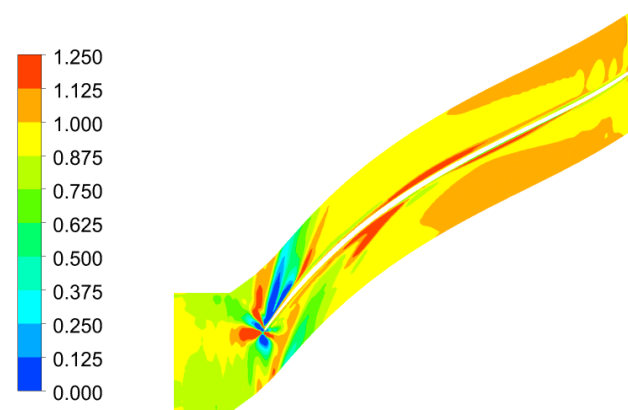
(b) 25% span



(c) 50% span



(d) 75% span



(e) 95% span

**Figure 48: Development of the  $f_{r1}$  parameter in the 1C, progressing spanwise in the impeller starting at the hub: (a) 5%, (b) 25%, (c) 50%, (d) 75% and (e) 95% span.**

## CURRICULUM VITAE

---

**Name:** Kevin James Elliott

**Post-secondary Education and Degrees:** The University of Western Ontario  
London, Ontario, Canada  
2006 – 2010  
*Bachelor of Engineering Science, Mechanical Engineering with Distinction*

**Honours and Awards:** MITACS Accelerate Intern  
2010 – 2011

Ontario Graduate Scholarship Recipient  
2011 – 2012

Western Graduate Research Scholarship  
2010 – 2012

John E. K. Foreman Gold Medal in  
Mechanical and Materials Engineering  
2010

Dean's Honour List  
2007 – 2010

**Related Work Experience:** Teaching Assistant  
*The University of Western Ontario*  
2010 – 2012

Project Manager  
*The Research Park*  
2008

**Publications:**

Elliott, K.J., Savory, E., Zhang, C., Martinuzzi, R. J. & Lin, W.E. (2012). Analysis of a curvature corrected turbulence model using a 90 degree curved geometry modelled after a centrifugal compressor impeller. *CFDSC 2012*. Canmore, Alberta.